National Library
of Canada

Acquisitions and
Bibliographic Services Branch

395 Wellington Street
Ottawa, Ontario
K1A 0N4

Bibliothèque nationale
du Canada

Direction des acquisitions et
des services bibliographiques

395, rue Wellington
Ottawa (Ontario)
K1A 0N4

Your file Votre référence

Our file Notre référence

NOTICE

The quality of this microform is heavily dependent upon the quality of the original thesis submitted for microfilming. Every effort has been made to ensure the highest quality of reproduction possible.

If pages are missing, contact the university which granted the degree.

Some pages may have indistinct print especially if the original pages were typed with a poor typewriter ribbon or if the university sent us an inferior photocopy.

Reproduction in full or in part of this microform is governed by the Canadian Copyright Act, R.S.C. 1970, c. C-30, and subsequent amendments.

AVIS

La qualité de cette microforme dépend grandement de la qualité de la thèse soumise au microfilmage. Nous avons tout fait pour assurer une qualité supérieure de reproduction.

S'il manque des pages, veuillez communiquer avec l'université qui a conféré le grade.

La qualité d'impression de certaines pages peut laisser à désirer, surtout si les pages originales ont été dactylographiées à l'aide d'un ruban usé ou si l'université nous a fait parvenir une photocopie de qualité inférieure.

La reproduction, même partielle, de cette microforme est soumise à la Loi canadienne sur le droit d'auteur, SRC 1970, c. C-30, et ses amendements subséquents.

Canada

UNIVERSITY OF ALBERTA

TURBULENT FLAME GROWTH IN A COMBUSTION CHAMBER WITH HOMOGENEOUS DECAYING TURBULENCE

BY

DAVID SING-KHING TING

A thesis submitted to the Faculty of Graduate Studies and Research in partial fulfilment of the requirements for the degree of Master of Science

DEPARTMENT OF MECHANICAL ENGINEERING

EDMONTON, ALBERTA

Fall, 1992

National Library of Canada
Bibliothèque nationale du Canada

Canadian Theses Service
Service des thèses canadiennes

Ottawa, Canada
K1A 0N4

The author has granted an irrevocable non-exclusive licence allowing the National Library of Canada to reproduce, loan, distribute or sell copies of his/her thesis by any means and in any form or format, making this thesis available to interested persons.

L'auteur a accordé une licence irrévocable et non exclusive permettant à la Bibliothèque nationale du Canada de reproduire, prêter, distribuer ou vendre des copies de sa thèse de quelque manière et sous quelque forme que ce soit pour mettre des exemplaires de cette thèse à la disposition des personnes intéressées.

The author retains ownership of the copyright in his/her thesis. Neither the thesis nor substantial extracts from it may be printed or otherwise reproduced without his/her permission.

L'auteur conserve la propriété du droit d'auteur qui protège sa thèse. Ni la thèse ni des extraits substantiels de celle-ci ne doivent être imprimés ou autrement reproduits sans son autorisation.

ISBN 0-315-77319-7

Canada

UNIVERSITY OF ALBERTA

RELEASE FORM

AUTHOR : David Sing-Khing Ting

TITLE : TURBULENT FLAME GROWTH IN A COMBUSTION CHAMBER WITH HOMOGENEOUS DECAYING TURBULENCE

DEGREE : Master of Science

GRANTED : Fall, 1992

Permission is hereby granted to the University of Alberta Library to reproduce single copies of this thesis and to lend or sell such copies for private, scholarly or scientific research purposes only.

The author reserves all other publication and other rights in association with the copyright in the thesis, and except as hereinbefore provided neither the thesis nor substantial portion thereof may be printed or otherwise reproduced in any material form whatever without the author's prior written permission.

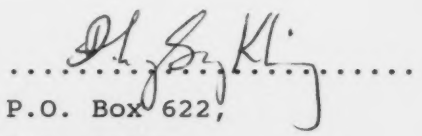

P.O. Box 622,
Sibu 96007,
Sarawak,
Malaysia.

July 27th 1992

UNIVERSITY OF ALBERTA

FACULTY OF GRADUATE STUDIES AND RESEARCH

The undersigned certify that they have read, and recommend to the Faculty of Graduate Studies and Research for acceptance, a thesis entitled TURBULENT FLAME GROWTH IN A COMBUSTION CHAMBER WITH HOMOGENEOUS DECAYING TURBULENCE submitted by David Sing-Khing Ting in partial fulfilment of the requirements for the degree of Master of Science.

.....

Dr. M.D. Checkel

(Supervisor)

.....

Dr. J.D. Dale

.....

Dr. J.T Ryan

July 27th 1992

To

The Dreamers

ABSTRACT

High speed Schlieren video and pressure trace analyses were used to study turbulence effects on burning velocity in a constant volume combustion chamber. Lean propane-air and lean methane-air mixtures of equivalence ratios between 0.75 and 0.96 were ignited at 101 kPa and 296 K. Schlieren images of flame growth were recorded at 2000 frames per second while combustion chamber pressure was simultaneously recorded. Turbulence was generated by pulling a 60% solid, perforated plate across the chamber prior to ignition. Turbulence intensity at ignition was up to 7 m/s with 2 mm integral scales for the propane-air tests and 8 mm integral scale for the methane-air tests. In the analysis, the turbulence parameters during combustion were adjusted for the effects of decay and rapid distortion in a closed chamber.

Results from both video and pressure trace analyses show the expected linear relationship between turbulent burning velocity and turbulence intensity. Moderate changes in equivalence ratio from 0.75 to 0.96 had negligible effects on this relationship when normalized by laminar burning velocity. The normalized relationship was not affected by small changes of integral scale of the order of 20%. In studying the flame growth from the ignition spark up to 55 mm flame radius, it was found that the effectiveness of turbulence increased dramatically as the flame grew. While the relationship of burning velocity to turbulence intensity remained linear, the linear coefficient increased with increasing flame size. It was also shown that this linear coefficient can be expressed as a function of the flame size normalized with the

integral scale.

The measured relationships were compared with values predicted by the model of Abdel-Gayed and Bradley. Their two-eddy theory over-predicted flame growth rate of these data. Alternatively, since the flame growth rate increased with flame size, it could be extrapolated that the two-eddy theory would be correct when the flame diameter is about 55 times larger than the integral scale.

ACKNOWLEDGEMENTS

The author would like take this opportunity to express special appreciation to the following individuals for contributing their expertise in making this thesis successful:

Mr. T. Nord, for his technical expertise in electronics in solving all the electronic problems.

Mr. A. Muir, for his prompt response in repairing and providing parts for the experimental apparatus.

Mr. I. Buttar, for his software expertise in solving the computer software problems encountered.

Mr. B. Cielin, Mr. B. Faulkner, Mr. W. Pittman and Mr. J. Foy for their prompt assistance in solving various problems.

Mr. R. Haley, for taking the high speed video.

Mr. K. Leung, for writing the image processing programs.

Mr. C. Johnston, for assisting in calibrating the area calculation program.

Prof. A. Hay, for providing the DAS8 data acquisition programs and subroutines.

Prof. J.T. Ryan, for his valuable feedback as an external examiner

Prof. J.D. Dale, for all the direct and indirect help as a committee member, graduate coordinator and chairman.

Prof. M.D. Checkel, for his diligent guidance in every aspect throughout the progress of this thesis, especially his patience in reading and correcting the drafts.

The author thanks his family and friends for their support.

The Department of Mechanical Engineering and NSERC are thanked for their financial support.

The author also thanks the Department of Electrical Engineering, especially Prof. Smy, for providing various equipment.

TABLE OF CONTENTS

CHAPTER	PAGE
1. INTRODUCTION	1
1.1 Objectives	1
1.2 Reasons For Study	1
1.3 Outline Of Study	2
2. THEORY AND BACKGROUND STUDIES	4
2.1 Perforated Plate Turbulence	4
2.2 Laminar Burning Velocity	7
2.3 Turbulent Burning Velocity	9
2.3.1 Effects Of Turbulence Intensity	12
2.3.2 Effects Of Eddy Scales	13
2.3.3 The Two-Eddy Theory	16
2.4 Spherical Flame In A Closed Combustion Chamber	17
2.4.1 Multi-zone Thermodynamic Equilibrium Model	20
2.4.2 Effects Of Rapid Distortion In A Closed Vessel	23
2.5 Spark Ignition	27
2.5.1 Energy Efficiency And Minimum Ignition Energy	27
3. EXPERIMENTAL APPARATUS AND PROCEDURE	32
3.1 Experimental Apparatus	32
3.1.1 Combustion Cell	32
3.1.2 Gas Mixer	35
3.1.3 Gas Chromatograph	38
3.1.4 High Speed Video Camera	40

TABLE OF CONTENTS (continued)

CHAPTER	PAGE
3.2 Procedure	41
3.2.1 Gas Mixer Calibration	41
3.2.2 Ignition System Tests	42
3.2.3 Supply Gas Analysis	44
3.2.4 Pressure Transducer Calibration	46
3.2.5 Quiescent Flame Tests	47
3.2.6 Turbulent Combustion Tests	47
3.3 Data Collecting And Analysis	48
3.3.1 Quiescent Runs	49
3.3.2 Turbulent Runs	51
4. QUIESCENT FLAME RESULTS AND ANALYSIS	53
4.1 Laminar Burning Velocities Of Lean Propane-Air Mixtures	54
4.2 Laminar Burning Velocities Of Lean Methane-Air Mixtures	68
4.3 Laminar Flame Growth From High Speed Video	79
4.4 Summary On Laminar Burning Velocity	84
5. TURBULENT FLAME RESULTS AND ANALYSIS	86
5.1 Turbulent Burning Velocity Of Lean Propane-Air	86
5.2 Turbulent Burning Velocity Of Lean Methane-Air	97
5.3 Methane-Air Turbulent Flame Growth From High Speed Video	112
5.4 The Effective Turbulence Intensity	121
5.4.1 Methane-Air Flames	121
5.4.2 Propane-Air Flames	122

TABLE OF CONTENTS (continued)

CHAPTER	PAGE
5.5 Comparison Of Turbulent Burning Velocity With Published Results	128
6. CONCLUSIONS AND RECOMMENDATIONS	132
6.1 Conclusions	132
6.1.1 Pressure Effects On Laminar Burning Velocities	132
6.1.2 Effects Of Eddy Scales On Burning Velocities	133
6.1.3 Effects Of Turbulence Intensity On Burning Velocities	133
6.1.4 Flame Growth From High Speed Video	135
6.1.5 Effect Of Rapid Distortion In A Closed Chamber Combustion	135
6.2 Recommendations	136
6.2.1 Pressure And Temperature Effects On Laminar Burning Velocities	136
6.2.2 Turbulence Measurements	136
6.2.3 Correlating Eddy Scales With Turbulent Burning Velocities	137
6.2.4 High Speed Video Images	138
REFERENCES	139
Appendix A : Burning Velocity Calculations	143
Appendix B : Air-Fuel Mixer Calibration	148
Appendix C : Flame Area Finding Algorithm	158
Appendix D : Spark Ignition Results	160
Appendix E : Gas Chromatograph	167
Appendix F : Pressure Transducer Calibration	182
Appendix G : Digitization And Analysis Programs	184

LIST OF TABLES

TABLE		PAGE
2.1	McDonell's Coefficients And Exponents (10 < X/D < 40)	6
2.2	Coefficients And Exponents For 5 < X/D < 40	7
2.3	Comparison Between The Equilibrium Model And STANJAN	22
3.1	Relative Response Factors From Dietz [Di67]	40
3.2	Supply Gas Analysis	46
3.3	Channel Inputs For Quiescent Runs	51
3.4	Channel Inputs For Turbulent Runs	52
4.1	Summary Results Of 75% Stoichiometric Propane-Air Quiescent Flames	55
4.2	Summary Results Of 90% Stoichiometric Propane-Air Quiescent Flames	56
4.3	Summary Results Of 95% Stoichiometric Propane-Air Quiescent Flames	57
4.4	Comparing Laminar Burning Velocities Of Propane-Air Flames	68
4.5	Summary Results Of 76% Stoichiometric Methane-Air Quiescent Flames	70
4.6	Summary Results Of 96% Stoichiometric Methane-Air Quiescent Flames	71
4.7	Comparing Pressure And Video Image Analyses	84
5.1	Summary Data From 75% Stoichiometric Propane-Air Turbulent Flames	87
5.2	Summary Data From 95% Stoichiometric Propane-Air Turbulent Flames	92
5.3	Summary Data From 76% Stoichiometric Methane-Air Turbulent Flames	99
5.4a	Summary Data From 96% Stoichiometric Methane-Air Turbulent Flames	105
5.4b	Summary Data From 96% Stoichiometric Methane-Air Turbulent Flames	106

LIST OF TABLES (continued)

TABLE		PAGE
5.5	Burning Velocity Of Lean Methane-Air Flame From Video Images at r = 23 mm (T_u = 298 K, P = 104 kPa)	117

LIST OF FIGURES

Figure		Page
2.1	Normal Decay Of Turbulence Intensity Behind 60% Solid, Perforated Plates.	8
2.2	Burning Velocity Of A Spherical Flame.	10
2.3	Influence Of Integral Scale On Turbulent Burning Velocity For Stoichiometric Propane-Air Mixtures [BL75].	14
2.4	Typical Temperature Profile Through A Flame Front.	19
2.5	Burning Of A Concentric Spherical Element In A Closed Vessel.	21
2.6	Losses Of A Spark Ignition System.	29
2.7	The Effect Of Spark Gap (Distance) On Minimum Ignition Energy.	30
3.1	A Schematic Of The Experimental Apparatus.	33
3.2	The Cubical Combustion Cell.	34
3.3	The 20 mm Diameter Perforated Plate.	36
3.4	The Critical Flow Orifice Gas Metering And Mixer System.	37
3.5	The High Energy Capacitance Discharge Ignition Circuit.	43
3.6	Signal Recording Summary For Quiescent Or Turbulent Runs.	50
4.1	Effects Of Initial Pressure On Maximum Pressure Rise And Time Of Peak Pressure For 75% Stoichiometric Propane-Air Flames.	58
4.2	Effects Of Initial Pressure On Maximum Pressure Rise And Time Of Peak Pressure For 90% Stoichiometric Propane-Air Flames.	59
4.3	Effects Of Initial Pressure On Maximum Pressure Rise And Time Of Peak Pressure For 95% Stoichiometric Propane-Air Flames.	60
4.4	Effect Of Pressure On Burning Velocity Of 75% Stoichiometric Propane-Air Flames.	62

LIST OF FIGURES (continued)

Figure		Page
4.5	Effect Of Pressure On Burning Velocity Of 90% Stoichiometric Propane-Air Flames.	63
4.6	Effect Of Pressure On Burning Velocity Of 95% Stoichiometric Propane-Air Flames.	64
4.7	Effect Of Equivalence Ratio On Pressure Exponent Of Lean Propane-Air Flames At r = 47 mm (T_u = 320 K).	65
4.8	Effect Of Equivalence Ratio On Pressure Exponent Of Lean Propane-Air Flames At r = 55 mm (T_u = 340 K).	66
4.9	Effects Of Initial Pressure On Maximum Pressure Rise And Time Of Peak Pressure For 76% Stoichiometric Methane-Air Flames.	72
4.10	Effects Of Initial Pressure On Maximum Pressure Rise And Time Of Peak Pressure For 96% Stoichiometric Methane-Air Flames.	73
4.11	Effect Of Pressure On Burning Velocities Of 76% And 96% Stoichiometric Methane-AIr Flames At r = 47 mm (T_u = 320 K).	74
4.12	Effect Of Pressure On Burning Velocities Of 76% And 96% Stoichiometric Methane-AIr Flames At r = 55 mm (T_u = 340 K).	75
4.13	Effects Of Equivalence Ratio And Temperature On Burning Velocities Of Methanne-Air Flames.	77
4.14	Laminar Lean Methane-Air Flame Growths From Schlieren Video Images And Pressure Trace Analyses.	80
4.15	Laminar Lean Methane-Air Burning Velocities From The Schlieren Video Images.	80
4.16	Comparing Laminar Velocity Of Lean Methane-Air Flames.	82
5.1	Effect Of Ignition-Time Turbulence Intensity On Burning Rate Of Lean Propane-Air Flames (Ø = 0.75).	89
5.2	Effect Of Turbulence Intensity On Burning Velocities Of Lean Propane-Air Flames (Ø = 0.75) At r = 55 mm.	90
5.3	Effect Of Ignition-Time Turbulence Intensity On Burning Rate Of Lean Propane-Air Flames (Ø = 0.95).	93

LIST OF FIGURES (continued)

Figure		Page
5.4	Effect Of Turbulence Intensity On Burning Velocities Of Lean Propane-Air Flames (Ø = 0.95) At r = 55 mm.	94
5.5	Effect Of Turbulence Intensity (Normal Direction) On Burning Velocities Of Lean Propane-Air Flames (Ø = 0.95) At r = 55 mm.	96
5.6	Effect Of Turbulence Intensity On Burning Velocities Of Lean Propane-Air Flames At r = 55 mm.	98
5.7	Effect Of Ignition-Time Turbulence Intensity On Burning Rate Of Lean Methane-Air Flames (Ø = 0.76).	101
5.8	Effect Of Turbulence Intensity On Burning Velocities Of Lean Methane-Air Flames (Ø = 0.76) At r = 55 mm.	102
5.9	Effect Of Turbulence Intensity (Normal Direction) On Burning Velocities Of Lean Methane-Air (Ø = 0.76) At r = 55 mm.	103
5.10	Effect Of Ignition-Time Turbulence Intensity On Burning Rate Of Lean Methane-Air Flames (Ø = 0.96).	107
5.11	Effect Of Turbulence Intensity On Burning Velocities Of Lean Methane-Air Flames (Ø = 0.96) At r = 55 mm.	108
5.12	Effect Of Turbulence Intensity (Normal Direction) On Burning Velocities Of Lean Methane-Air Flames (Ø = 0.96) At r = 55 mm.	109
5.13	Effect Of Turbulence Intensity On Burning Velocities Of Lean Methane-Air Flames At r = 55 mm.	111
5.14	Lean Methane-Air (Ø = 0.76) Turbulent Flames (compared with quiescent flame) From Video Images.	113
5.15	Turbulent Flame Growth Of Lean Methane-Air Flame (Ø = 0.76, u' = 0.4 m/s, Λ = 7.6 mm, X/D = 10 at ignition).	115
5.16	Turbulent Flame Growth Of Lean Methane-Air Flame (Ø = 0.76, u' = 2 m/s, Λ = 7.6 mm, X/D = 9 at ignition).	115
5.17	Effect Of Turbulence Intensity On Burning Velocities Of Lean Methane-Air Flames (Ø = 0.76) At r = 23 mm.	118

LIST OF FIGURES (continued)

Figure		Page
5.18	Effect Of Turbulence Intensity On Burning Velocities Of Lean Methane-Air Flames At r = 34 mm.	120
5.19	Dependence Of Linear Coefficient On Flame Size (Lean Methane-Air).	123
5.20	Effect Of Turbulence Intensity On Burning Velocities Of Lean Propane-Air Flames At r = 34 mm.	124
5.21	Effect Of Turbulence Intensity On Burning Velocities Of Lean Propane-Air Flames At r = 46 mm.	125
5.22	Dependence Of Linear Coefficient On Flame Size (Lean Propane-Air).	127
5.23	Comparing Turbulent Burning Velocities From This Study (points) With The Two-Eddy Theory Of Abdel-Gayed And Bradley [AB81].	129

NOMENCLATURE

atm	atmosphere
a	pressure exponent
A	ampere
b	temperature exponent
c	normal strain
c_d	dependence coefficient
C	capacitance
C_1, C_2,..	coefficients determined from experimental measurements
C_L	linear coefficient
°C	degree celsius
div	division
dr_i	change in pre-ignition radius of unburned gas
dt	time step
D	diameter
F	Faraday
GC	gas chromatograph
Hz	Hertz
ips	inch per second
I	current
kHz	10^3 Hertz
kPa	10^3 Pascal
K	degree Kelvin
l or L	litre
m	meter
min	minute

ml	10^{-3} litre
mm	10^{-3} meter
mJ	10^{-3} Joule
ms	10^{-3} second
P	pressure
P_c	pressure after combustion of the element
P_i	initial pressure (before ignition of the element)
P_{max}	maximum pressure rise
Q	heat loss
r	flame radius
r.m.s.	root mean square
r_b	radius of combustion wave
r_i	pre-ignition radius of unburned gas
r_{last}	previous flame radius
R	universal gas constant
R_{bomb}	hydraulic radius of vessel
R_Λ	turbulent Reynolds number $u'\Lambda/\nu$
s	second
S_t	turbulent burning velocity
S_u	laminar burning velocity
S_{u0}	reference laminar burning velocity (at T_i and P_i)
t	time
T	temperature
T_i	initial temperature
T_u	temperature of unburnt gas
$Time_{Pmax}$	time required to achieve maximum pressure
u	fluctuation component of velocity

u'	root mean square turbulent velocity or turbulence intensity
u'_{rd}	turbulence intensity including the effects due to rapid distortion
U	mean component of velocity
U_r	internal energy of reactant
U_p	internal energy of product
v	specific volume
V	volt
V1	voltage before ignition
V2	voltage after ignition
V_e	volume of element after combustion
V_i	volume of element before ignition
W	watt
W_{comp}	work of compression
X	distance downstream of the perforated plate
$\acute{o}$	laminar flame thickness
η	Kolmogorov scale
γ	specific heat ratio
γ_b	specific heat ratio of burnt gas
γ_u	specific heat ratio of unburnt gas
λ	Taylor microscale
Λ	integral scale
Λ_{actual}	integral scale after correcting for density change
μF	10^{-6} Faraday
μ_r	ratio of turbulent kinetic energy in the r direction
μ_θ	ratio of turbulent kinetic energy in the θ direction

μ_α	ratio of turbulent kinetic energy in the α direction
ν	kinetic viscosity
$\emptyset$	equivalence ratio
ρ	density
ρ_i	initial density
ζ	compression factor

CHAPTER 1: INTRODUCTION

1.1 Objectives

This thesis describes an experimental study of the effects of turbulence intensity and eddy scales on premixed, lean, propane-air and methane-air burning velocities in a closed combustion chamber with homogeneous decaying turbulence.

Lean propane-air and methane-air mixtures of equivalence ratios between 0.75 and 0.96 were ignited at 101.3 kPa and 296 K to investigate the effects of turbulence intensity on propagating premixed flames growing from spark kernels. The turbulence intensity at ignition was varied from 0 to 7 m/s. The integral scale was either 2 mm or 8 mm.

1.2 Reasons For Study

Cleaner and more efficient burning is vital for all internal combustion engines, especially as air pollution, the green house effect and rising fuel prices are become increasingly important issues. Leaner mixtures can ensure more complete burning, lower pollution and allow the use of higher compression ratios which can lead to higher thermal efficiencies [HS87, LA87, DO81, VS78][1]. Leaner mixtures also result in slower burning. As a consequence, increasing heat loss and poor combustion timing may lead to lower efficiency. In addition, slow burning may lead to knock, misfire

---

[1] Symbols in brackets, [], designate reference.

and increased cyclic variability in spark ignition engines.

Both methane and propane are common hydrocarbons. Methane is the major component in natural gas. With lower prices, abundant supply in Canada, and cleaner burning compared with gasoline, methane and propane are considered attractive alternative fuels [PC89]. As gases under room conditions, methane and propane are easy to use and analyze experimentally. Furthermore, there are published results for comparisons. These comparisons can lead to confirmation of some fundamental results. By the same token, the results obtained from this study can be useful to other researchers in this area and serve as guidelines for future work.

1.3 Outline Of Study

Turbulence is known to influence the burning characteristics of a combustible mixture [Mo90, Mc88, LK76, BL75, OH71, BT37]. However, there are still discrepancies from one study to another about the effects of turbulence on burning rates.

This research is an extension of previous studies by Modien [Mo90], McDonell [Mc88], and Checkel and Thomas [CT83, Ch81]. The experimental apparatus used is the same as that used by Modien [Mo90] and McDonell [Mc88] with the addition of a gas chromatograph and a high speed video camera. McDonell [Mc88] pointed out that the largest possible error in his experiments could be attributed to uncertainty in the gas mixtures composition. With the use of a highly accurate gas chromatograph in this study, the gas mixture composition discrepancy can be minimized. In addition, the actual

components of the fuel and dry air supply can be analyzed.

As compared with the study done by Modien [Mo90], this study covers a wider range of turbulence intensity with more experimental runs. Furthermore, both methane and propane are used as fuels in this study along with improvements in experimental apparatus and improved analysis.

The next chapter reviews the theory behind this experimental study and its analysis. Chapter 3 discusses the experimental apparatus with references to detailed design. It also details the actual experimental procedure. Chapter 4 reports and discusses laminar burning results. Chapter 5 presents and discusses turbulent combustion results. Conclusions are drawn in Chapter 6 which includes various recommendations.

CHAPTER 2: THEORY AND BACKGROUND STUDIES

This chapter covers the theory and analysis used in this experimental study. It also reviews previous studies, including the analyses used by other investigators.

2.1 Perforated Plate Turbulence

Turbulence intensity and integral scale are two major parameters involved in this study. The present turbulence generation system utilizes the same perforated plates used in Modien [Mo90] , McDonell [Mc88] and Checkel [Ch86]. Thus, the turbulence decay models from Checkel (unpublished work) and McDonell [Mc88] are adopted.

Conventional hot wire anemometry was used in earlier studies by McDonell and Checkel [Mc88, Ch86] to measure the decaying turbulence behind the perforated plates. The fluctuation velocities were measured directly in the wind tunnel, while integral scales were obtained as the auto-correlation of these velocities. Limited ensembles of turbulence decay cycles in the combustion chamber were compared with the detailed decay results in the wind tunnel. Both McDonell and Checkel demonstrated comparable results between turbulence in the combustion chamber and those in the wind tunnels. These measurements and comparisons are detailed in McDonell [Mc88] and Checkel [Ch86].

A simple turbulence decay model is expressed as:

$$\frac{\sqrt{\overline{u^2}}}{U} = c_1 \left(\frac{X}{D}\right)^{c_2} \qquad 2.1$$

where u = fluctuation component of velocity

U = mean component of velocity

X = distance downstream of the plate

D = hole diameter

Earlier studies such as [UW67, CC66, BP51, Fr48] of grid-generated turbulence used power law decay to describe the inertial subrange. By assuming isotropic turbulence, Frenkiel [Fr48] found that the decay exponent c_2 was -5/7. Baines and Peterson [BP51] obtained the same exponent over a limited range of turbulence behind a grid. The results from McDonell [Mc88] and Checkel (unpublished work) are tabulated in Tables 2.1 and 2.2 respectively. The values for the exponent, c_2, obtained by McDonell and Checkel are slightly higher but within reasonable agreement with earlier researchers.

Hinze [Hi75] explained the grid-generated turbulence in this way. As turbulence grows to its full development, larger eddies produce smaller eddies through inertial interaction, thereby transferring energy to the smaller eddies. At the same time, viscosity effects (dissipation) become more and more important for the smaller eddies. The relationships between the scales and the turbulence decay are expressed as Equations 2.2, 2.3 and 2.4.

$$\frac{\Lambda}{D} = C_3 \left(\frac{X}{D}\right)^{C_4} \qquad 2.2$$

where Λ = integral scale

$$\frac{\lambda}{D} = C_5 \left(\frac{X}{D}\right)^{C_6} \qquad 2.3$$

where λ = Taylor microscale

$$\frac{\eta}{D} = C_7 \left(\frac{X}{D}\right)^{C_8} \qquad 2.4$$

where η = Kolmogorov scale

The values for these coefficients and the exponents obtained by McDonell are tabulated in Table 2.1.

Table 2.1 : McDonell's Coefficients And Exponents (10 < X/D < 40).

D (mm)	C_1	C_2	C_3	C_4	C_5	C_6	C_7	C_8
20	1.286	-0.917	0.131	0.397	0.034	0.465	0.001	0.786
5	1.012	-0.875	0.216	0.286	0.059	0.616	0.002	0.825

Checkel (unpublished work) separated the decay of turbulence into three regions. This was done to better cover a wide range (including the inhomogeneous region) over which decay is not well represented by a single power law equation. The coefficients and exponents are tabulated in Table 2.2.

The new model tabulated in Table 2.2 is used throughout this study for calculating the turbulence intensity and integral scale.

The old model by McDonell, tabulated in Table 2.1, is used for estimating Taylor microscale and Kolmogorov scale for completeness. Figure 2.1 shows the comparisons between these two models in terms of turbulence decay. In general, the two models agreed reasonably well.

Table 2.2 : Coefficients And Exponents For 5 < X/D < 40.

Region	C_1	C_2	C_3	C_4
5<X/D<10	10.96	-1.812		
X/D<14.3			0.38	0
10<X/D<20	2.627	-1.191		
14.3<X/D			0.1	0.5
20<X/D<40	0.773	-0.783		

2.2 Laminar Burning Velocity

The burning velocity is defined as the velocity of the flame wave relative to the unburned gas ahead of the wave in the direction normal to the flame surface. This burning velocity is used in this study as a measure of the rate of burning.

From a pressure trace or a series of flame growth images, the burning velocity is calculated as the engulfment rate of the unburnt gas between measurement points. The volume of the unburnt gas which is engulfed during each time interval is considered as though it was a thin shell spread over a smooth sphere having the

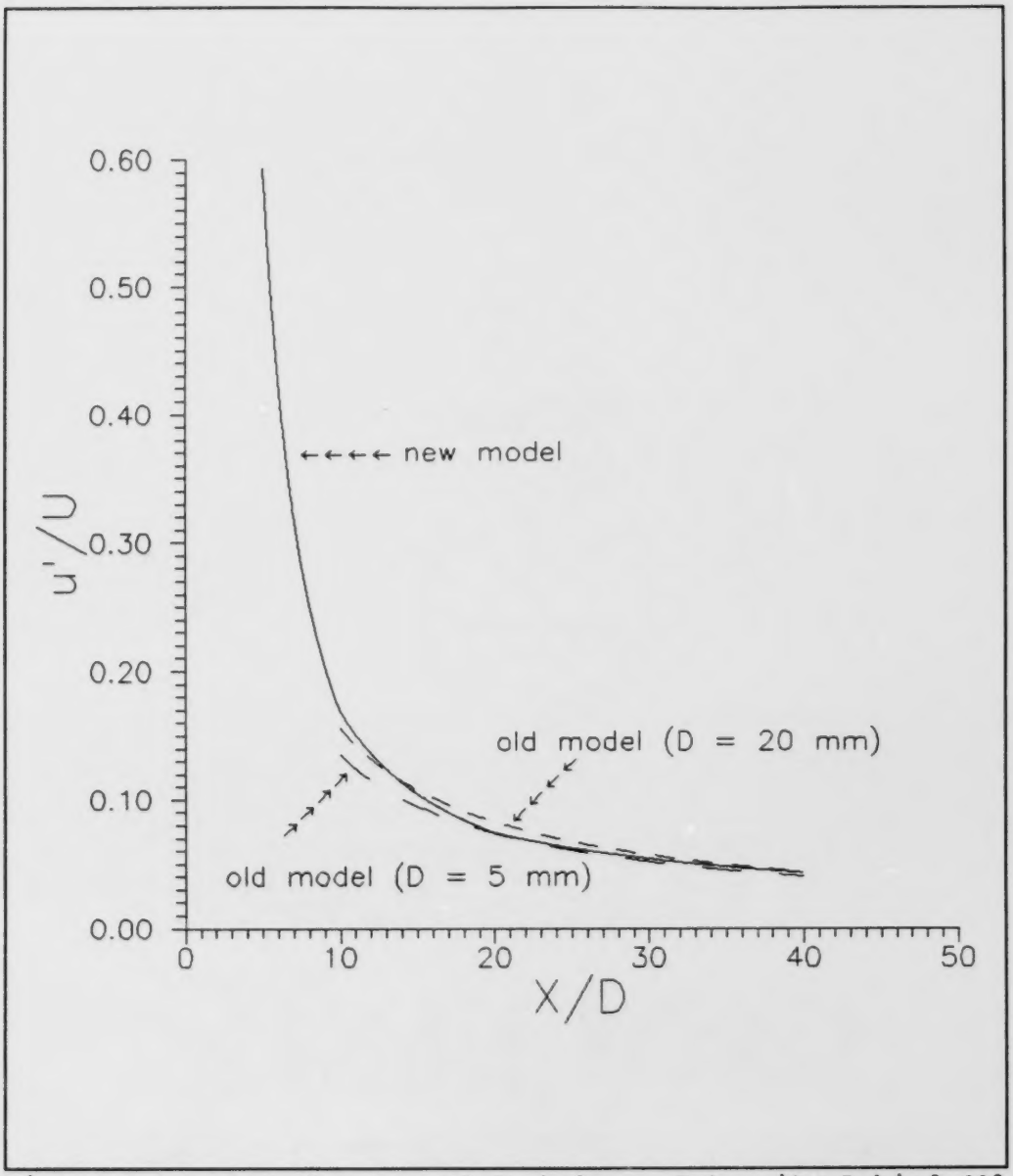

Figure 2.1 : Normal Decay Of Turbulence Intensity Behind 60% Solid, Perforated Plates.

same volume as the burnt gas. The thickness of the shell divided by the time interval gives the laminar burning velocity, S_u.

The geometric method used for calculating burning velocity can be described with the help of Figure 2.2. The flame radius, r, is calculated as the geometric mean radius of the previous flame radius, r_{last}, and the radius of the combustion wave, r_b, that is,

$$r = \sqrt{\frac{r_{last}^2 + r_b^2}{2}} \qquad 2.5$$

Before combustion, the burning element has the volume of the concentric spherical shell with thickness dr_i. The burning velocity is simply dr_i divided by the time interval, dt. A comparison of this geometric method with the Lewis and von Elbe [LV68] method is given in Appendix A.

There are several methods of studying burning velocity [Gl87, Ku86]. The more popular ones are the burner method, flat flame method, flame kernel method, soap bubble method and constant-volume vessel method. Rallis and Garforth [RG80] concluded that the spherical constant-volume vessel method is the most versatile and the most accurate method for analyzing laminar burning velocity. In this study, a cubical combustion chamber was used which is similar to the spherical combustion chamber and yet allows for turbulence generation using a perforated plate.

2.3 Turbulent Burning Velocity

Turbulence distorts the flame front and thus increases the

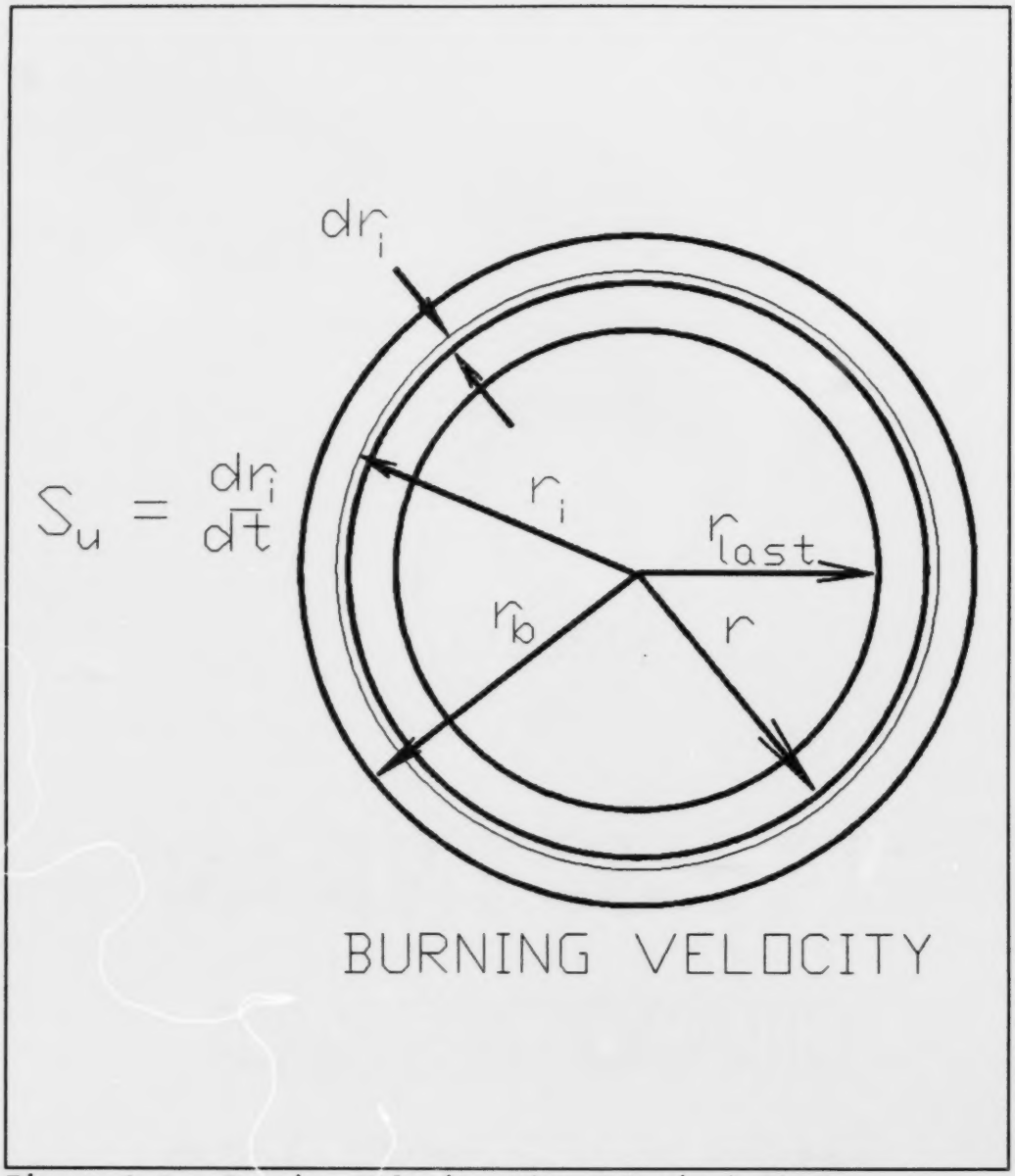

Figure 2.2 : Burning Velocity Of A Spherical Flame.

flame front area. It transports flaming material forward and unburned material into wrinkles in the flame front. Turbulence also increases transport properties at all scales. Hence, the mass transport or consumption rate of unburnt mixture increases. In general, this leads to an increase in burning velocity.

The distortion of the flame front by turbulence leads to an increase in the flame front thickness. Therefore, there is a larger volume of burning material compared with a laminar flame. The smaller eddies may carry pockets of unburned mixture into the burned gases. As a result, the thick flame front may consist of both burning and unburnt mixtures.

The thick turbulent flame front can create difficulty in determining the actual flame size from which the burning velocity is calculated. Both high speed Schlieren video and pressure trace analyses were used to calculate the burning velocities. For the pressure analysis used, the pressure rise corresponds to the amount of mixture burnt. Therefore, it is sensible to measure the turbulent burning velocity, S_t, based on the radius of the smooth sphere having volume equal to that of the gas already burnt.

By using the smoothed spherical flame in the pressure analysis, an average flame radius in the turbulent flame thickness is used as the flame front. For the image processing analysis, the outer Schlieren edge is used as the flame front. Both burned and burning mixtures are included as burned mixture and hence the flame size is exaggerated in calculating the turbulent burning velocity from Schlieren images.

2.3.1 Effects Of Turbulence Intensity

Most studies [LL88, Mc88, AB84] in combustion chambers, burners and engines agree that there is a very strong, roughly linear increase in the turbulent burning velocity with increasing turbulence intensity. However, the slope of the linear relationship varies from one study to another and the explanation about the combustion mechanisms also varied. Hence, a better understanding about the turbulence intensity effect on burning velocity is required.

Previous studies [AB87, Th86, AB86, AB84] found that the initial flame kernel is not exposed to the lower frequencies, larger eddies, in the turbulence. As the flame grows, progressively larger eddies become effective at shearing and distorting it. Through a history of interaction with the turbulence, the flame front becomes thicker and more complicated, thus, the flame area increases. In short, there is an increasing turbulence effect on a "developing turbulent flame".

In general, the turbulent burning velocity can be expressed as a function of turbulence intensity in the form

$$S_t = C_L\, u + S_u \qquad 2.6$$

where C_L = Linear Coefficient

It is a common practice to use this equation in the normalized form,

$$\frac{S_t}{S_u} = C_L\, \frac{u'}{S_u} + 1 \qquad 2.7$$

The advantage of using Equation 2.7 instead of Equation 2.6 is the unity constant. Using Equation 2.7, all results with the same linear coefficient fall into one single line despite different laminar burning velocities. The linear coefficient, C_L in Equations 2.6 and 2.7, is investigated for various flame sizes under different turbulence conditions in this study.

2.3.2 Effects Of Eddy Scales

The effects of eddy scales can be related to the occurrence of different regimes of turbulent flame propagation. Eddies responsible for wrinkling are large compared with the flame thickness [LV68]. Smaller eddies increase transfer rates of heat and mass within the flame. These smaller eddies have much lower energy and they decay quickly; therefore, their effects are negligible unless the turbulence intensity is very high [Wi85].

Ballal and Lefebvre [BL75] performed an experimental study using stoichiometric propane-air mixtures at 1 atm and room temperature. They concluded that there are three distinct regions of flame propagation as shown in Figure 2.3. The dashed lines fit the data points of the same normalized turbulence intensity, u'/S_u. The three regions described in [BL75] are as follows:

Region 1 : $u' < 2\ S_u$, $\eta > \delta$

where δ = laminar flame thickness

In this low turbulence and low velocity region, the burning velocity is increased due to wrinkling of the flame. Since all eddies are larger than the flame

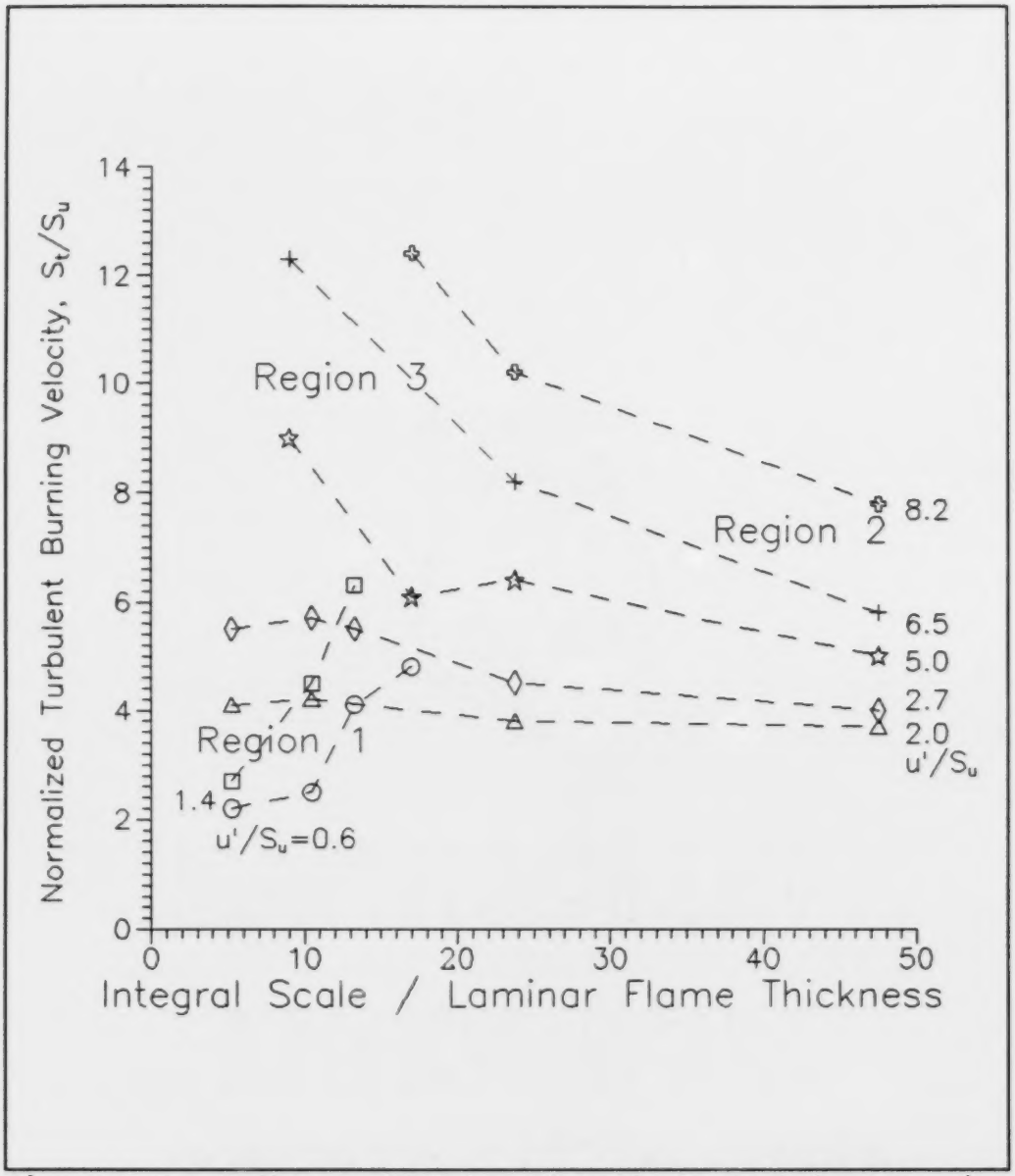

Figure 2.3 : Influence Of Integral Scale On Turbulent Burning Velocity For Stoichiometric Propane-Air Mixtures [BL75].

thickness, increasing these eddies increases the wrinkled area and hence the burning velocity.

Region 2 : $u' \approx 2\ S_u$, $\eta \approx \delta$

This is the region of moderate turbulence in which fresh mixture contains eddies which are both larger and smaller than the flame thickness. There are two different mechanisms involved in this region:

1) wrinkling of the flame front by eddies larger than flame thickness.

2) increasing the area of interface by eddies entrained in the burning zone.

The first mechanism increases the turbulent burning velocity as the scales increase. The second mechanism decreases the burning velocity as the scales are increased. Therefore, normally these two mechanisms cancel out the effect of changing scales.

Region 3 : $u' > 2\ S_u$, $\eta < \delta$

This is the region of high intensity and very small eddies. The combustion zone is regarded as a thick matrix of burned gases interspersed with eddies of unburned mixture. The total surface area of eddies is proportional to the inverse of the turbulence scale. Therefore, in this region the burning velocity increases with decreasing eddy scale.

Region 1 in Figure 2.3 illustrates some very peculiar trends

which are questionable. Under this low intensity, small scale turbulence conditions, turbulence decays very rapidly downstream of the grid. Therefore, small measurement uncertainties can result in large experimental errors.

Most practical cases fall into Region 2. This region is also called the reaction sheet regime [Wi85] or wrinkled flame regime. The present experimental study covers a wide range of integral scale (2 mm < Λ < 8 mm) in Region 2. Normalizing the integral scale with a laminar flame thickness of 0.1 mm, Λ/δ varied from 20 to 80 in this study. Therefore, according to Figure 2.3, for the range of integral scale used, there should be no effect of integral scale on the linear coefficient. In short, the normalized turbulent burning velocity and turbulence intensity relationship of this study would be expected to be independent of integral scale.

2.3.3 The Two-Eddy Theory

For uniform isotropic turbulence, the two-eddy theory of burning as postulated by Abdel-Gayed and Bradley [AB81], expresses burning rate in terms of both eddy decay and chemical reaction rates, for the large integral scale and dissipative Kolmogorov scale. According to the theory, burning in both types of eddies is essentially a molecular phenomenon. The rate of burning for each eddy size is expressed by the product of the rate of eddy dissipation and the amount of mixture chemically reacted during the eddy lifetime. Abdel-Gayed and Bradley found that at higher values of turbulent Reynolds number, R_Λ > 1500, the results computed from

the two eddy theory agreed well with the experimental results, provided the r.m.s turbulent velocity is greater than the laminar burning velocity. Uncertainties remain with regard to the small scale turbulent structure (chemical lifetime and fractional volume occupied) and the mode of combustion in these scales.

Present results are compared with those predicted by the two eddy theory in Chapter 5. Direct comparison in terms of the linear coefficient is not quite possible for one major reason. While the two eddy theory aimed at describing a "fully developed" turbulent burning velocity [Th86], the present and most engine turbulent burning velocities are measured in conditions where they are unlikely to be fully developed.

2.4 Spherical Flame In A Closed Combustion Chamber

Simple theory for analysis of quiescent combustion waves in a spherical chamber is well documented in Lewis and von Elbe [LV68]. They assume that the combustion wave propagates by both heat transfer and diffusion processes. This model derives burning velocity from a pressure trace and assumes:

a) combustion wave propagates isotropically forming two concentric spherical zones (burned and unburned mixtures) with an abrupt interface (no burning mass),

b) uniform properties in each zone,

c) adiabatic compression with abrupt temperature difference between the burned and unburned gases, and

d) uniform pressure throughout the chamber at any

instant.

The model used in this study is an improved model based on thermodynamic equilibrium conditions in many different zones.

The actual flame front of a combustion wave is shown in Figure 2.4. Though a laminar flame front is usually of the order of 0.1 mm [Wi85], it can be thick for a small spherical flame. The analysis used here assumes a thin flame front with no burning mass. Since there is always a burning volume, varying the location of the thin flame front can result in different burning velocities. According to Figure 2.4, a thin flame front at the position where the preheat and the reaction zones meet would best approximate the real combustion wave.

The pressure trace analysis is based on mass burnt which corresponds to thermal energy release. Using this pressure trace analysis, the thin flame front is located at the maximum temperature gradient point in Figure 2.4. Fristron [Fr65] has shown that the inner region of the luminous zone represents the best location for measuring gas velocities and areas for curved, thick flames. This is very close to the maximum temperature gradient point used in the pressure trace analysis.

The image processing analysis is based on Schlieren images which detect temperature gradient. The present image processing program detects the outer preheat zone as the thin flame front location where burning velocity is calculated. This outer preheat zone is in the unburnt gas mixture as shown in Figure 2.4. Therefore, the image processing analysis includes the burning

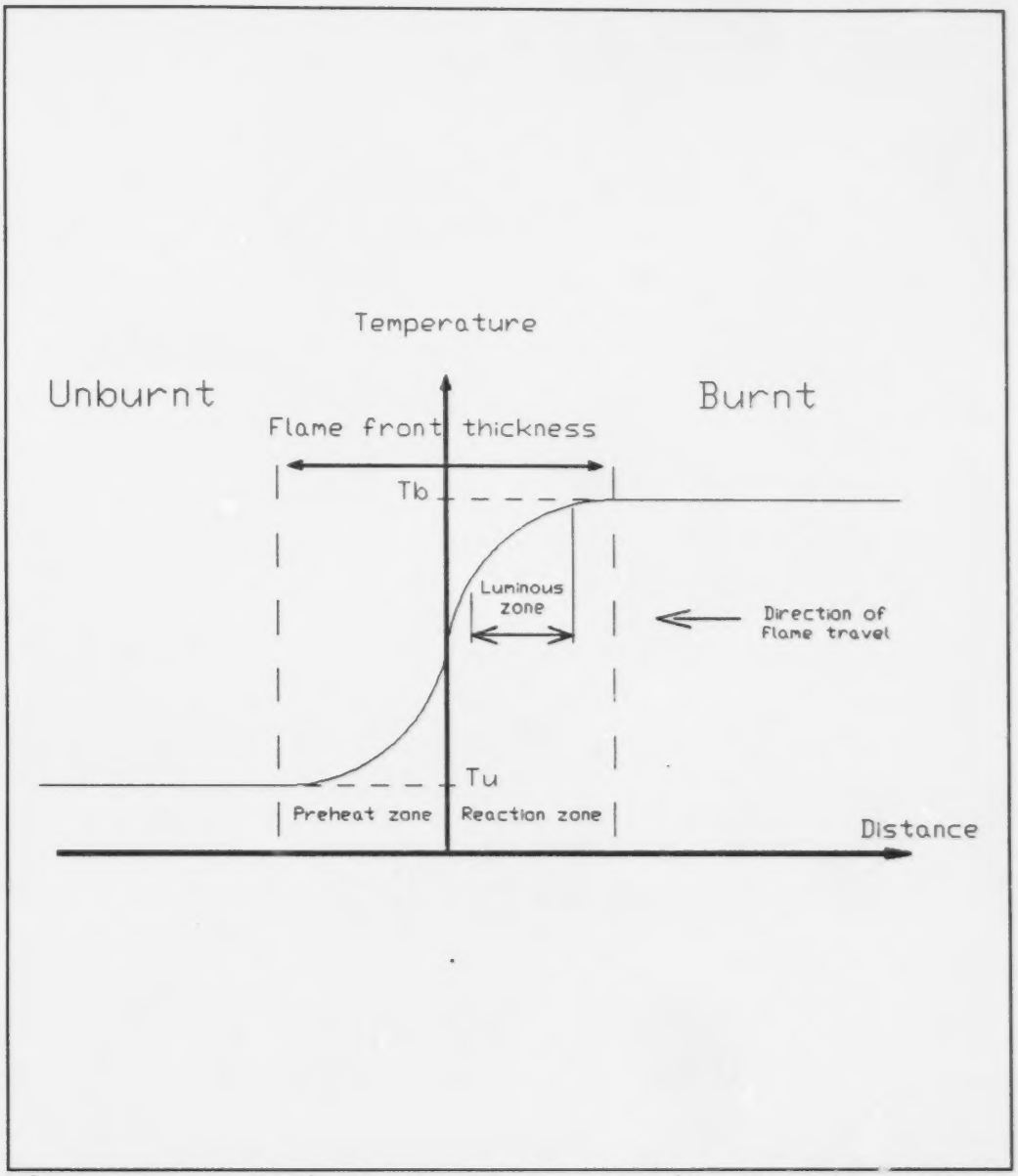

Figure 2.4 : Typical Temperature Profile Through A Flame Front.

volume as the burnt volume. For the turbulent case, some unburnt volume is carried into the thick flame front by eddies. The burning volume plus the unburnt volume could be significant especially in the high turbulence case.

2.4.1 Multi-zone Thermodynamic Equilibrium Model

This model assumes an adiabatic combustion wave which propagates isotropically in the radial direction from the point of ignition. Ellis and Wheeler [EW27, El28] found that the assumption of isotropic flame propagation is valid provided the spatial velocity is not too low.

In this multi-zone model, the mixture is divided into many (1200) elements consisting of equal mass fraction. Each element reacts sequentially, starting from the ignition point, so elements are treated as concentric spherical shells. During combustion of the n^{th} element as shown in Figure 2.5, its equilibrium composition of six species is calculated. The six species considered are CO, CO_2, O_2, N_2, H_2 and H_2O. In short, only the carbon dioxide and water-gas dissociations are considered.

$$CO_2 \rightleftarrows CO + \tfrac{1}{2} O_2$$

$$CO + H_2O \rightleftarrows CO_2 + H_2$$

It was found by Modien [Mo90] that for lean propane-air mixtures, these two dissociations could adequately represent the energy and species effects on combustion. This work reconfirmed the adequacy of the two dissociations in representing the species effects on combustion by comparing the theoretical results with that of

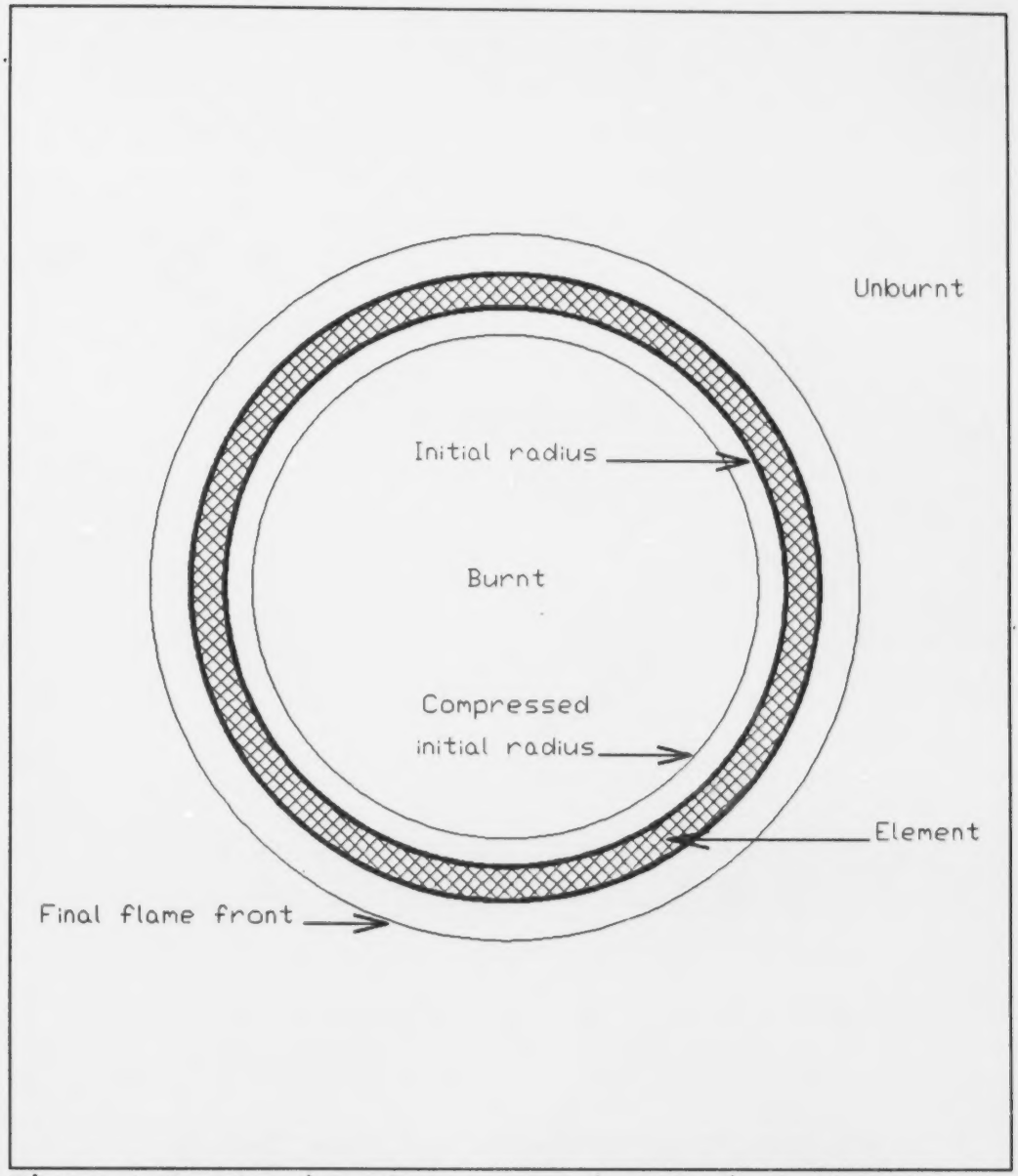

Figure 2.5 : Burning Of A Concentric Spherical Element In A Closed Vessel.

STANJAN computer model [Re87]. A typical comparison for propane-air combustion is shown in Table 2.3. This table shows that for 75% stoichiometric propane-air mixture ignited at 296 K, the maximum error is less than 0.5%.

Table 2.3 : Comparison Between The Equilibrium Model And STANJAN.

P (atm)	0.5	1	2
T (K) STANJAN	1959	1961	1963
T (K) model	1966	1967	1968
% error	0.36	0.31	0.25

All mixture elements are treated as ideal gases,

$$P\,v = R\,T \qquad \textbf{2.8}$$

where v = specific volume

R = universal gas constant

The code for the multi-zone thermodynamic equilibrium model is an energy balance and equilibrium solver based on property relationships as in Benson [Be77]. It starts by guessing the pressure after the n^{th} element burns. The program then calculates the temperature and the specific heat ratio of the reactants assuming isentropic compression to this pressure. From these values the total unburnt volume before and after combustion of the n^{th} element is calculated. The same calculation is done on all burnt elements to find their current temperature and volume at this

pressure. Then, an equilibrium calculation and energy balance is performed on the burning element. The energy balance assumes adiabatic combustion and includes the energy used by the burning element to compress all unburnt and previously burnt elements. Figure 2.5 shows that the burning element compresses both the burnt gas and the unburnt gas as it burns. The energy balance is :

$$Q + U_r = U_p + W_{comp} \qquad 2.9$$

where element heat transfer, Q, is assumed negligible, U_r and U_p are the internal energy of element reactants and products, and W_{comp} is the work done by the element on other elements. This work is the sum of the work done in compressing all other elements,

$$W_{comp} = \sum \frac{(P_e V_e - P_i V_i)}{(1 - \gamma)} \qquad 2.10$$

Using the calculated temperature and composition, the volume of the burning element is calculated after combustion. If the original pressure guess was right, the total volume of all elements is equal to the volume of the combustion chamber. If not, the pressure guess is refined and the calculation repeated until the correct pressure for each mass burnt increment is obtained. Concurrently, the flame radius at each mass burnt increment is also obtained by assuming the total burnt volume occupies a sphere of that radius.

2.4.2 Effects Of Rapid Distortion In A Closed Vessel

There are various flame-turbulence interactions including

1) amplification or generation of turbulence in flame

front,

2) distortion or amplification due to stretching around expanding flame, and

3) amplification due to compression or density increase.

These interactions compete with the normal turbulence decay. Many studies such as [VS90, Wi85] found that there is an overall increase in absolute turbulence intensity in turbulent flames which is known as flame-generated turbulence [Wi85]. Videto and Santavicca [VS90] used stoichiometric propane-air mixture to study flame-turbulence interaction in a freely-propagating premixed flame. They found that turbulence production in the flame is significant, and is an-isotropic in nature.

For the present study using a closed combustion chamber, the change in turbulence in front of the flame front is different from that of the unconfined explosion. In the present combustion chamber, the pre-ignition turbulence generated by the perforated plate decays quickly as discussed in Section 2.1. McDonell [Mc88] had shown that the normal turbulence decay in the combustion chamber (no explosion) corresponded well with that in the wind tunnel. During the actual flame growth, expansion of the flame compresses the unburnt mixture ahead. This leads to stretching of the vortices just in front of the flame front. As a result, there is an increase in turbulence intensity ahead of the flame front. Chew and Britter [CB88a] derived the equations of this rapid distortion for a growing spherical flame in a closed chamber. When accounting for the contributions due to rapid distortion, there

could be a few times amplification of turbulence intensity at the last stages of combustion [CB88a].

The rapid distortion model presented in Chew and Britter [CB88a] assumes adiabatic flame propagation with no heat loss to the walls of combustion chamber. Assuming isotropic turbulence initially, the enhancement of rapid distortion on the radial and transverse components of a spherical flame is as Equations 2.11 and 2.12 respectively. However, the contribution of the effect of rapid distortion on the transverse directions of the vortices may not play an important role in enhancing the burning rate. This is because the flame is propagating in the normal (radial) direction. This point is discussed further in Chapter 5. Equations 2.11 and 2.12 show the ratio of turbulent kinetic energy after distortion to that before in the radial and transverse directions respectively.

$$\mu_r = \zeta^{-3}\, c^{-2}\, \frac{3}{4}\, \left(\frac{\beta^2 - 1}{\beta^3} \tan^{-1}\beta + \beta^{-2}\right) \qquad 2.11$$

$$\mu_\theta = \mu_\alpha = \frac{3}{4}\, \frac{c}{\zeta} + \frac{3}{8}\, \frac{1}{\zeta^5\, c^5}\, \left(\frac{1}{\beta^3} \tan^{-1}\beta - \frac{1}{\beta^2(\beta^2 - 1)}\right) \qquad 2.12$$

where

$$\beta = \sqrt{\frac{1}{\zeta^2\, c^3} - 1} \qquad 2.13$$

compression factor,

$$\zeta = \left(\frac{\rho}{\rho_i}\right)^{-1} \qquad 2.14$$

normal strain,

$$C = \left(\frac{r_i}{r_b}\right)^2 \qquad 2.15$$

Therefore, the rapid distortion enhancement is

$$\frac{u'_{rd}}{u'} = \sqrt{\frac{\mu_r + \mu_\theta + \mu_\alpha}{3}} \qquad 2.16$$

where u'_{rd} is the turbulence intensity including the effects due to rapid distortion.

Chew and Britter [CB88a] mentioned that a further improvement in their rapid distortion model would be to include only those length scales which are affected by the distortion. This means that for the small initial flame kernel, only proportionally small scales are affected by the distortion. This improvement is expected to be small for the present study because the flames are large compared with the length scales.

As the rapid distortion affects the eddy vorticity, the eddy scales (volumes) are relatively unaffected. Therefore, it can be assumed that these eddy scales are only functions of unburnt mixture density; that is,

$$\Lambda_{actual} = \frac{P_i\, T_u}{P\, T_i}\, \Lambda \qquad 2.17$$

Due to a larger increase in pressure compared with temperature in the present closed vessel combustion, the actual scales during combustion are smaller than would result from normal decay only.

2.5 Spark Ignition

Kuo [Ku86] treated ignition with a 3 T (temperature, time and turbulence) rule of thumb. The temperature must be high enough to cause significant chemical reactions and/or pyrolysis. The time must be long enough to allow heat input to be absorbed by the reactants so that a runaway thermochemical process can occur. Turbulence must be high enough so that heat can be transferred from the reacted media to the unreacted media.

As the spark duration (order of 100 μs) is increased, there is a decrease in energy required for ignition followed by an increase. This is because as the spark duration is increased, the heating time increases, therefore, more energy is lost by conduction and radiation prior to ignition. On the other hand, for low power sparks, the shock strength decreases which results in less energy lost in shock waves generated by the spark. This shock wave propagates away quickly without any contribution to ignition.

2.5.1 Energy Efficiency And Minimum Ignition Energy

Spark energy efficiency is generally defined as the useful energy in forming a spark kernel divided by the stored energy. Zeldovich [Ze41] reported energy efficiency of 2 to 16% for a conventional spark. More recent study by Teets and Sell [TS88] found higher energy efficiency of about 20% for pointed electrodes.

For the current capacitance spark ignition system used, the energy from the capacitor is,

$$\text{Energy} = \tfrac{1}{2}\, C\, (V2^2 - V1^2)$$

where C = capacitance of the capacitor

V1 = voltage before ignition

V2 = voltage after ignition

In actual systems, there are losses due to radiation, shock wave formation, heat convection and conduction through the electrodes. Figure 2.6 shows the various losses which are present in a spark ignition system.

The energy efficiency used in this study is defined as the energy across the spark gap divided by the stored energy. This energy efficiency does not take the radiation, convection, conduction and shock wave formation losses into account.

The minimum ignition energy is the minimum amount of energy required to ignite a combustible mixture at a given condition. At small electrode spacings, electrodes remove large amount of heat from the incipient flame, as a result, a large minimum ignition energy is required. As the spacing is increased, the surface area to spark volume ratio decreases and heat loss is less. Hence, the ignition energy required decreases. In short, minimum ignition energy decreases as the electrode spacing is increased; it then reaches its lowest point at some spacing before it increases again. The final increase is believed to be due to the increase in circuit and other losses due to the high resistance of the gap. Paschen's law states that the sparking potential is a function of the product of pressure and gap length only [Pa89]. The sparking potential rises as the gap length is increased.

Figure 2.7 shows a typical shape of the effect of gap distance

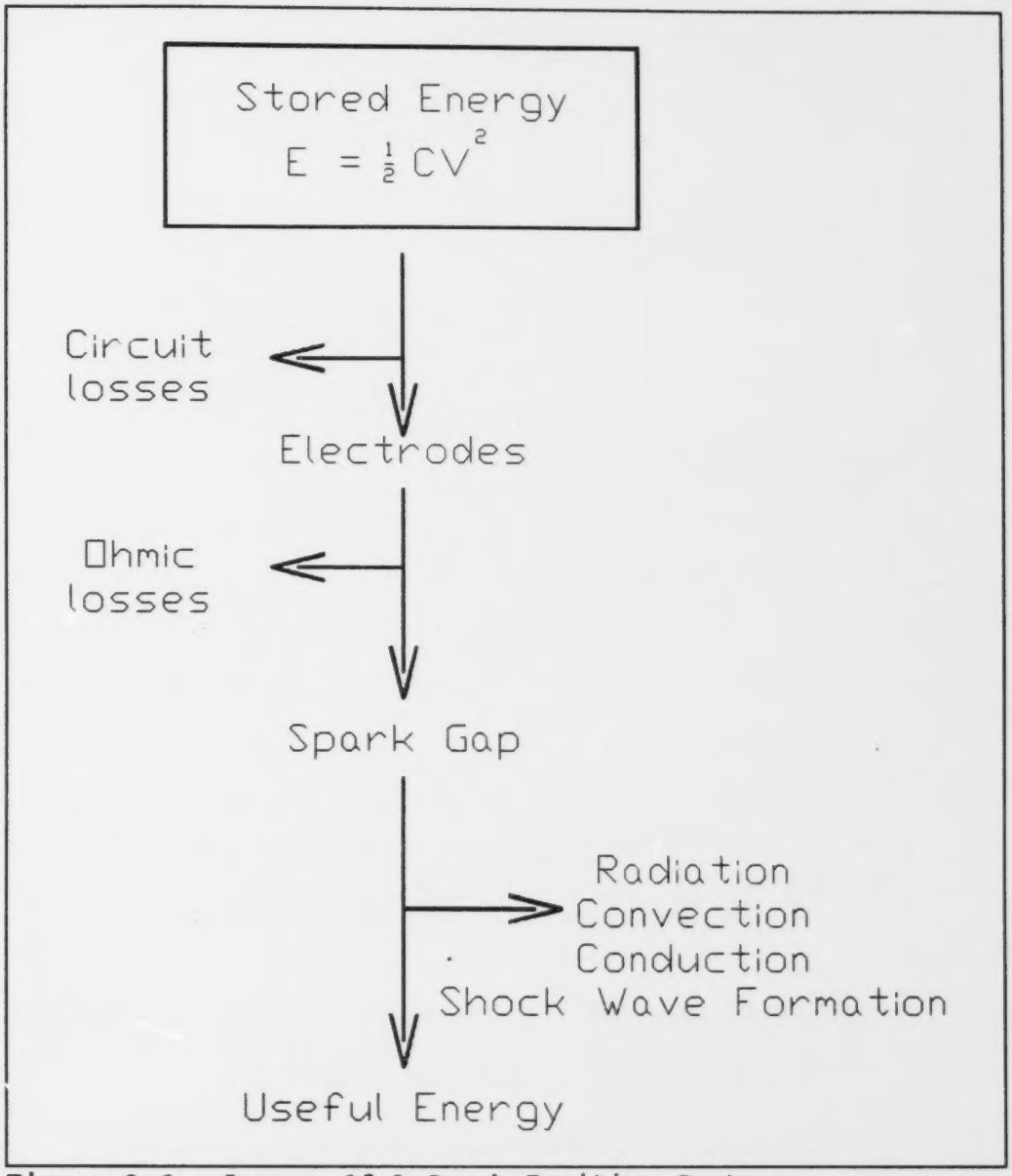

Figure 2.6 : Losses Of A Spark Ignition System.

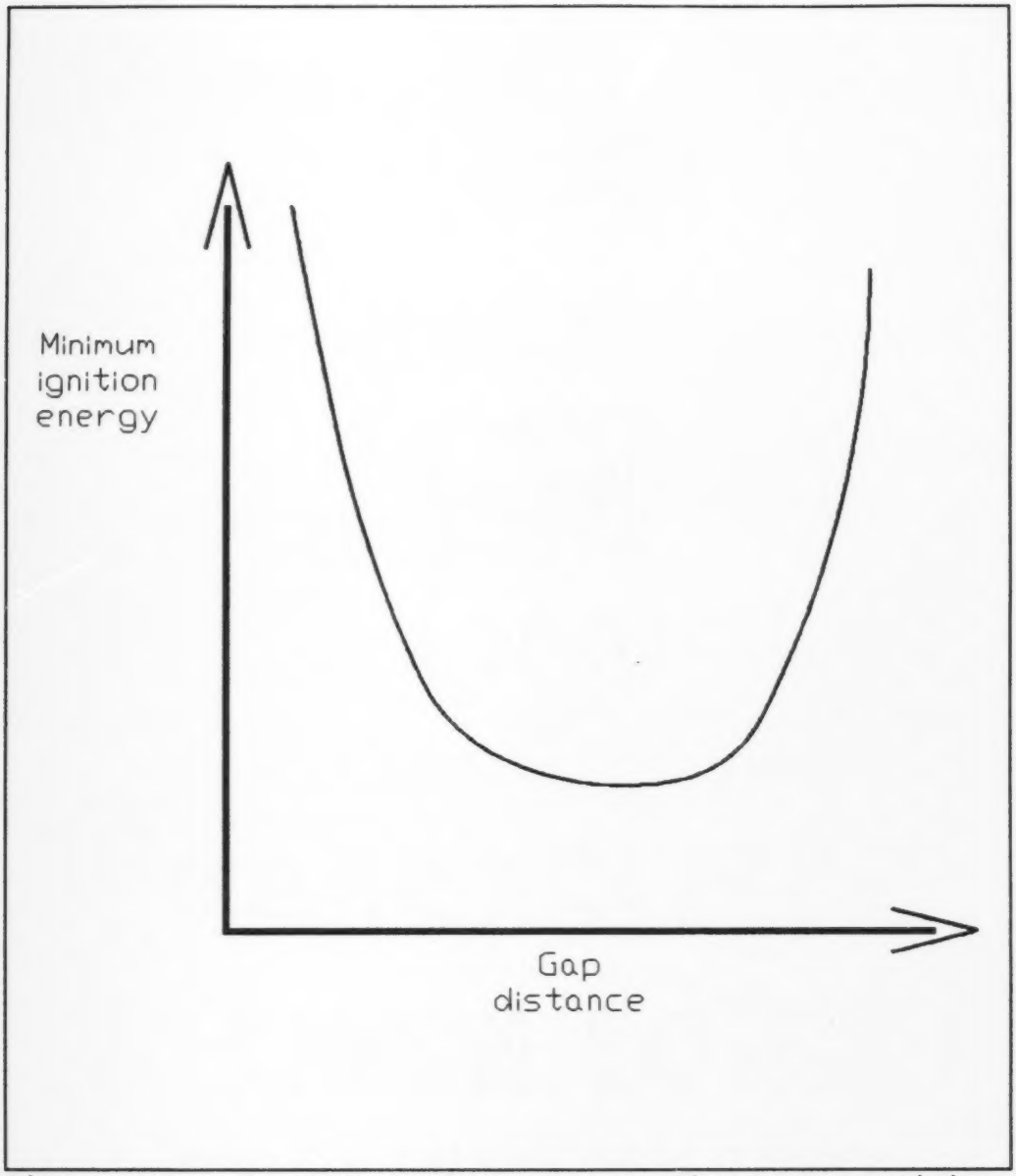

Figure 2.7 : The Effect Of Spark Gap (Distance) On Minimum Ignition Energy.

on minimum ignition energy for free or pointed electrode tips (from Lewis and von Elbe [LV68]). This figure illustrates the trend of a decrease followed by an increase in minimum ignition energy with increasing spark gap as discussed above.

The spark energy efficiency has the opposite trend with increasing spark gap compared with the minimum ignition energy. The spark gap for the highest spark energy efficiency is expected to be the spark gap with the lowest minimum ignition energy.

CHAPTER 3: EXPERIMENTAL APPARATUS AND PROCEDURE

This chapter describes the experimental apparatus used in this study. It also covers and explains the experimental procedures.

3.1 Experimental Apparatus

The experimental set-up shown in Figure 3.1 is similar to that used in Modien [Mo90] and McDonell [Mc88]. This set-up consists of four main elements. These main elements are :

1) Combustion Cell
2) Gas Mixer
3) Gas Chromatograph
4) High Speed Video Camera

There are two major modifications compared with the old set-up used in [Mo90] and [Mc88]. The gas chromatograph was installed for the purpose of reducing the largest uncertainty proclaimed by McDonell [Mc88]; mixture composition. Another modification of the set-up was the use of a Kodak Spin Physics high speed video camera with a capability of taking 2000 full frames per second instead of the Hycam camera used in [Mo90].

3.1.1 Combustion Cell

The combustion cell used was based on the original design by Checkel and Thomas [CT83, Ch81]. This apparatus was described in detail by Modien [Mo90] and McDonell [Mc88]. The 125 mm cube chamber, shown in Figure 3.2, is made of 6066-T6 aluminium alloy. All walls are 25 mm thick.

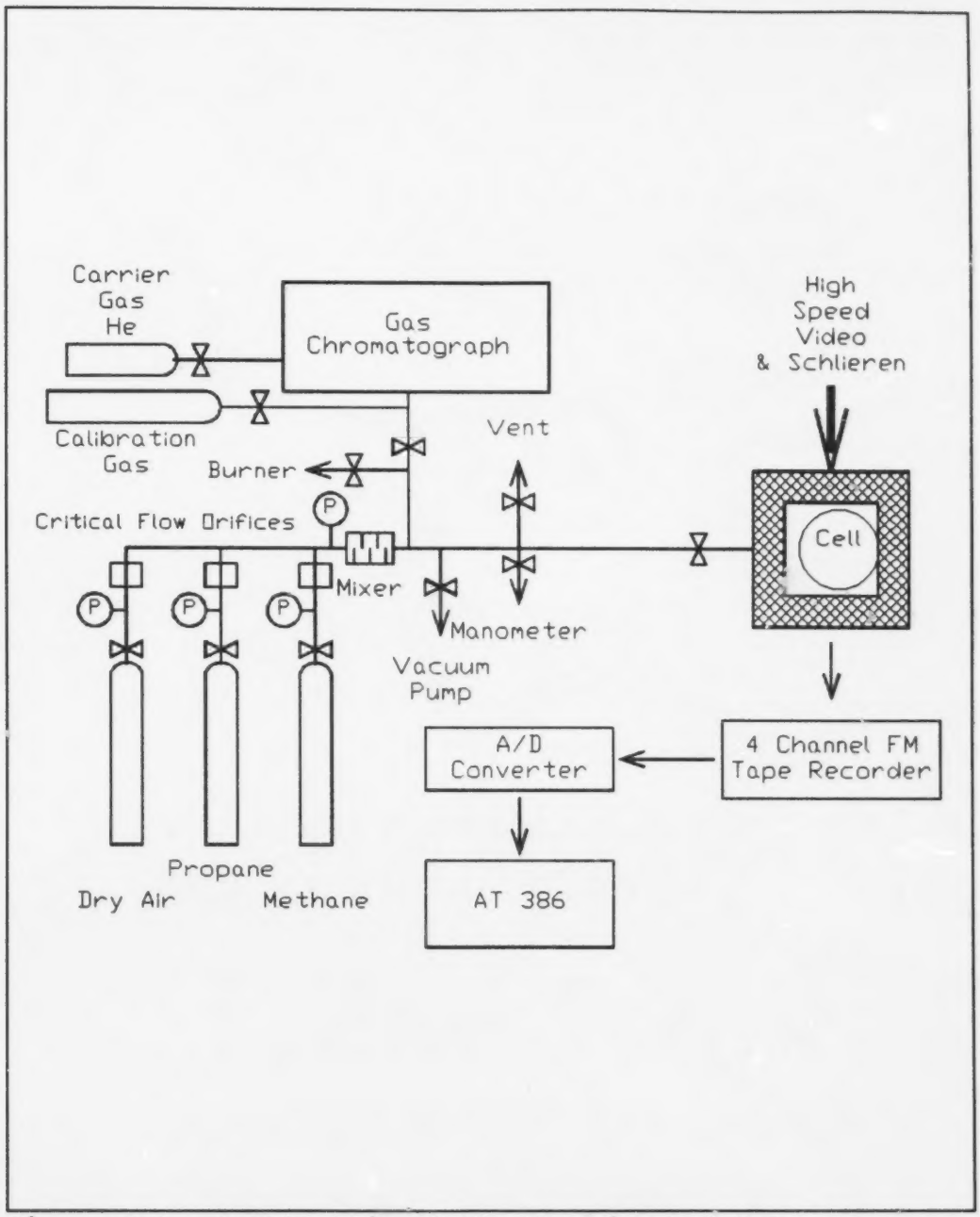

Figure 3.1 : A Schematic Of The Experimental Apparatus.

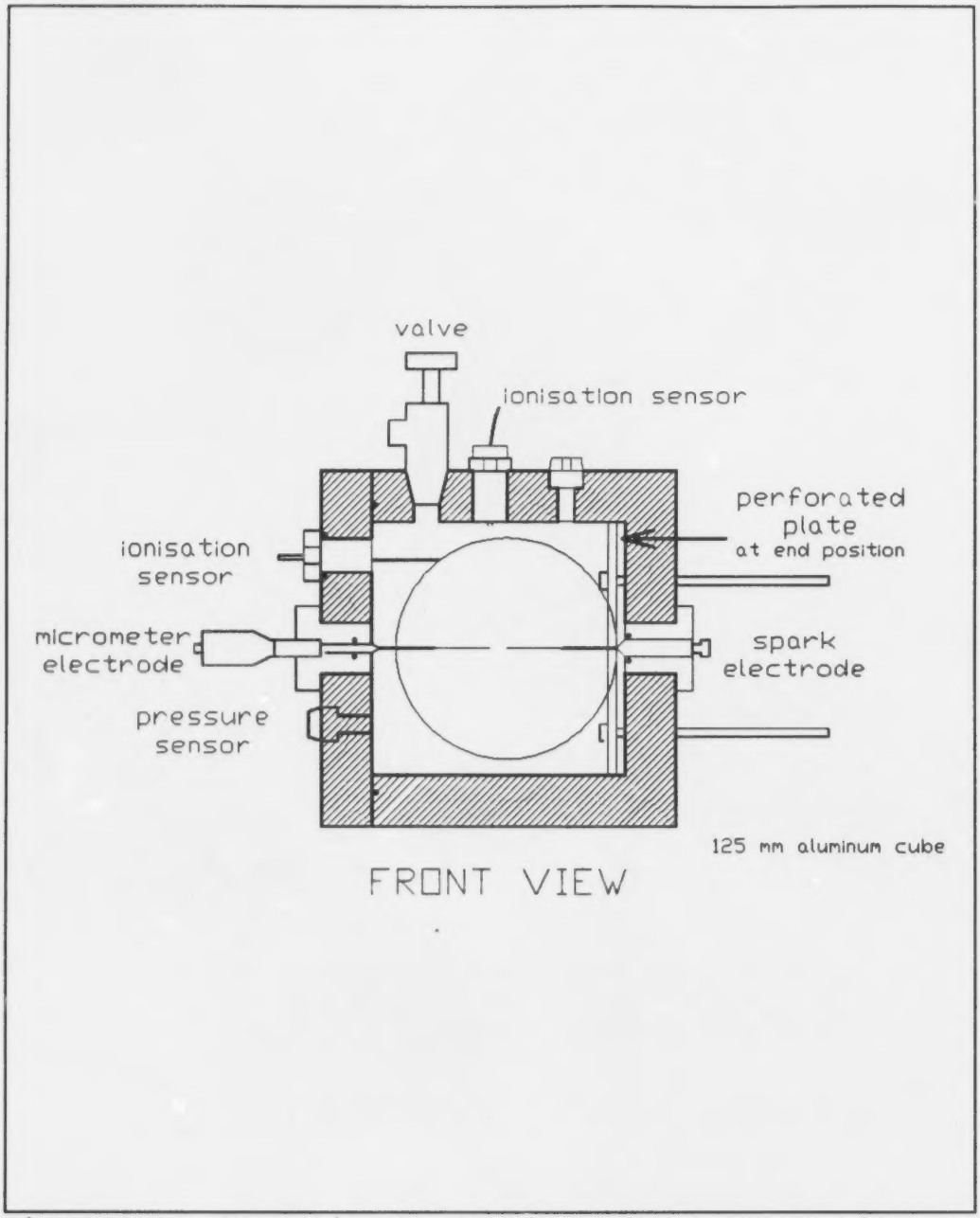

Figure 3.2 : The Cubical Combustion Cell.
(The Perforated Plate Is Shown At Its End-Of-Travel Position.)

Two circular PK-7 optical glass windows are mounted on the opposing sides (front and back) of the chamber to allow Schlieren visualization of the growing flame. These windows are 30 mm thick with diameters of 110 mm.

Two ionization probes are located at 40 mm and 60 mm (2 mm from the wall) from the spark gap. A Norwood model 111 four-active-arm strain gauge pressure transducer was used to trace the pressure. This pressure transducer is located on the wall of the combustion cell as shown in Figure 3.2. The two spark electrodes pass through the centre of the chamber. The micrometer electrode is adjustable for variable spark gap. A spark gap of 4.50 mm and a spark energy supply of 312.5 mJ (500 V and 2.5 μF) were used throughout this study.

A typical perforated plate used for generating the pre-ignition turbulence is shown in Figure 3.3. The plates have holes of diameter D placed on alternate intersections of a grid with spacing D to give a 60% solid ratio. The two plates used in this study are the 5 mm diameter and the 20 mm diameter plates described by McDonell [Mc88]. Both perforated plates are 5 mm thick. Whenever possible a single plate was used for the range(s) of turbulence intensity and/or turbulent eddy scales required. This procedure eliminates possible error due to plate change.

3.1.2 Gas Mixer

Air/Fuel ratio is controlled by the critical flow orifice gas metering and mixer system as shown in Figure 3.4. With known flow

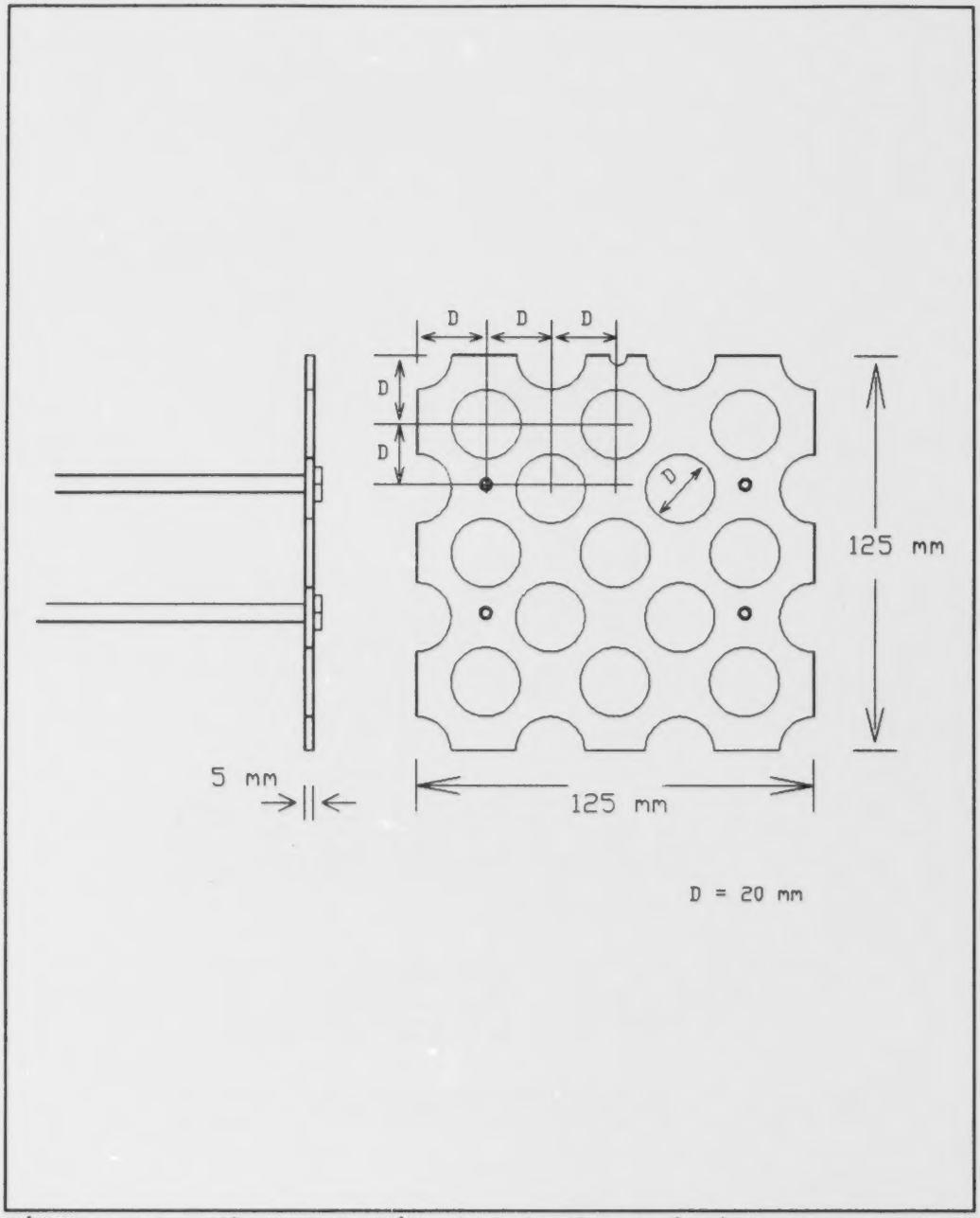

Figure 3.3 : The 20 mm Diameter Perforated Plate.
(20 mm Perforations Are Spaced On Alternate Corners Of A 20 mm Grid. Smaller Holes Are Attachment Points. Small Notch At Top Provides Clearance For Ion Probe.)

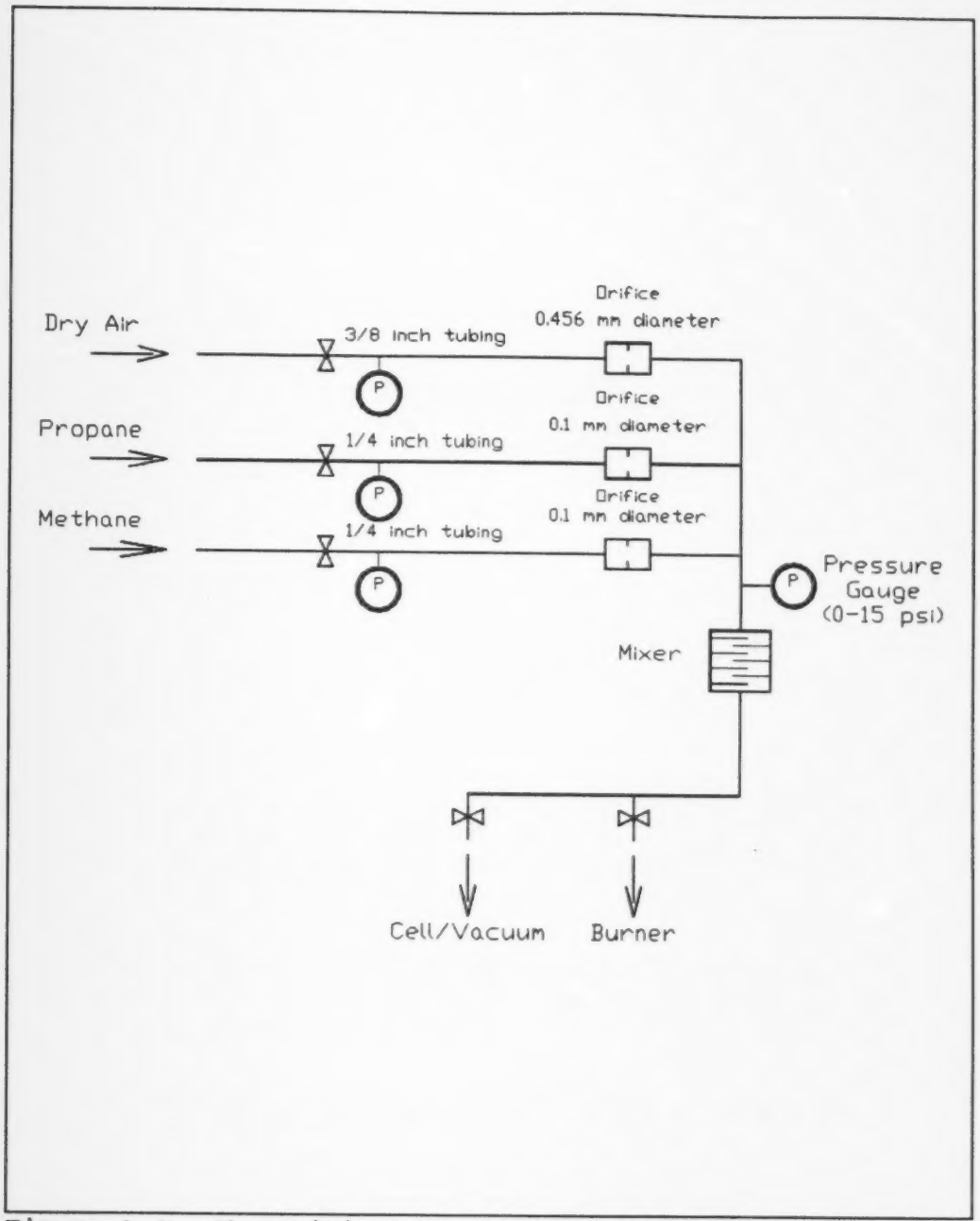

Figure 3.4 : The Critical Flow Orifice Gas Metering And Mixer System.

rates of both the air and the fuel, the mixer mixes the two gases into a homogenous mixture of known mixture stoichiometry. The main components of this apparatus include critical flow orifices, pressure gauges, and a mixer.

The Marsh Master Test pressure gauges measure the upstream and downstream pressures of the orifices. The upstream pressure from the gas cylinder is regulated using a pressure regulator, while the downstream pressure is that of the atmosphere or that of the combustion chamber. The critical flow orifices are made of brass orifice plates with diameters of 0.1 mm for the fuels and 0.456 mm for the air. The flow rate through a critical flow orifice is directly related to the upstream pressure when assuming a constant temperature. The details of calibration and operation are given in Appendix B.

3.1.3 Gas Chromatograph

The gas chromatograph used in this study is a P200 GC manufactured by Microsensor Technology Inc. The software controlling the gas chromatograph is called EZCHROM 3.1 which runs on WINDOWS 3.0 on a IBM compatible 386 computer.

The gas chromatograph operates by injecting a few μL of sample gas into two columns. The columns then elute different components at different times called elution times, with a steady carrier gas flowing through. A thermal conductivity detector responds to the difference in thermal conductivity between the helium carrier gas and the sample components eluting through the detector. The two

columns are Mol Sieve 5A which is used to analyze the hydrogen, oxygen and methane compositions, and Pora Plot Q 2M which is used to analyze the hydrocarbons (methane and propane).

The main advantage of a thermal conductivity detector is that it responds to all substances having a thermal conductivity different from that of the carrier gas [RB73]. It has been shown experimentally [Gr85, Di67] that the relative response factors (where sample weight is used) are independent of,

(1) type of detector (filament or thermistor)

(2) cell and sensor temperature

(3) concentration of sample

(4) helium (carrier gas) flow rate

(5) detector current

The relative response factors used in this study were taken from Dietz [Di67]. These values as tabulated in Table 3.1, have a precision of about ± 3% [Di67]. As the gas chromatograph has the ability to detect down to one part per million, the precision of gas analysis in this study depends on the calibration gas used (about ± .05%).

Oxygen and Argon do not separate in either of the two columns. Therefore, a ratio of 20.8/21.8 was assumed for the oxygen to oxygen plus argon ratio for all tests. However, it was later found from the manufacturer that the extra dry air was made by mixing oxygen with nitrogen with no argon present. If pure oxygen and nitrogen were present and the equivalence ratio was based on fuel and oxygen only, the actual equivalence ratio of methane-air

mixtures used would be about 0.03 lower. However, due to the large amount of inert (≈ 78% nitrogen) present, the actual equivalence ratio was relatively unaffected by this change.

The purpose of the gas chromatograph was to analyze the actual compositions of components present in the combustion gas. The gas chromatograph was used to analyze the fuel to permit equivalence ratio calculations. In addition, it was used to analyze the fuel/air mixture for determining the actual mixture stoichiometry.

Table 3.1 : Relative Response Factors From Dietz [Di67].

Compound	Relative Response Factor
Oxygen	40
Nitrogen	42
Methane	35.7
Propane	64.5
Air	40.1

3.1.4 High Speed Video Camera

The high speed video camera used is a SP2000 Motion Analysis System manufactured by EASTMAN KODAK COMPANY Spin Physics Division. It has a capability of taking 12,000 picture per second in partial frame format. Flame images were formed in the camera using the Schlieren technique as described in Modien [Mo90]. In this study, the camera was used in the full frame format of 2000 frames per

second.

The images from this high speed video are digitized using programs developed at the University of Alberta Mechanical Engineering Department. After passing through Data Translation DT2782 Flame Grabber, the images go through the following programs.

- PASS
- AUSAVE1
- FLASH with Flame Area Option

The program FLASH calculates the area occupied by the outer Schlieren edge of the flame front. The flame radius can then be obtained from the calculated area. The present FLASH program, described in Appendix C, detects a larger flame area than expected. Further improvement of this program is required.

3.2 Procedure

The exact sequence of carrying out the experiment is as follows:

1) Gas Mixer Calibration
2) Ignition System Tests
3) Gas Analysis
4) Pressure Transducer Calibration
5) Quiescent Flame Tests
6) Turbulent Combustion Tests

3.2.1 Gas Mixer Calibration

The original calibration of the choked orifice flow was done

by McDonell [Mc88] in 1986. The re-calibration of air, propane and methane flow rates is detailed in Appendix B.

The upstream air pressure was calibrated to flow rate using a rotameter. The propane and methane flow rates, being too low for rotameter application, were calibrated using a stop watch and a 100 ml burette tube with a rising soap bubble.

The results obtained from the re-calibration showed linear relationships between the flow rates and the upstream pressures. The maximum deviation of flow rate was found to be less than 0.1 l/min for the air and less than 0.02 l/min for the fuels. These calibration data and graphs are presented in Appendix B.

3.2.2 Ignition System Tests

The ignition system used in this study was the high energy capacitance discharge unit as used by Modien [Mo90] and McDonell [Mc88]. Figure 3.5 shows the schematic of the circuit.

A high voltage DC supply unit, capable of supplying up to 2000 V, is used to supply the required voltage. This voltage charges the capacitor bank of variable capacitance (1, 1.5, 2, and 2.5 μF). When the electric trigger pulse activates the SCR, the current discharges through the primary windings of a standard automotive coil to produce the spark.

Two sets of experiments were conducted to obtain the characteristics of this spark ignition system. These tests were conducted with atmospheric air in the combustion chamber.

The first set of tests was carried out with fixed voltage and

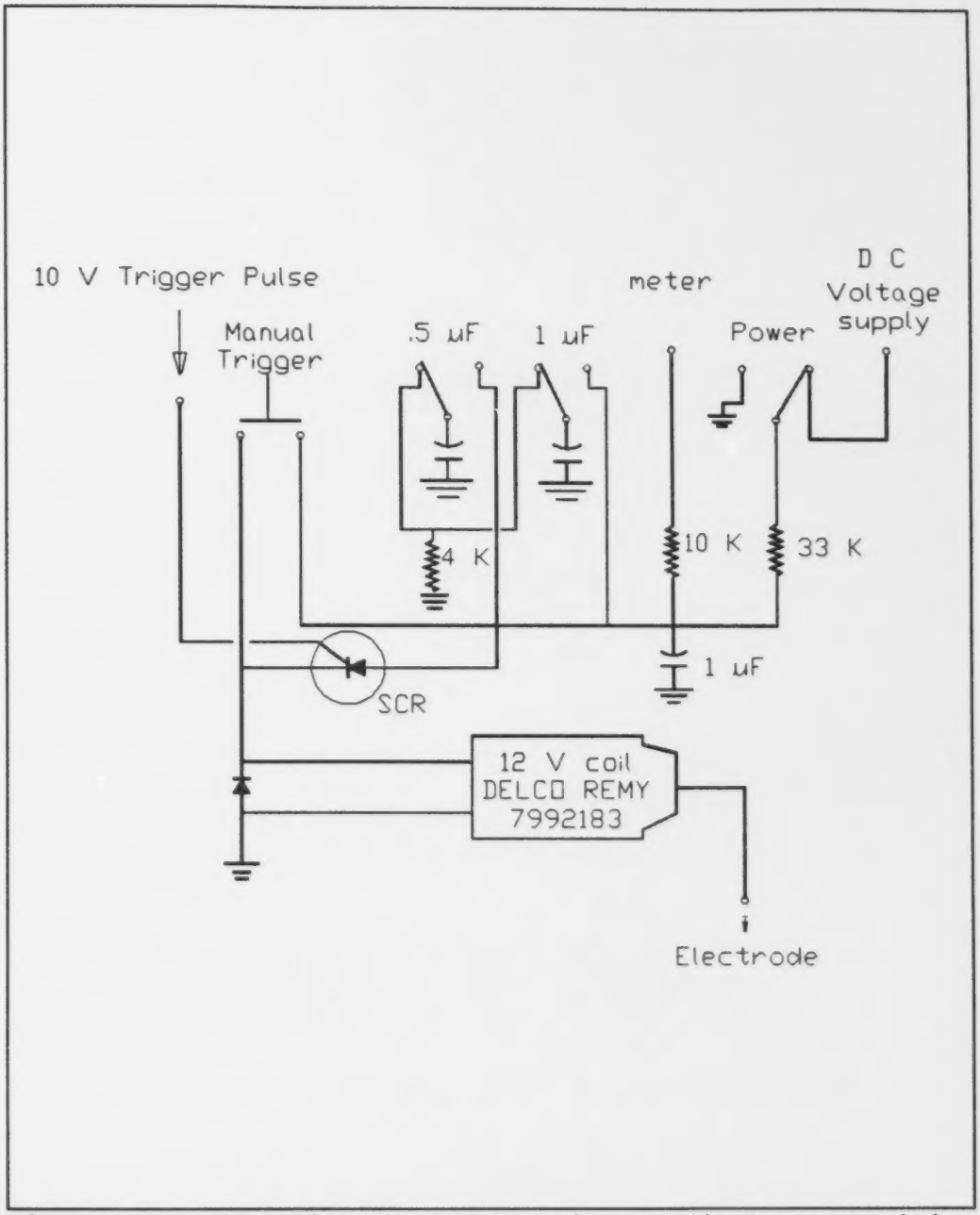

Figure 3.5 : The High Energy Capacitance Discharge Ignition Circuit.

capacitance: 500 V and 2.5 μF respectively. The spark gap was varied from 1 mm to 4.5 mm. The second set of tests was carried out with fixed spark gap of 4.5 mm and fixed capacitance of 2.5 μF while the voltage was varied from 300 V to 600 V.

Voltage and current traces were measured using a Tektronix P6015 1000X 100 MΩ voltage probe with compensating box and an Emerson Electronics model 411 wide band current transformer. The traces were recorded on two two-channel Tektronix oscilloscopes. These traces, presented in Appendix D, are plots of spark voltage and current against spark duration.

For each test, approximately five runs were conducted to obtain an average. As the spark energy was increased, the deviation from run to run also increased. Auto-sparking or spontaneous breakdown was found to occur at some very high spark voltage supply (1000 V, spark gap of 1 mm). The maximum deviation from run to run was less than 20%. There was a 30 second delay between consecutive runs with ten seconds flushing of fresh room air through the combustion chamber.

All measurements and results are presented and discussed in Appendix D. A 4.50 mm spark gap with 312.5 mJ (500 V, 2.5 μF) stored energy was used throughout this study. The reasons behind this choice are presented in Appendix D.

3.2.3 Supply Gas Analysis

Each of the supply gases (extra dry air, methane and propane) was analyzed individually before the actual experiments. As a

result, the actual purity or composition of each supply gas was found. Detailed method settings and calibrations for dry air, methane and propane are given in Appendix E.

Since the columns may be contaminated after a number of analyses, the gas columns were reconditioned from time to time. Reconditioning evaporates the water vapour and the various un-eluted gases accumulated in the columns after a series of runs. Re-conditioning was carried out by heating channel A (Mol Sieve 5A) at 165°C and channel B (Pora Plot Q 2M) at 160°C for about two hours.

Table 3.2 shows the supply gas analysis results. The table shows that the methane used was of high purity (98% pure). Therefore, during the methane-air experiments, the actual mixture composition was that obtained from the GC analysis by assuming 99% pure methane (98.3% methane + 0.7% ethane). The 0.7% ethane was treated as methane and the air/fuel ratio was based on oxygen content and this fuel.

Table 3.2 also shows that the propane (94% pure) was not as high in purity. Depending on how the other hydrocarbons are treated, the GC analysis for propane-air mixture can vary accordingly. The fluctuation from one analysis to another was found to be larger than those in methane-air case. Moreover, the equivalence ratio calculated was very sensitive to small changes in the fuel and/or oxygen analyzed. Therefore, the actual air/fuel ratios used were those of the re-calibrated choked flow values. Despite this problem, the results of mixture composition from GC analysis in both the methane-air and propane-air cases, agreed

within 3% in term of equivalence ratio with those of the choked flow method.

Table 3.2 : Supply Gas Analysis.

Gas	Actual Composition
Dry Air	21.6 % Oxygen (+ Argon), 78.4 % Nitrogen
Methane	1.0 % Nitrogen, 98.3 % Methane, 0.7 % Ethane
Propane	0.8 % Methane, 4.3 % Ethylene, 0.3 % Ethane, 94.2 % Propane, 0.4 % i-Butane

3.2.4 Pressure Transducer Calibration

The pressure transducer used was a Norwood model 111 four-active-arm strain gauge type with a response frequency of 45 kHz. The strain gauge circuit had variable offset and multiple amplification factors of 100, 300, 500, 800 and 1000. Throughout this study, the amplification factor was set at 1000. The pressure transducer and amplifier were calibrated using a dead weight tester before each series of runs. A typical calibration is given in Appendix F.

Throughout this study, pressure was recorded at two levels using two channels of the 4 channel RACAL FM tape recorder as discussed in Section 3.3. Channel 1 was used to record the high resolution pressure by setting the maximum voltage to 1 V unipolar (0 to 2 V). This high resolution pressure record with a maximum

pressure of about 400 kPa enables better burning velocity calculation for early flame growth. Maximum combustion pressure rise was recorded using channel 2 of the RACAL FM tape recorder with maximum voltage set at 5 V unipolar (0 to 10 V).

3.2.5 Quiescent Flame Tests

Laminar burning tests were carried out for both propane-air and methane-air mixtures. For propane-air tests, equivalence ratios of 0.75, 0.90 and 0.95 were studied. For methane-air tests, equivalence ratios of 0.76 and 0.96 were used.

Initial pressure varied from 0.5 atm to 2.6 atm. This range of initial pressure was used to study the pressure effects on burning velocities.

A calibration of the pressure transducer was done prior to each series of tests. Over the series of runs, GC analysis of the mixture was carried out from time to time. Between two consecutive runs, the combustion chamber was evacuated and flushed with the supply gas mixture; this procedure was repeated three times to ensure that the dead volume left in the manifold or the combustion chamber was of the same composition as the supply gas. Four or five runs were repeated for every single test condition.

3.2.6 Turbulent Combustion Tests

Similar to the quiescent flame tests, a pressure calibration using the dead weight tester was done prior to each series of tests. A GC analysis was carried out over the series of runs to

check the mixture stoichiometry. Evacuation of the combustion chamber followed by flushing with the supply mixture was repeated three times between consecutive runs. Every single test condition was repeated three to five times. The actual plate speed and time delay before ignition were recorded in conjunction with the pressure trace.

For propane-air turbulent tests, propane-air mixtures at equivalence ratios of 0.75 and 0.95 were used. The perforated plate with 5 mm diameter holes was used here as the intention was to study the effect of small scale turbulence on burning velocity. Turbulence intensity at ignition was varied from 0 m/s to 4.5 m/s.

For methane-air turbulent tests, gas mixtures with equivalence ratios of 0.76 and 0.96 were used. Using the perforated plate with 20 mm diameter holes, the turbulence intensity at ignition was varied from 0 m/s to 7 m/s.

More variables were involved in turbulent combustion tests compared with the laminar runs. To reduce variability, runs where the actual plate speed was more than ± 5% from the required average were rejected. Moreover, any run with burning velocity variation of more than ± 5% at 110 mm diameter flame was rejected. This procedure prevented the inclusion of any wild data due to noise. This selecting criterion also resulted in using two to five runs for averaging any data point.

3.3 Data Collection And Analysis

All experimental data were first recorded using a 4 channel

RACAL FM tape recorder. It was then digitized for storage and analysis on a IBM compatible 386 computer. There are a number of advantages for following the procedure. First, a faster data acquisition rate was achieved by recording at a high speed of 30 ips and playback at a much lower speed of 1.875 ips for digitization. This process effectively increased the digitization rate by a factor of 16. Secondly, the adverse effects of electrical "noise" on the digital computer when operating adjacent to the high energy ignition systems were eliminated. Thirdly, the FM recorder had high frequency cutoff filters which filtered out high frequency noise above 40 kHz. Finally, the FM tape recorder also allowed simultaneous recording of pressure at two levels.

3.3.1 Quiescent Runs

Figure 3.6 shows the paths of data collection in quiescent or turbulent tests. The four channels used in quiescent tests are listed in Table 3.3. The stored data from the FM tape was digitized at a frequency of 4000 Hz (3000 Hz for the slower burning mixtures) using a Metrabyte DASH8 board in a 386 computer. The detailed digitization procedure is given in Appendix G.

The analysis used for measuring the burning velocity was the multi-zone model as described in Chapter 2. No compression or smoothing of the pressure trace was done before the burning velocity analysis. This was to eliminate possible error introduced by compression or smoothing routines.

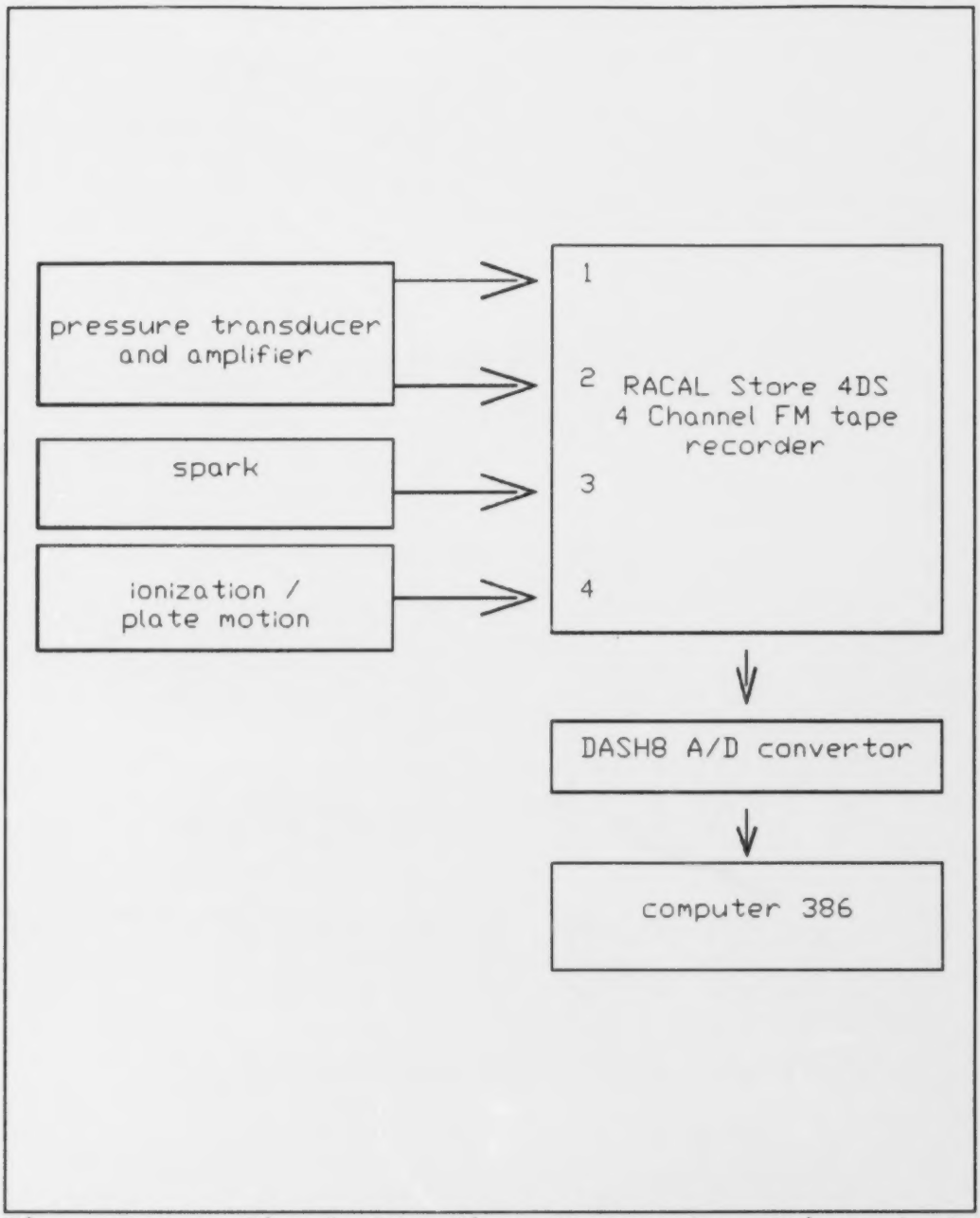

Figure 3.6 : Signal Recording Summary For Quiescent Or Turbulent Runs.

Table 3.3 : Channel Inputs For Quiescent Runs.

Channel	Range (V) unipolar	Function
1	0 to 2	high resolution pressure
2	0 to 10	maximum pressure
3	0 to 10	spark
4	0 to 10	ionization

3.3.2 Turbulent Runs

Due to the complexity of turbulent runs, the actual plate motion was also recorded as shown in Figure 3.6. The plate motion measurement, detailed in McDonell [Mc88], used optical sensors to record the passage of a stirrup which was attached to the perforated plate. The motion of the perforated plate was sensed by a phototransistor focused on alternating black and white markers at 10 mm intervals on the stirrup directly attached to the plate.

Table 3.4 lists the functions of the four channels on the FM tape recorder. Digitization of the stored data from the FM tape was done with a 386 computer using a DASH8 board running at 4000 Hz for an effective digitization rate of 64 kHz. Parameters such as the actual plate speed and the actual spark delay time (time from the plate passing the spark gap till spark ignition) were measured from the FM tape record to calculate the actual turbulence intensity and eddy scales for each run.

Table 3.4 : Channel Inputs For Turbulent Runs.

Channel #	Range (V) unipolar	Function
1	0 to 2	high resolution pressure
2	0 to 10	maximum pressure
3	0 to 10	spark
4	0 to 10	plate motion

CHAPTER 4: QUIESCENT FLAME RESULTS AND ANALYSIS

This chapter presents all useful results obtained from the quiescent flame tests. The laminar burning velocities presented in this chapter are used to normalize the turbulent burning velocities in Chapter 5.

Quiescent burning of lean propane-air and lean methane-air flames was investigated in this study. The initial temperature was fixed at 296 K (±1 K) while the initial pressure was varied from 0.5 atm to 2.6 atm.

From the pressure trace, the multi-zone thermodynamic equilibrium model described in Chapter 2 was used to calculate burning velocities for 47 mm radius (P = 135 kPa, T_u = 320 K) and 55 mm radius (P = 170 kPa, T_u = 340 K) flames. These values were obtained from a linear fit line of burning velocity against relative flame radius, r/R_{bomb}, over the range 0.55 to 0.75. This particular range of relative radii was chosen for two reasons. First, within this range the flame is large compared with its thickness and curvature. Therefore, the one dimensional, thin flame assumption is good. Second, the pressure trace analysis is capable of producing consistent results over this range of detectable pressure rise, with signal about two orders of magnitude larger than the noise. A flame with relative radius of more than 0.75 was not used to ensure that the flame front was not in contact with the walls. Ideally, for a perfectly spherical flame propagating from the center of the chamber, contact with the walls would occur at a relative radius of 0.8 (r = 61 mm).

Burning velocity is known to be affected by both pressure and temperature. These pressure and temperature effects on laminar burning velocity can be expressed as Equation 4.1 over particular ranges of pressure and temperature.

$$S_u = S_{u0} \left(\frac{P}{P_i}\right)^a \left(\frac{T}{T_i}\right)^b \qquad 4.1$$

where S_{u0} = reference laminar burning velocity at 1 atm and 298 K

P_i = initial or reference pressure, 1 atm

T_i = initial or reference temperature, 298 K

a, b = pressure and temperature exponents respectively

4.1 Laminar Burning Velocities Of Lean Propane-Air Mixtures

The laminar burning velocities of 75%, 90%, and 95% stoichiometric propane-air flames were studied. Tables 4.1, 4.2, and 4.3 show the respective results obtained from the pressure trace analysis.

Effects of initial pressure on maximum pressure rise, P_{max}, time required to achieve P_{max}, $Time_{Pmax}$, and normalized maximum pressure rise, P_{max}/P_i were investigated. The results for lean propane-air mixtures of Ø = 0.75, 0.90 and 0.95 are shown in Figures 4.1, 4.2 and 4.3 respectively. These figures show that for the pressure range considered, there is a linear relationship between P_{max} and P_i as expected. As the mixture approaches stoichiometric composition from the lean side, comparing Figures 4.1, 4.2

Table 4.1 : Summary Results Of 75% Stoichimetric Propane-air Quiescent Flames.

P_i (kPa)	51	76	101	127	152	177
P_{max}						
(kPa)	256	481	712	931	1162	1387
(ms)	74.9	82.9	93.7	104.1	107.4	112.9
T_u = 320 K, r/R_{bomb} = 0.61, r = 47 mm						
S_u (m/s)	0.461	0.312	0.251	0.245	0.197	0.184
P (kPa)	68	102	136	170	204	238
t (ms)	44.2	41.0	39.2	40.3	39.0	39.7
T_u = 340 K, r/R_{bomb} = 0.72, r = 55 mm						
S_u (m/s)	0.500	0.429	0.332	0.253	0.231	0.209
P (kPa)	85	127	171	213	257	297
t (ms)	48.0	46.1	45.1	47.9	47.9	49.0

Table 4.2 : Summary Results Of 90% Stoichiometric Propane-Air Quiescent Flames.

P_i (kPa)	51	101	152
P_{max}			
(kPa)	315	827	1350
(ms)	46.8	58.2	65.4
T_u = 320 K, r/R_{bomb} = 0.62, r = 47 mm			
S_u (m/s)	0.726	0.378	0.286
P (kPa)	68	138	207
t (ms)	26.8	25.4	24.0
T_u = 340 K, r/R_{bomb} = 0.72, r = 55 mm			
S_u (m/s)	0.727	0.467	0.348
P (kPa)	86	173	261
t (ms)	29.1	28.9	29.2

Table 4.3 : Summary Results Of 95% Stoichiometric Propane-Air Quiescent Flames.

P_i (kPa)	76	101	127	152	177
P_{max}					
(kPa)	565	830	1073	1351	1602
(ms)	49.0	52.4	53.9	55.7	57.1
T_u = 320 K, r/R_{bomb} = 0.61, r = 47 mm					
S_u (m/s)	0.396	0.412	0.374	0.319	0.314
P (kPa)	102	136	170	205	239
t (ms)	21.4	21.8	19.9	19.4	19.9
T_u = 340 K, r/R_{bomb} = 0.72, r = 55 mm					
S_u (m/s)	0.571	0.484	0.396	0.359	0.343
P (kPa)	128	173	215	258	302
t (ms)	24.9	25.3	24.2	24.1	24.8

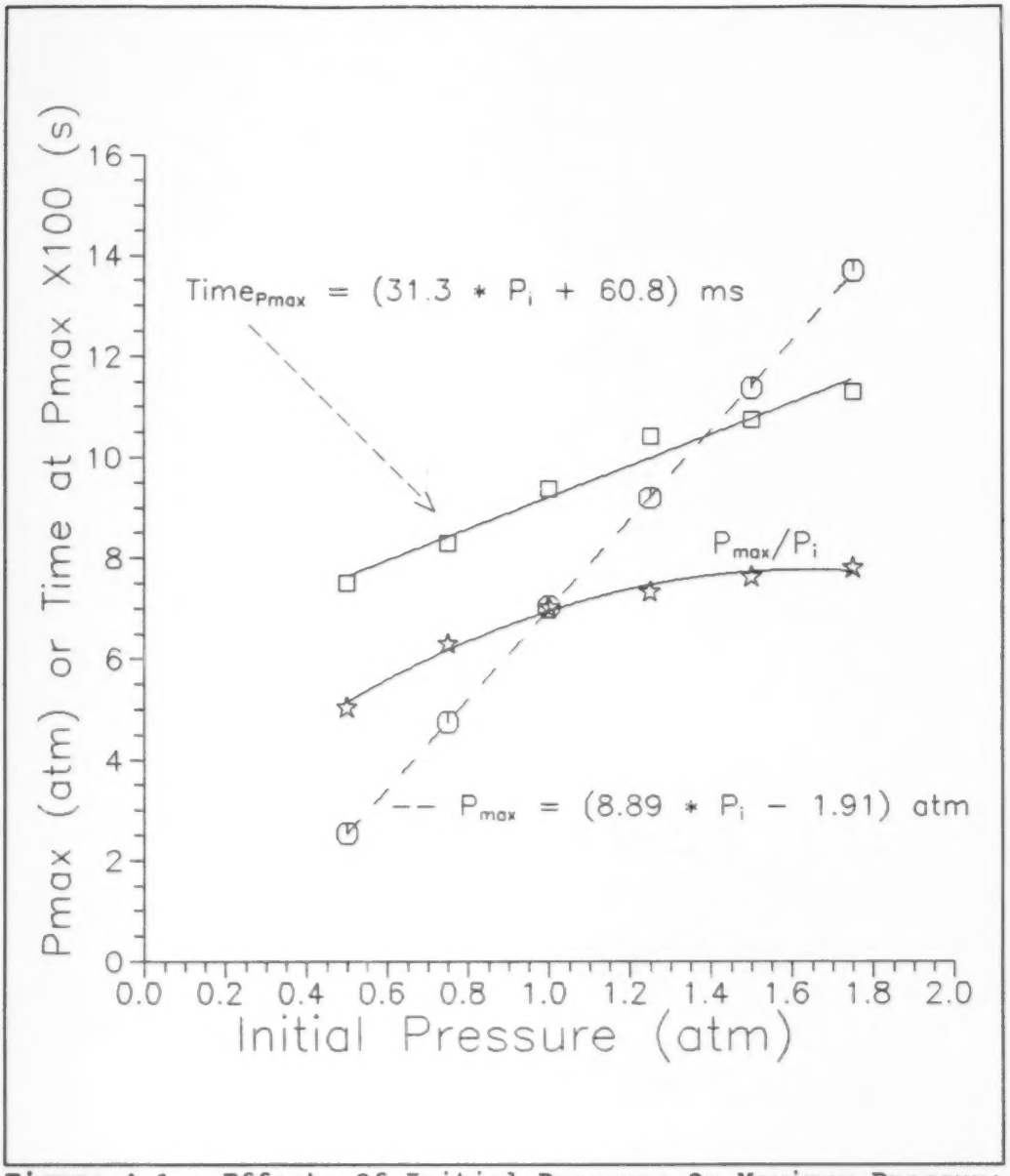

Figure 4.1 : Effects Of Initial Pressure On Maximum Pressure Rise And Time Of Peak Pressure For 75% Stoichiometric Propane-Air Flames.

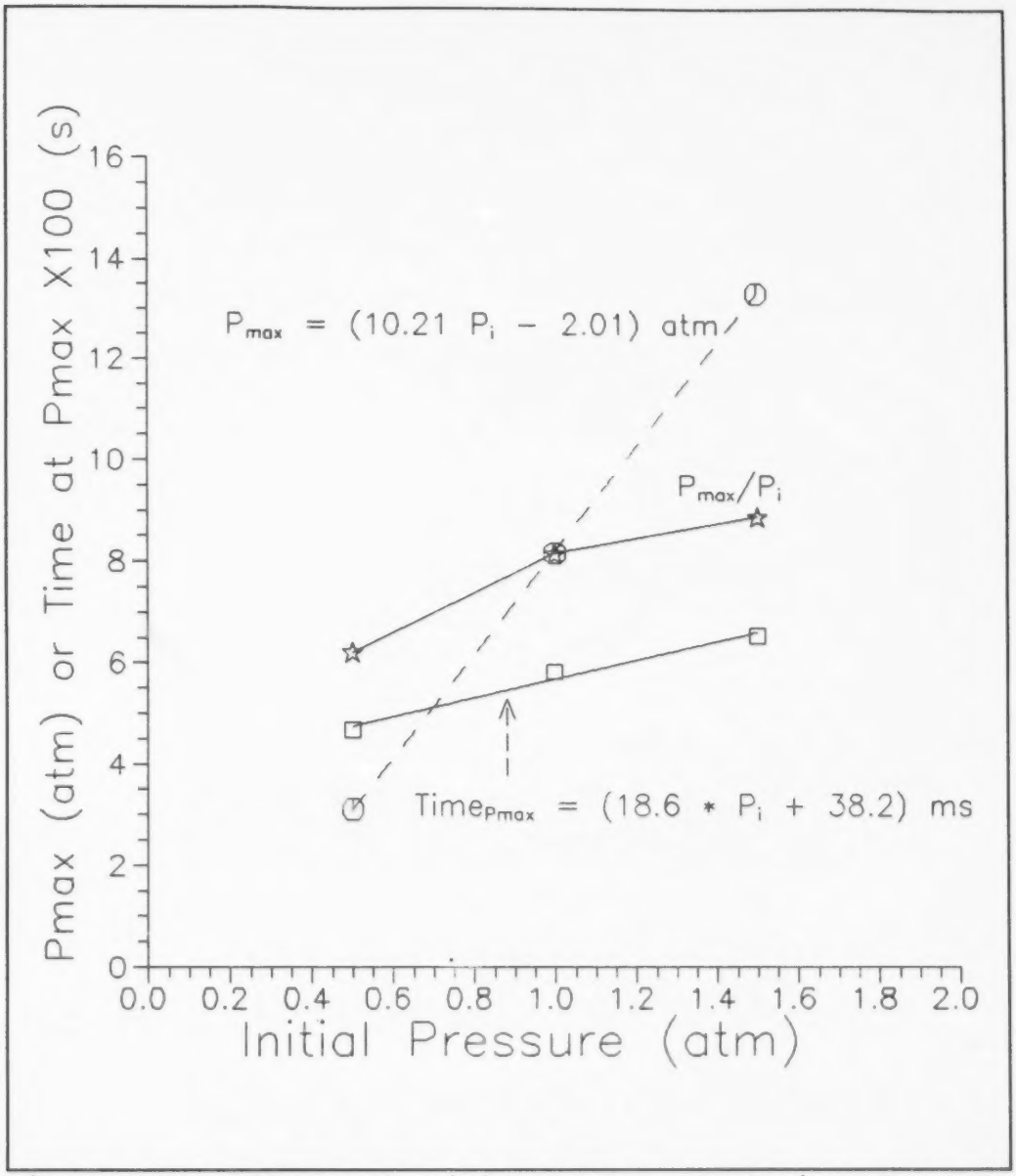

Figure 4.2 : Effects Of Initial Pressure On Maximum Pressure Rise And Time Of Peak Pressure For 90% Stoichiometric Propane-Air Flames.

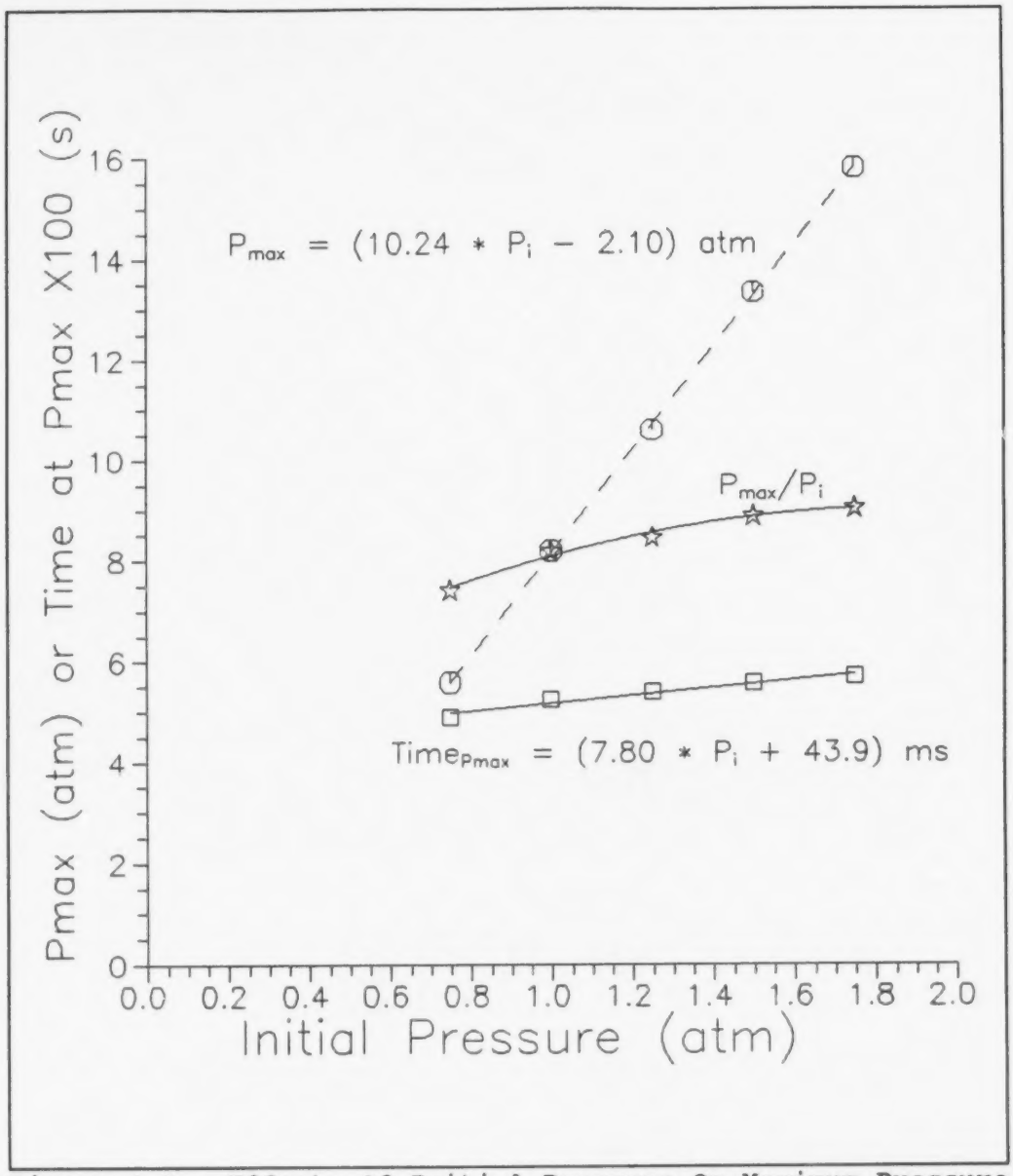

Figure 4.3 : Effects Of Initial Pressure On Maximum Pressure Rise And Time Of Peak Pressure For 95% Stoichiometric Propane-Air Flames.

and 4.3, the slope of the linear relationship increases.

Similar to the P_{max} and P_i relationship, the time required to achieve P_{max}, $Time_{Pmax}$, increases with increasing P_i. However, the slope of the relationship, comparing Figures 4.1, 4.2 and 4.3, decreases as the mixture approaches stoichiometry. This trend is opposite to the trend of P_{max} as expected.

The normalized peak pressure, P_{max}/P_i, shown in Figures 4.1, 4.2 and 4.3 increases with initial pressure. However, due to lower burning velocity at higher pressure, the gradient of P_{max}/P_i with respect to P_i decreases with increasing P_i. The lower burning velocity increases combustion duration which allows a longer heat loss period. Therefore, there is more heat loss for higher pressure tests.

The effects of pressure on laminar burning velocities of 75%, 90% and 95% stoichiometric propane-air flames are shown in Figures 4.4, 4.5 and 4.6 respectively. Burning velocities were calculated for both 47 mm and 55 mm radius flames. These figures show that, for the same flame size and T_u, the laminar burning velocity, S_u, is much higher at low pressures. A power-law of the form

$$S_u = S_{u0} \left(\frac{P}{P_i}\right)^a \qquad 4.2$$

as from Equation 4.1 was used to express the relationship between laminar burning velocity and pressure.

The dependence of the pressure exponent on equivalence ratio for 47 mm and 55 mm radius flames is plotted in Figures 4.7 and 4.8 respectively. Figure 4.7 shows no specific trend for the pressure

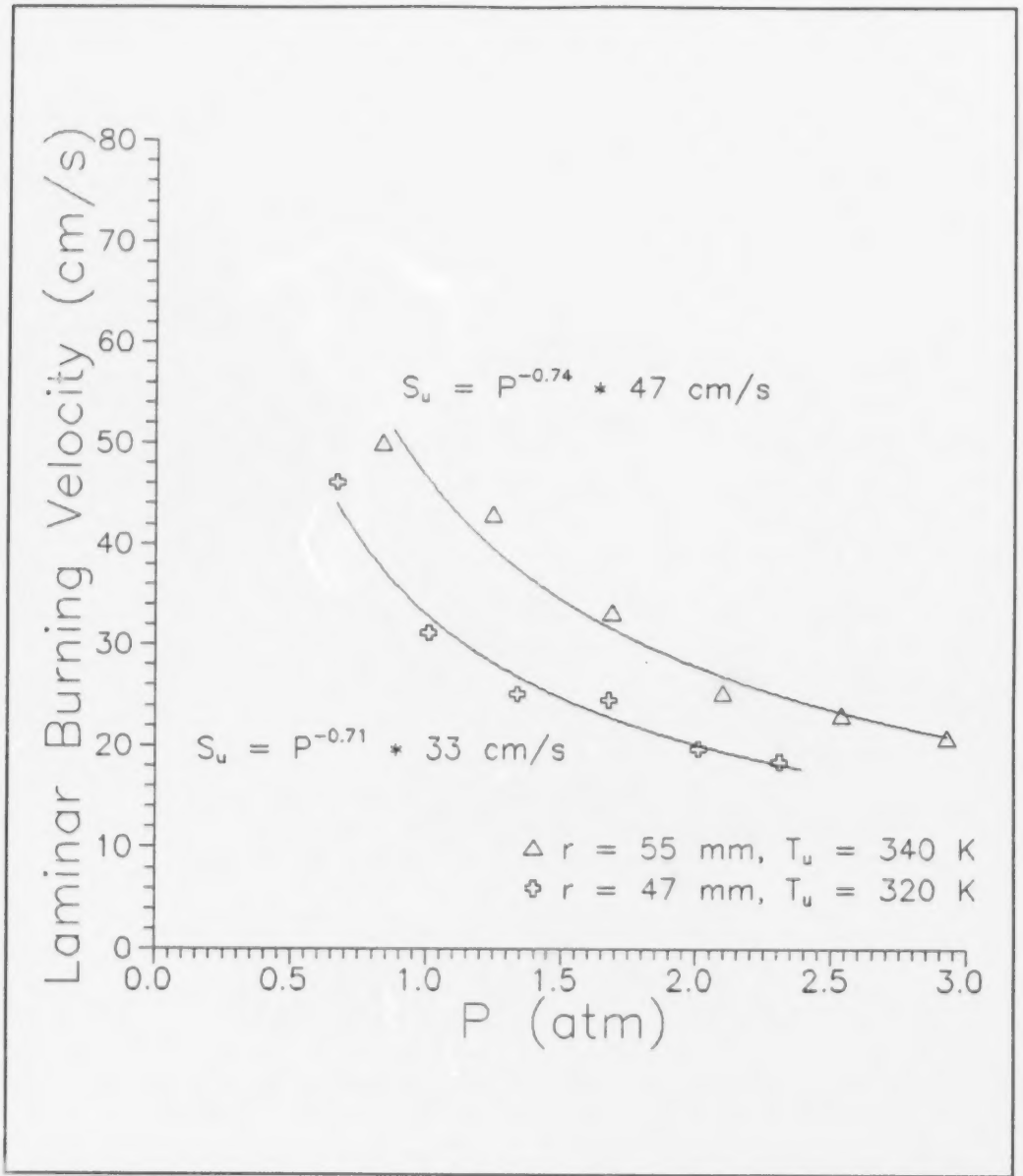

Figure 4.4 : Effect Of Pressure On Burning Velocity Of 75% Stoichiometric Propane-Air Flames.

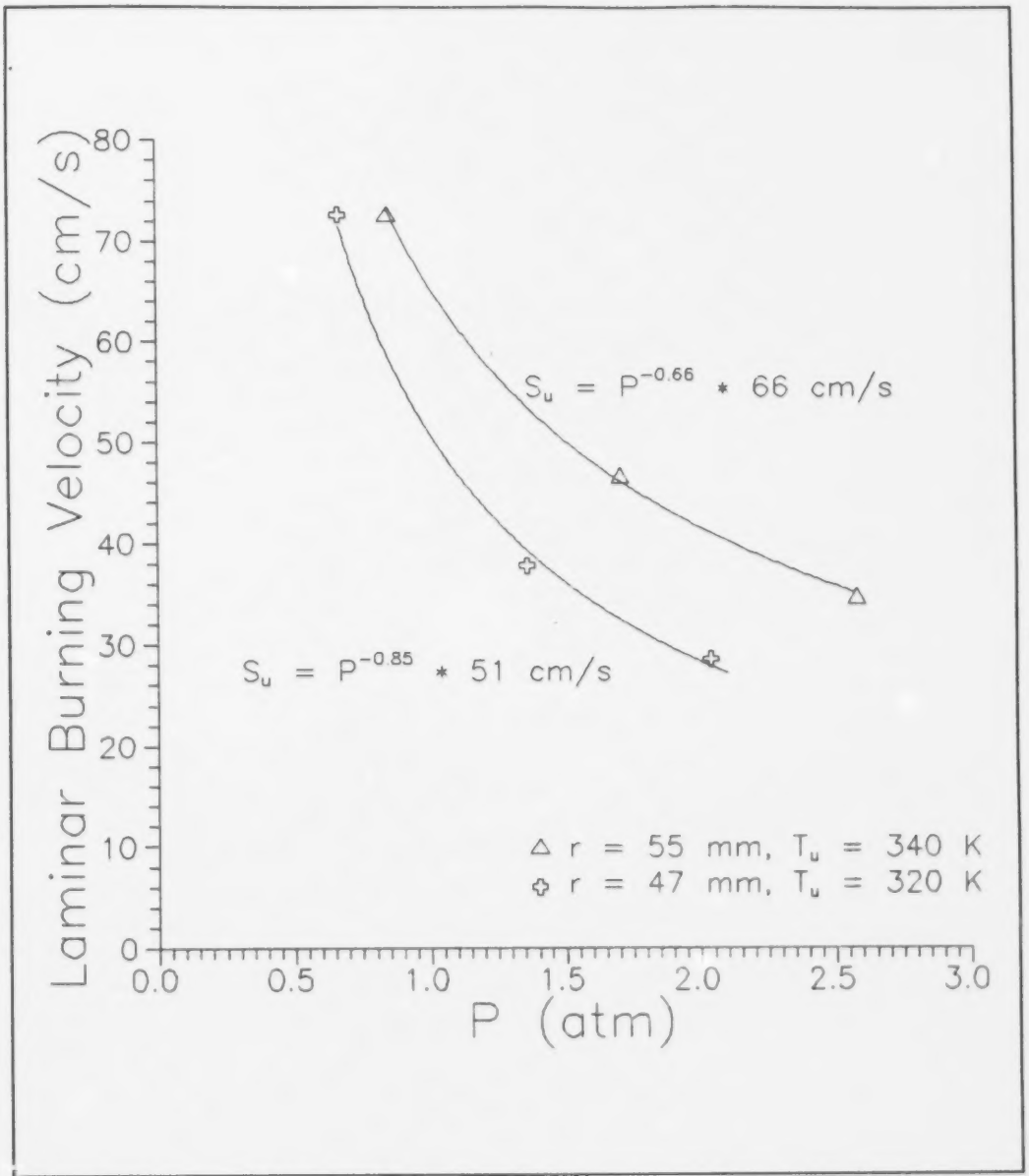

Figure 4.5 : Effect Of Pressure On Burning Velocity Of 90% Stoichiometric Propane-Air Flames.

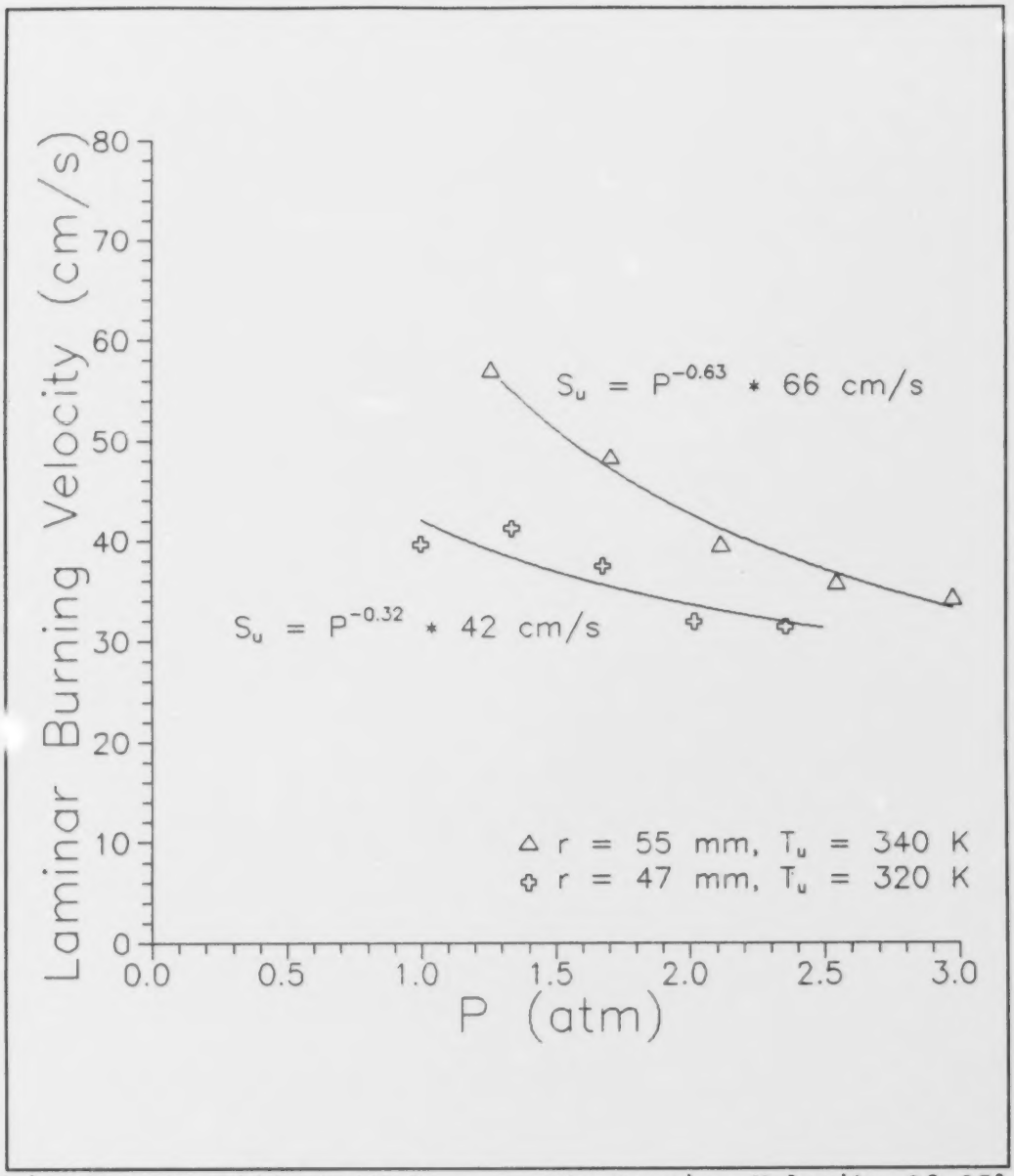

Figure 4.6 : Effect Of Pressure On Burning Velocity Of 95% Stoichiometric Propane-Air Flames.

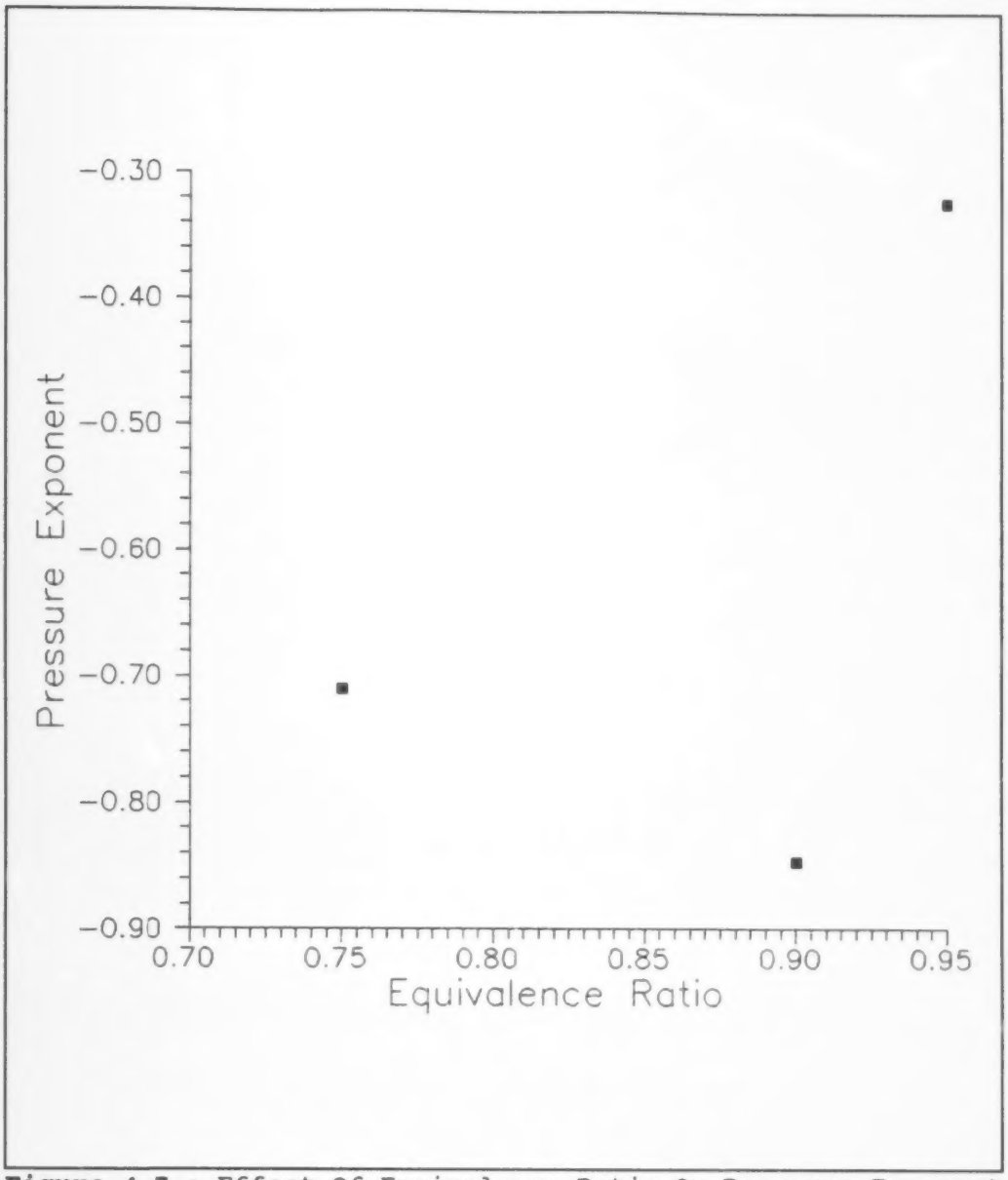

Figure 4.7 : Effect Of Equivalence Ratio On Pressure Exponent Of Lean Propane-Air Flames At r = 47 mm (T_u = 320 K).

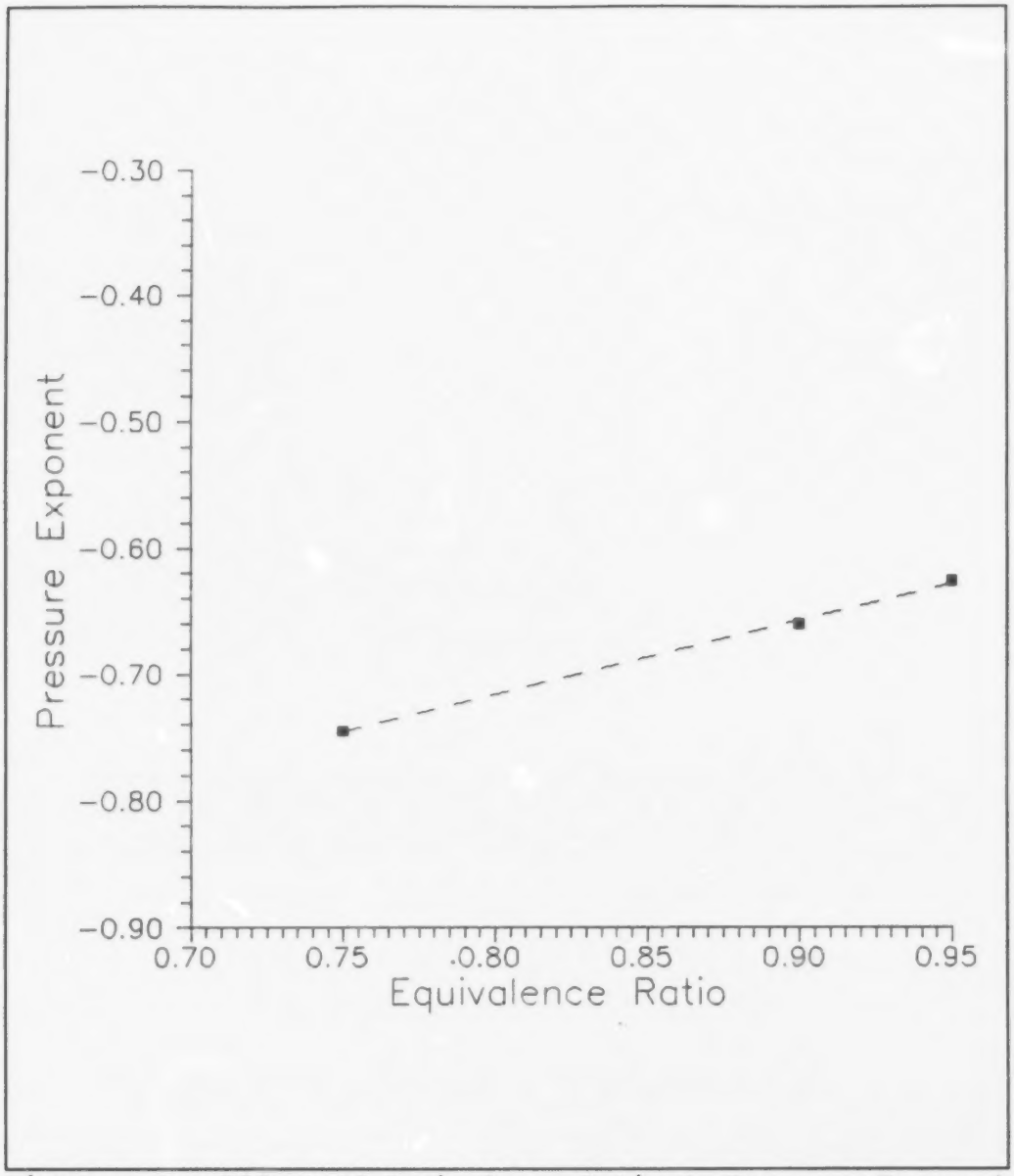

Figure 4.8 : Effect Of Equivalence Ratio On Pressure Exponent Of Lean Propane-Air Flames At r = 55 mm (T_u = 340 K).

exponent and equivalence ratio relation for 47 mm radius flames. The values for the pressure exponent are scattered. The scatter is caused by both the original scatter in Figures 4.4, 4.5 and 4.6, and the limited points used in Figure 4.5. However, the average is -0.6.

The pressure exponent for 55 mm radius flames becomes less negative with increasing equivalence ratio as shown in Figure 4.8. This trend is more evident at r = 55 mm because of less scattering in Figures 4.4, 4.5 and 4.6. At r = 55 mm, the flame is larger and the pressure rise is higher compared with that at r = 47 mm.

Previous studies such as [MK80, AG61, Ku60, Gi57] found that the pressure exponents for propane-air flames, expressed as Equation 4.1, varied from -0.1 to -0.3. These studies also found that the near stoichiometric or faster burning propane-air flames had less negative exponents. More recent study by Okajima et al [OI84] found that the pressure exponent of propane-air flames, varied from -0.1 to -0.7 as the burning velocity decreased from 70 cm/s to 8 cm/s.

The present pressure exponents are more negative than those obtained by others. There is one possible reason for this discrepancy. The range of initial pressure used here (0.5 to 1.75 atm) is very narrow compared with those used by Metghalchi and Keck [MK80] (0.4 to 40 atm) and Agnew and Graiff [AG61] (0.5 to 20 atm).

Table 4.4 shows the comparisons between the present results and the burning velocities at 1 atm obtained by Kuehl [Ku60]. The

present burning velocities for 47 mm radius flames with unburnt temperature of 320 K agreed well with those obtained by Kuehl. The burning velocities of 55 mm radius flames with T_u = 340 K , appeared to be slightly higher.

Table 4.4 : Comparing Laminar Burning velocities Of Propane-Air Flames.

Ø	0.75				0.95			
T_u (K)	311	320	340	478	311	320	340	478
Present S_u(cm/s)		33	48			42	66	
Kuehl S_u(cm/s)	30			65	40			85

In short, the present results seem to show a larger pressure effect compared with other studies. The reasons behind this larger effect have not been resolved. Despite the discrepancy between the present study and those of others, the fact that pressure dependence decreases with increasing equivalence ratio (faster burning) for lean propane-air mixture was consistent in all these studies.

4.2 Laminar Burning Velocities Of Lean Methane-Air Mixtures

The laminar burning velocities of 76% and 96% stoichiometric methane-air flames were studied. The initial temperature was fixed

at 296 K while the initial pressure was varied from 0.6 to 2.6 atm. The results for 76% and 96% stoichiometric methane-air flames are tabulated in Tables 4.5 and 4.6 respectively. Figures 4.9 and 4.10 show the corresponding results for 76% and 96% stoichiometric methane-air flames.

Figures 4.9 and 4.10 show that both P_{max} and $Time_{Pmax}$ increase linearly with increasing initial pressure. This is similar to the case of propane-air just discussed. The high consistency of the measurements is shown by small scattering of data points.

The normalized peak pressure, P_{max}/P_i, shown in Figures 4.9 and 4.10, increases with P_i. However, similar to the propane-air case, the gradient of P_{max}/P_i with respect to P_i decreases with increasing P_i. As pressure increases, the burning velocity decreases. The decrease in burning velocity allows longer combustion duration. As a result, there is more heat loss for higher pressure tests.

The effect of equivalence ratio on the P_{max} and $Time_{Pmax}$ with P_i relationships can be seen by comparing Figure 4.9 with Figure 4.10. As the mixture approaches stoichiometric composition from $\emptyset$ = 0.76 to $\emptyset$ = 0.96, the rise in P_{max} per unit rise in P_i increases. On the other hand, the rise in $Time_{Pmax}$ per unit P_i rise decreases. Similar to the lean propane-air case, these trends (increasing gradient of P_{max} and decreasing gradient of $Time_{Pmax}$ with respect to P_i) are likely due to faster burning for richer mixtures.

Figure 4.11 and Figure 4.12 show the effect of pressure on burning velocities of 46 mm (T_u = 320 K) and 55 mm (T_u = 340 K) radius flames respectively. Both figures show much higher burning

Table 4.5 : Summary Results Of 76% Stoichiometric Methane-Air Quiescent Flames.

P_i (kPa)	61	101	142	182	223	263
P_{max}					range	range
(kPa)	334	668	1005	1355	exceeded	exceeded
(ms)	86.9	108.8	126.4	145.0		
T_u = 320 K, r/R_{bomb} = 0.61, r = 47 mm						
S_u (m/s)	0.289	0.248	0.177	0.157	0.126	0.118
P (kPa)	81	135	189	243	297	349
t (ms)	41.5	41.3	42.3	46.1	50.2	54.6
T_u = 340 K, r/R_{bomb} = 0.72, r = 55 mm						
S_u (m/s)	0.371	0.251	0.197	0.169	0.147	0.129
P (kPa)	101	169	236	303	370	437
t (ms)	47.9	49.3	53.0	58.2	64.1	70.5

Table 4.6 : Summary Results Of 96% Stoichiometric Methane-Air Quiescent Flames.

P_i (kPa)	61	101	142	182	223
P_{max} (kPa)	399	772	1197	1567	range exceeded
(ms)	54.8	62.3	69.4	70.7	
T_u = 320 K, r/R_{bomb} = 0.60, r = 46 mm					
S_u (m/s)	0.518	0.393	0.315	0.291	0.258
P (kPa)	81	135	189	242	296
t (ms)	25.5	24.1	22.9	21.8	22.4
T_u 340 K, r/R_{bomb} = 0.72, r = 55 mm					
S_u (m/s)	0.610	0.413	0.335	0.313	0.289
P (kPa)	101	169	237	302	370
t (ms)	28.8	28.2	28.3	27.2	28.4

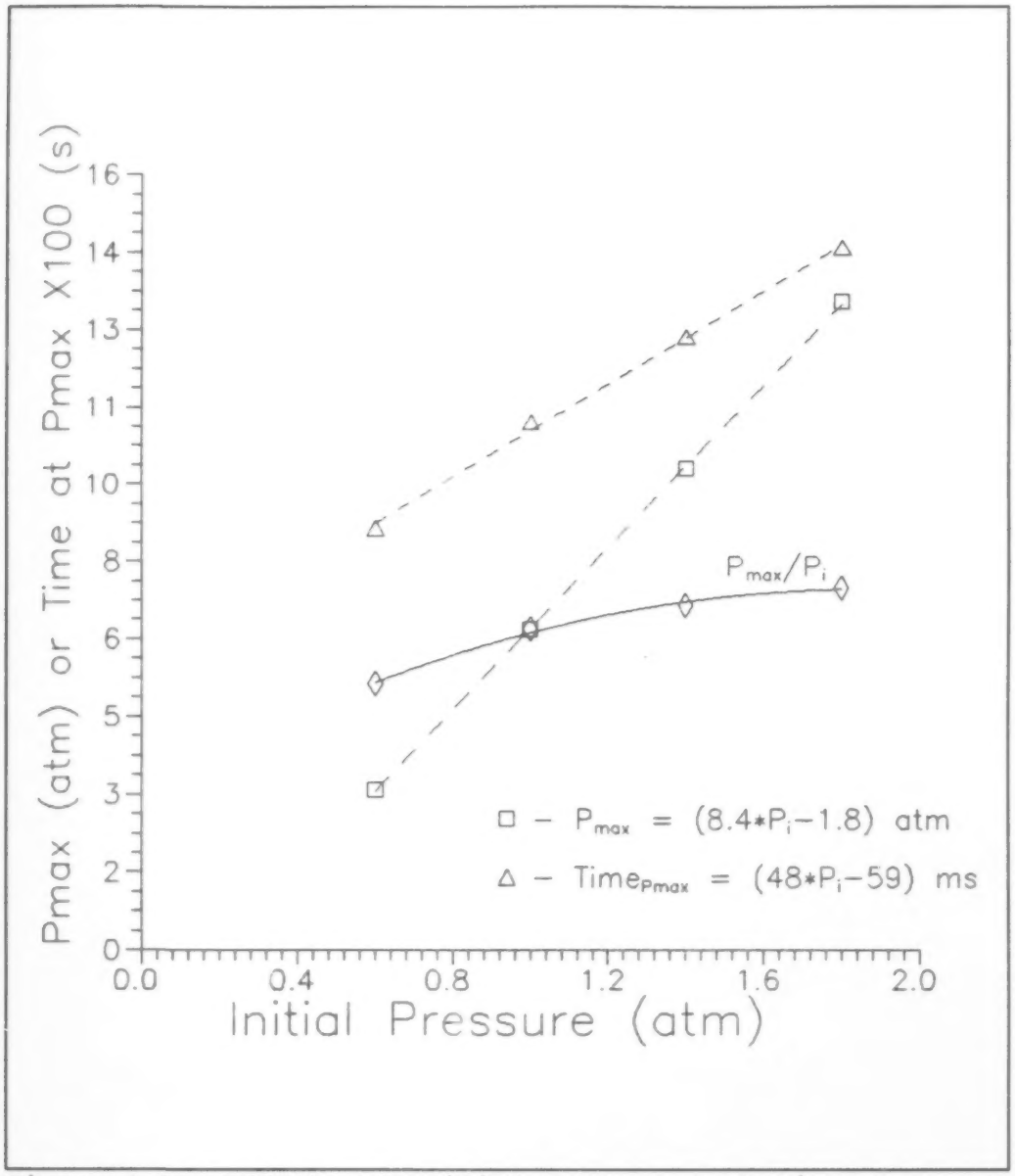

Figure 4.9 : Effects Of Initial Pressure On Maximum Pressure Rise And Time Of Peak Pressure For 76% Stoichiometric Methane-Air Flames.

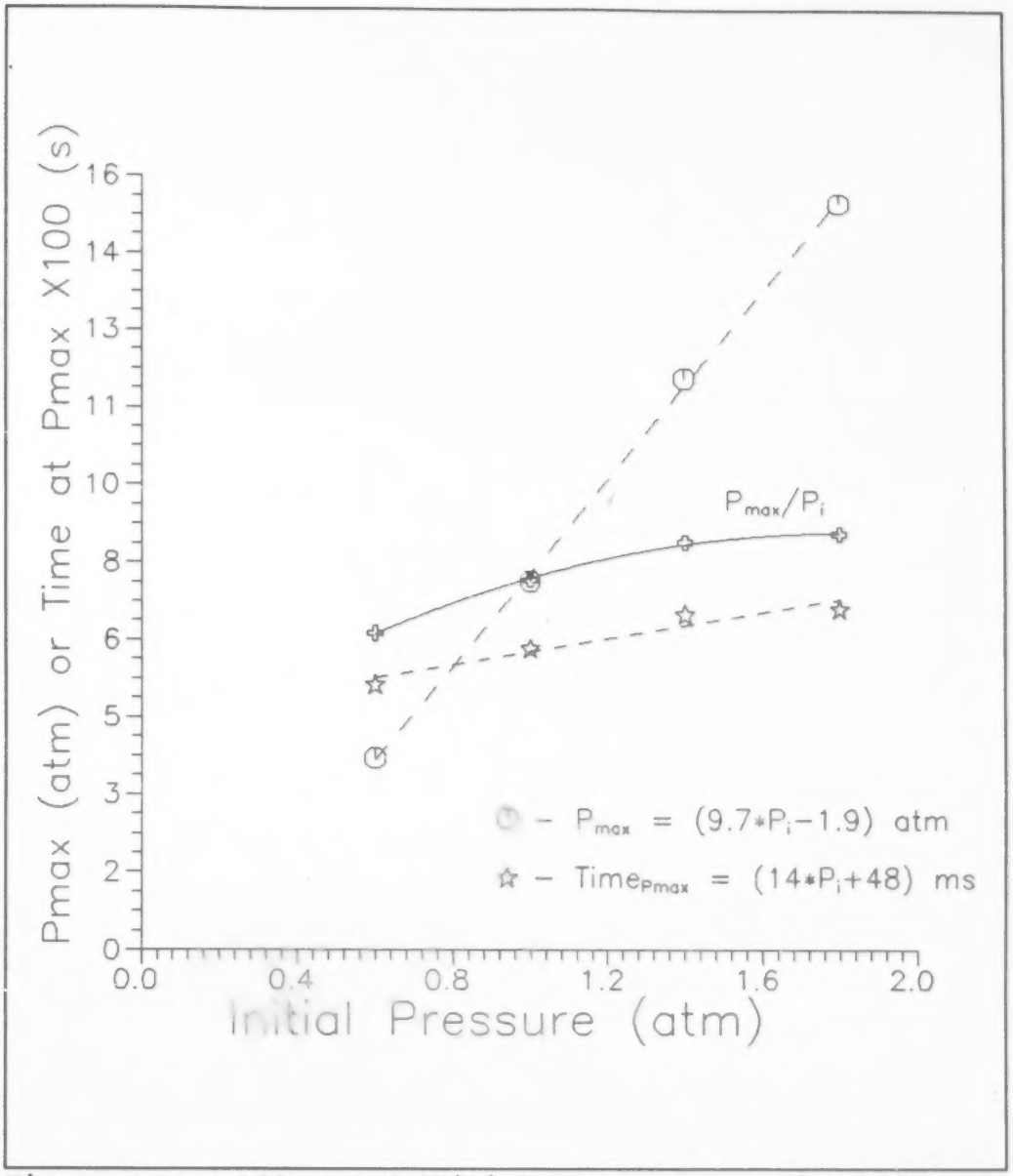

Figure 4.10 : Effects Of Initial Pressure On Maximum Pressure Rise And Time Of Peak Pressure For 96% Stoichiometric Methane-Air Flames.

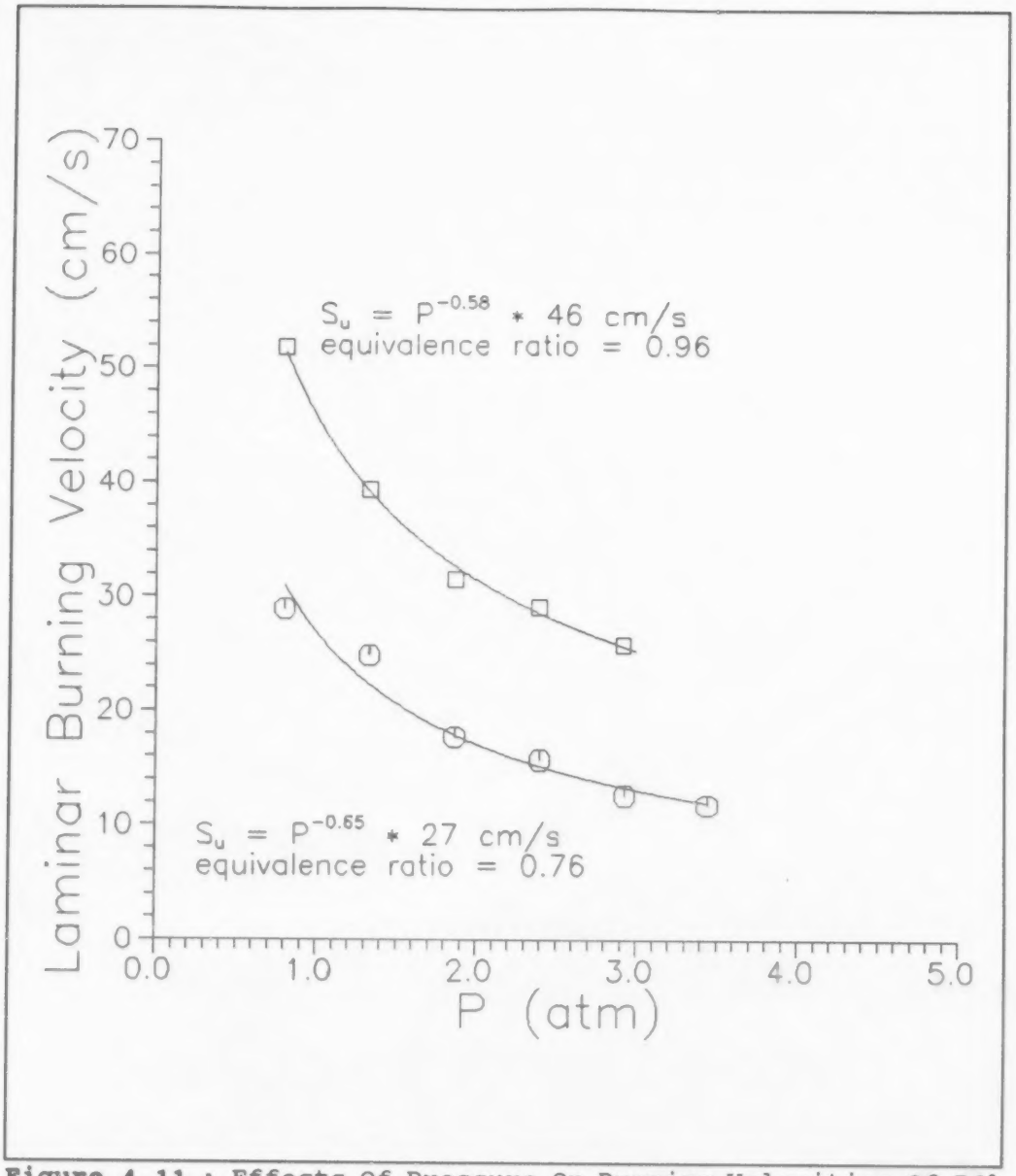

Figure 4.11 : Effects Of Pressure On Burning Velocities Of 76% and 96% Stoichiometric Methane-Air Flames At r = 47 mm (T_u = 320 K).

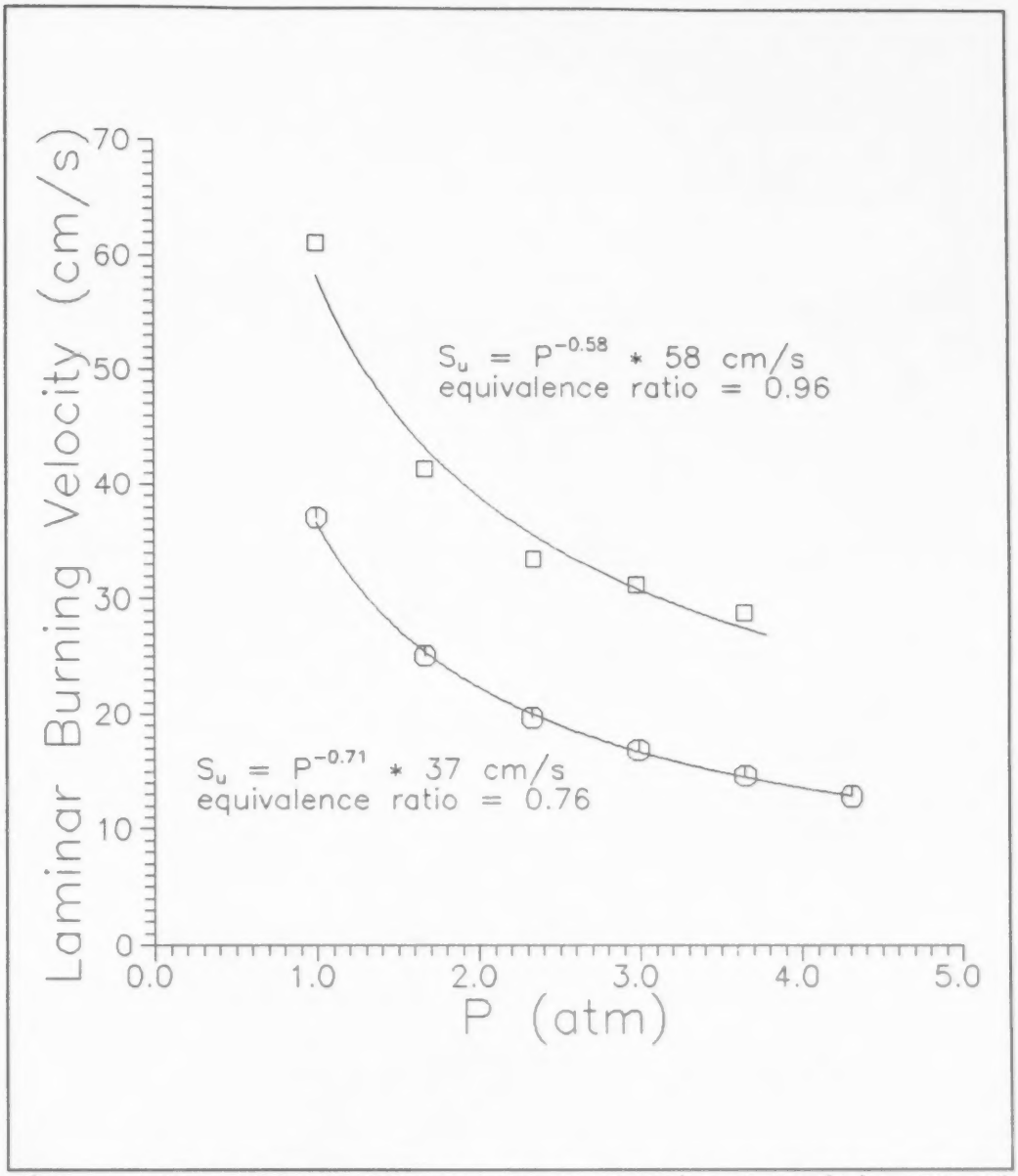

Figure 4.12 : Effects Of Pressure On Burning Velocities Of 76% and 96% Stoichiometric Methane-Air Flames At r = 55 mm (T_u = 340 K).

velocities at lower pressures. This behavior is fitted with the power law equation, Equation 4.2. The absolute value of the pressure exponent decreases as the mixture becomes richer.

Rallis and Garforth [RG80] obtained the following results from their study of stoichiometric methane-air at about 300 K :

$$S_u = 38\ P^{-0.145}\ cm/s \quad for\ P < 0.6\ atm \qquad 4.3$$

$$S_u = 36\ P^{-0.265}\ cm/s \quad for\ 0.6 < P < 3\ atm \qquad 4.4$$

$$S_u = 46\ P^{-0.51}\ cm/s \quad for\ 3 < P < 10\ atm \qquad 4.5$$

An earlier, experimental study of Bradley and Hundy [BH71] obtained a pressure exponent of -0.5. This pressure exponent of -0.5 was obtained from burning stoichiometric methane-air mixtures in a closed vessel with pressure varied from 0.25 to 1.5 atm. Bradley and Hundy also found this pressure exponent of -0.5 to be valid for pressure up to 60 atm.

The pressure exponents were found to vary from -0.58 to -0.71 in this study. These pressure exponents are more negative compared with those of [RG80] and [BH71].

Figure 4.13 shows the effects of equivalence ratio and temperature on the burning velocity of methane-air mixtures. The laminar burning velocity of 47 mm radius, 76% stoichiometric methane-air flames agreed reasonably with those obtained by Rallis and Garforth [RG80], and Abdel-Gayed and Bradley [AB72]. The laminar burning velocities of 55 mm radius flames are higher than those of 47 mm radius flames and higher than typical literature values. The main reason behind this higher burning velocities at

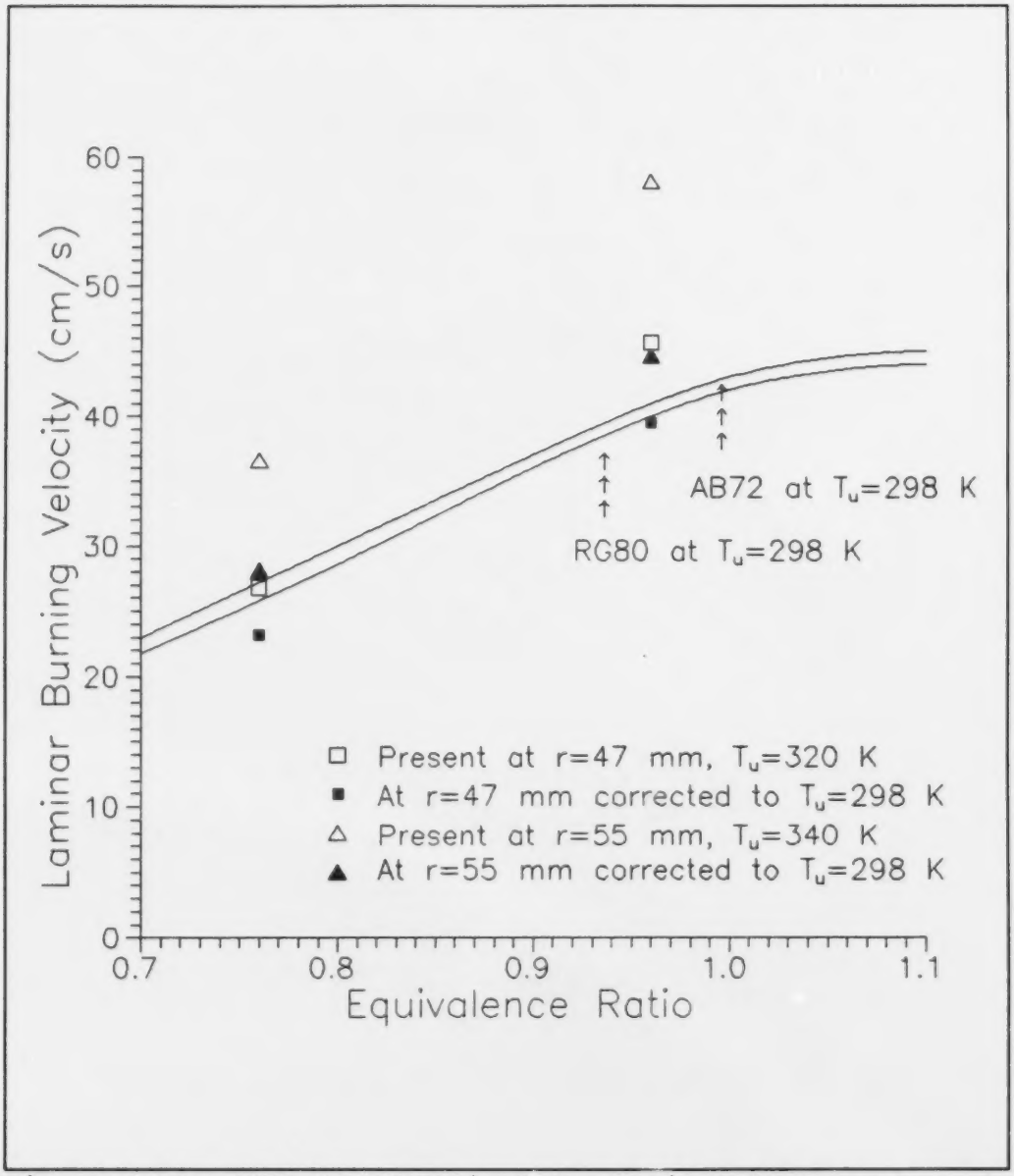

Figure 4.13 : Effects Of Equivalence Ratio And Temperature On Burning Velocities Of Methane-Air Flames.

55 mm radius flames is attributed to a higher unburnt gas temperature of 340 K.

The temperature exponent of Equation 4.1 was found to be about 2 for methane-air flames at atmospheric conditions [RG80]. In Figure 4.13, the points labelled "At r = 47 mm corrected to T_u = 298 K" are the burning velocities of 47 mm radius flames after correcting for the temperature effect. The temperature correction was done using a temperature exponent of 2. These corrected burning velocities at T_u = 298 K are slightly lower than those of [RG80] and [AB72].

The temperature exponent of 2 was also used for correcting the laminar burning velocities at r = 55 mm to T_u = 298 K. These corrected burning velocities are shown by points labelled "At r = 55 mm corrected to T_u = 298 K". These corrected burning velocities are about 10% higher than those of [RG80] and [AB72]. The different flame sizes involved in this study could have some effects on the corresponding burning velocities. Further experiments with varying initial temperatures are required to study the temperature effect on burning velocity.

In summary, the pressure exponents obtained in this study were found to be more negative than those in the literature. The laminar burning velocities varied within 10% agreement with those obtained by others. These discrepancies could lead to some suspicion about the burning velocities. However, turbulent burning velocities are expressed in the normalized form, S_t/S_u, so this would cancel out any unusual pressure and temperature effects.

4.3 Laminar Flame Growth From High Speed Video

Figure 4.14 shows the flame growth trace of a 76% stoichiometric, methane-air flame ignited at 1 atm and 23°C. The solid trace is the flame growth obtained from the pressure trace. The squares show the flame growth obtained from the high speed video images of the same run.

This particular run is typical for all laminar runs with initial pressure of 1 atm. Figure 4.14 shows that the pressure trace shows reasonable signal as early as $r/R_{bomb} = 0.25$ ($r = 19$ mm). For sub-atmospheric pressure tests, larger noise was encountered. The initial high noise pressure trace lasted longer in these low pressure tests.

Comparing the flame growth based on pressure trace with that obtained from the video images, shown in Figure 4.14, the flame growth from the pressure trace is slower than that obtained from the high speed video. The difference is about 4 ms when the flame radius is 30 mm ($r/R_{bomb} = 0.4$).

The difference of about 13% or 4 mm in flame radius for a 30 mm radius flame, shown in Figure 4.14, could be due to various factors. There is a high possibility that the burnt mixture may not consist of completely burnt mixture during the process. Chemical equilibrium is usually not achieved during combustion [RG80]; for a 95% burnt mixture the "actual" flame radius would be about 2% smaller than a completely burnt mixture. The pressure trace method uses the mass fraction burnt to calculate the mean flame radius, while the image processing method detects the very small tempera-

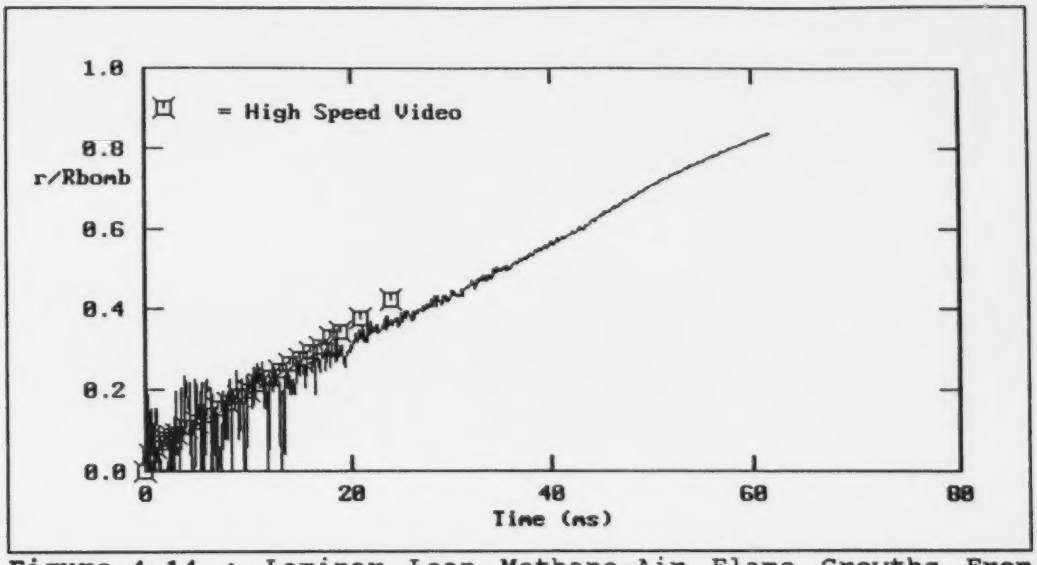

Figure 4.14 : Laminar Lean Methane-Air Flame Growths From Schlieren Video Images And Pressure Trace Analyses.
($\emptyset$ = 0.76, P_i = 1 atm, T_i = 296 K)

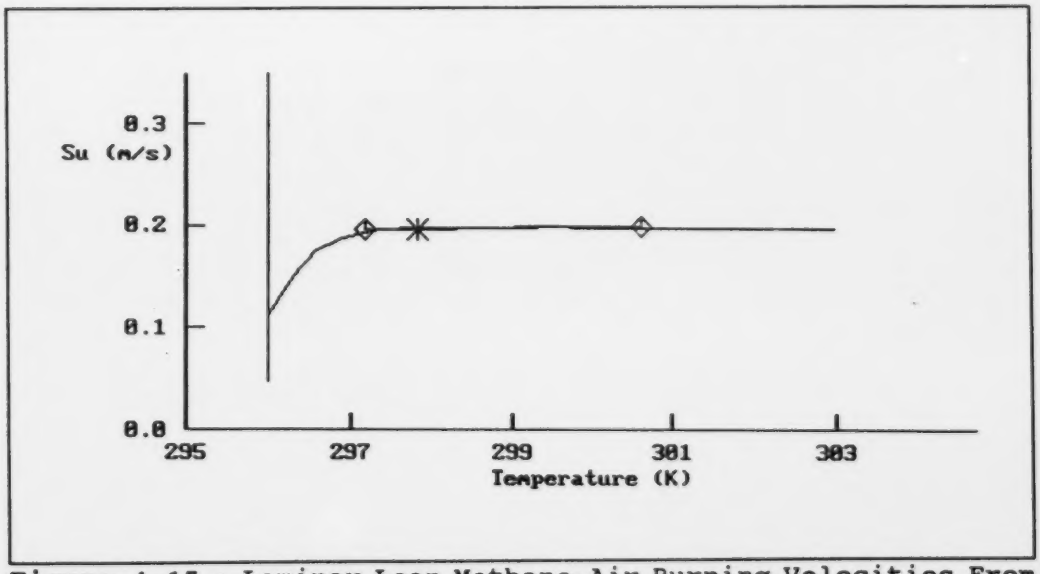

Figure 4.15 : Laminar Lean Methane-Air Burning Velocities From The Schlieren Video Images.
($\emptyset$ = 0.76, P_i = 1 atm, T_i = 296 K, $\diamond$ = range of r (19 mm to 27 mm), * = S_u at r = 23 mm)

ture gradient in the unburnt mixture. The difference in flame radius obtained from these two methods is of the order of the flame thickness (≈ 0.1mm). The image processing program also has the tendency to include a slightly larger area than the actual cross sectional area of the flame.

There are two other factors which could had contributed to the discrepancy of the flame growth mentioned above. First, the assumption of perfectly spherical flame calculated from the cross sectional area could be one contributor. This is because the indented volume due to the two intruding electrodes could have reduced the actual volume. Secondly, there is a possibility of time lag for information to be transmitted from the flame front to the pressure transducer on the wall. These two factors were estimated to be relatively negligible for the flame sizes considered.

Figure 4.15 shows the plot of burning velocity as a function of unburnt gas temperature from the video images. The best fit line from flame radius of 19 mm to 27 mm ($0.25 < r/R_{bomb} < 0.35$) is used to obtained the burning velocity of 23 mm radius flame (T_u = 298 K, r/R_{bomb} = 0.30, P = 104 kPa). This burning velocity was found to be 19.8 cm/s. Figure 4.15 shows that the burning velocity remains relatively constant over the range considered.

Figure 4.16 shows the comparison between the burning velocities obtained by the two different methods. The conditions for each data point are tabulated in Table 4.7. It appears that the burning velocity from the pressure trace increases rapidly with flame size. However, this trend is likely created by large error for small

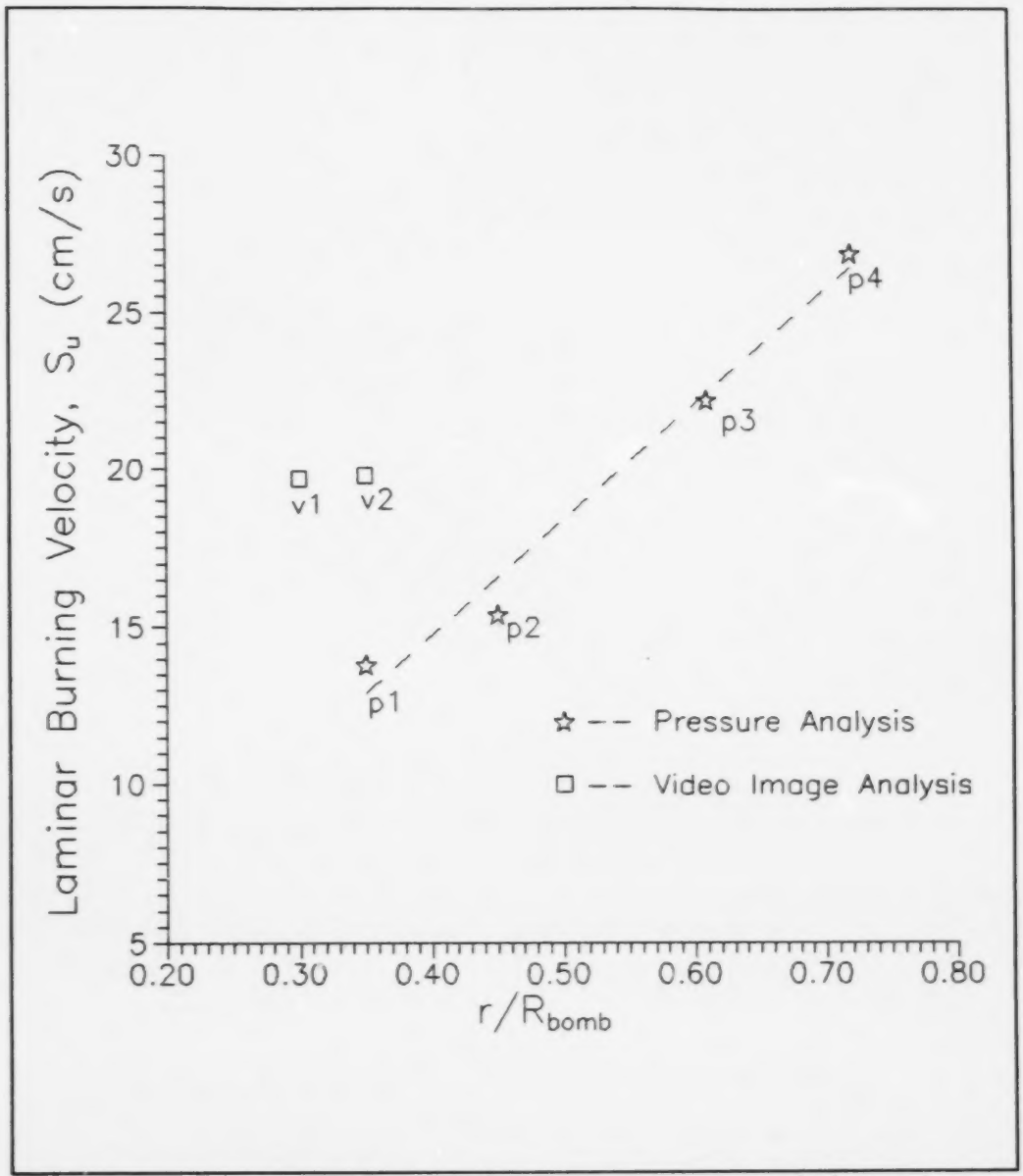

Figure 4.16 : Comparing Laminar Burning Velocities Of Lean Methane-Air Flames.
(Pressure Analysis Versus Video Image Analysis, P_i = 101 kPa, 101 kPa < P < 175 kPa)

flame sizes (p1 and p2) where the noise to signal ratio is very high at about 20% as shown in Figure 4.14.

Figure 4.16 also shows that the burning velocity obtained from the video images is faster than that obtained from the pressure trace. Considering data points p1 and v2, the difference between the burning velocities for this 23 mm radius flame was found to be 30%. This large difference is due to the square of the 13% difference in flame radius. Note that the video image obtained this flame size 4.2 ms earlier than the pressure trace.

Table 4.7 : Comparing Pressure And Video Image Analyses.

Data point	S_u (cm/s)	r/R_{bomb}	r/R_{bomb} range	T_u (K)	P (kPa)	Time (ms)
p1	13.8	0.35	0.30 to 0.40	300	107	23.2
p2	15.4	0.45	0.35 to 0.70	305	114	31.9
p3	22.2	0.61	0.55 to 0.75	320	135	43.8
p4	26.9	0.72	0.55 to 0.75	340	168	51.2
v1	19.7	0.30	0.25 to 0.35	298	104	16.0
v2	19.8	0.35	0.30 to 0.40	299	106	19.0

In short, the burning velocities obtained from the video images are higher than those calculated from the pressure traces. This difference is due to the squaring of the difference in flame

radius. The normalized turbulent burning velocities described as Equation 2.7 are used in Chapter 5. These normalized turbulent burning velocities from the two different analyses, produce acceptable turbulence relationships due to the fact that the discrepancy in burning velocities is relatively constant. As faster burning in the S_u measurements from video images also happen in the S_t measurements, the normalized turbulent burning velocity, S_t/S_u, discussed in Chapter 5 agree with those from the pressure-based measurements.

4.4 Summary On Laminar Burning Velocities

This study used propane-air and methane-air mixtures to examine the characteristics of laminar burning velocity. The burning velocities at atmospheric conditions were found to be reasonable but to increase as flames grow. The increase in burning velocity is mostly due to increasing unburnt gas temperature. As turbulent burning velocities are expressed in the normalized form, S_t/S_u, any excessive effects cancel out.

The burning velocities of propane-air flames have a large negative pressure exponent of about -0.6, compared with the more acceptable values of about -0.2. It was found that the pressure exponent obtained by other researchers varied significantly from one study to the other. Other studies such as [Gl87, Ku87, Ku60] showed that the pressure exponent is dependent on temperature, pressure, chemical reactions involved and burning velocity. The pressure exponents of methane-air flames obtained in this study

varied from -0.58 to -0.71 compared with a value of about -0.5 in the literature.

High speed Schlieren video was used as an independent analysis in conjunction with the pressure trace analysis in a 76% stoichiometric methane-air test. The 76% stoichiometric methane-air mixture was ignited at 1 atm and 23°C. The flame growth obtained from video images is faster than that obtained from pressure traces. For a 30 mm radius flame, there is a 13% difference in flame radius. This difference is larger than the expected laminar flame thickness of the order of 0.1 mm.

The burning velocity calculated from the video images is about 30% higher than that calculated from the pressure trace. This 30% difference came from squaring of the 13% difference in flame radius. Despite this discrepancy in absolute burning velocities obtained by the two analyses, the normalized turbulent burning velocities, S_t/S_u (to be presented in Chapter 5), should agree because the discrepancy is canceled out.

CHAPTER 5: TURBULENT FLAME RESULTS AND ANALYSIS

This chapter presents turbulent burning results of both lean propane-air and lean methane-air flames. The mixtures were ignited at 1 atm and 23°C. The turbulence intensity at ignition was varied from 0 m/s to 4.5 m/s for the propane-air case and 0 m/s to 6.7 m/s for the methane-air case. The integral scale was about 2 mm for the propane-air case and 8 mm for the methane-air case.

5.1 Turbulent Burning Velocity Of Lean Propane-Air

The turbulent burning characteristics of lean propane-air gas mixtures were studied. Propane-air mixtures of 75% and 95% stoichiometric compositions were ignited at 1 atm and 23°C. The ignition-time turbulence was varied from 0 to 4.5 m/s using the perforated plate with 5 mm diameter holes. The purpose was to study the effects of small scale turbulence ($\Lambda \approx 2$ mm) on burning velocities.

Summary results obtained from turbulent burning of 75% stoichiometric propane-air mixtures are tabulated in Table 5.1. The rapid distortion model from Chew and Britter [CB88a] was used in conjunction with normal turbulence decay to estimate the turbulence level. The actual integral scale during the combustion process was calculated using the normal decay model and corrected for density as discussed in Chapter 2.

As many parameters change with the burning process in a closed combustion chamber, a useful correlation would be one that relates the ignition-time turbulence with the overall burning rate.

Table 5.1 : Summary Data From 75% Stoichiometric Propane-Air Turbulent Flames.

At ignition, P = 101 kPa, T_u = 23 °C									
u' (m/s)	.54	.85	4.5	.20	.43	.58	.19	.37	.41
Λ (mm)	1.9	1.9	1.9	2.1	2.1	2.1	2.4	2.2	2.4
X/D	6.0	5.6	6.0	18	18	18	24	20	23
At r = 55 mm, T_u = 340 K, P = 170 kPa, r/R_{bomb} = 0.72									
u' (m/s)	.23	.27	.55	.18	.29	.43	.19	.37	.30
Λ (mm)	1.9	2.1	3.9	3.0	3.6	4.3	3.4	4.1	4.0
X/D	15	17	62	37	52	75	47	68	65
S_t (m/s)	.60	.62	.88	.50	.60	.76	.51	.72	.60
End of Explosion									
P_{max} (kPa)	737	712	728	740	722	720	737	721	725
T_{Pmax} (ms)	61	55	39	63	55	45	62	49	54

Figure 5.1 shows the plots of burning velocity and combustion duration as functions of ignition-time turbulence intensity. The dashed and solid lines fit data points with the same eddy scales. According to Equation 2.4, the Kolmogorov scale at ignition time was of the order of laminar flame thickness (≈ 0.1 mm).

In Figure 5.1, there is an increase of overall burning rate illustrated by a decrease in $Time_{Pmax}$ as the integral scale is increased. The burning velocity at 110 mm diameter flame also appears to increase with increasing ignition-time integral scale.

The normalized burning velocity curve with the smallest integral scale (Λ = 1.9 mm, X/D = 6) shown in Figure 5.1 is not linear. This nonlinearity is due to rapid turbulence decay after ignition. The rapid decay is most obvious in the inhomogeneous region with X/D less than 10 as shown in Figure 2.1. Therefore, expressing post-ignition burning velocity as a function of ignition-time turbulence intensity is deceptive.

Using the rapid distortion model of Chew and Britter [CB88a], the turbulence intensity for 110 mm diameter flames can be estimated. Figure 5.2 shows the effect of turbulence intensity on burning velocity of 110 mm diameter flames. The best linear fit line is

$$\frac{S_t}{S_u} = 1.00\ \frac{u'}{S_u} + 1.00\ ;\ \Lambda_{actual} \approx 2\ mm \qquad 5.1$$

Figure 5.2 shows that small changes in integral scale have negligible effect on the linear coefficient. Due to different

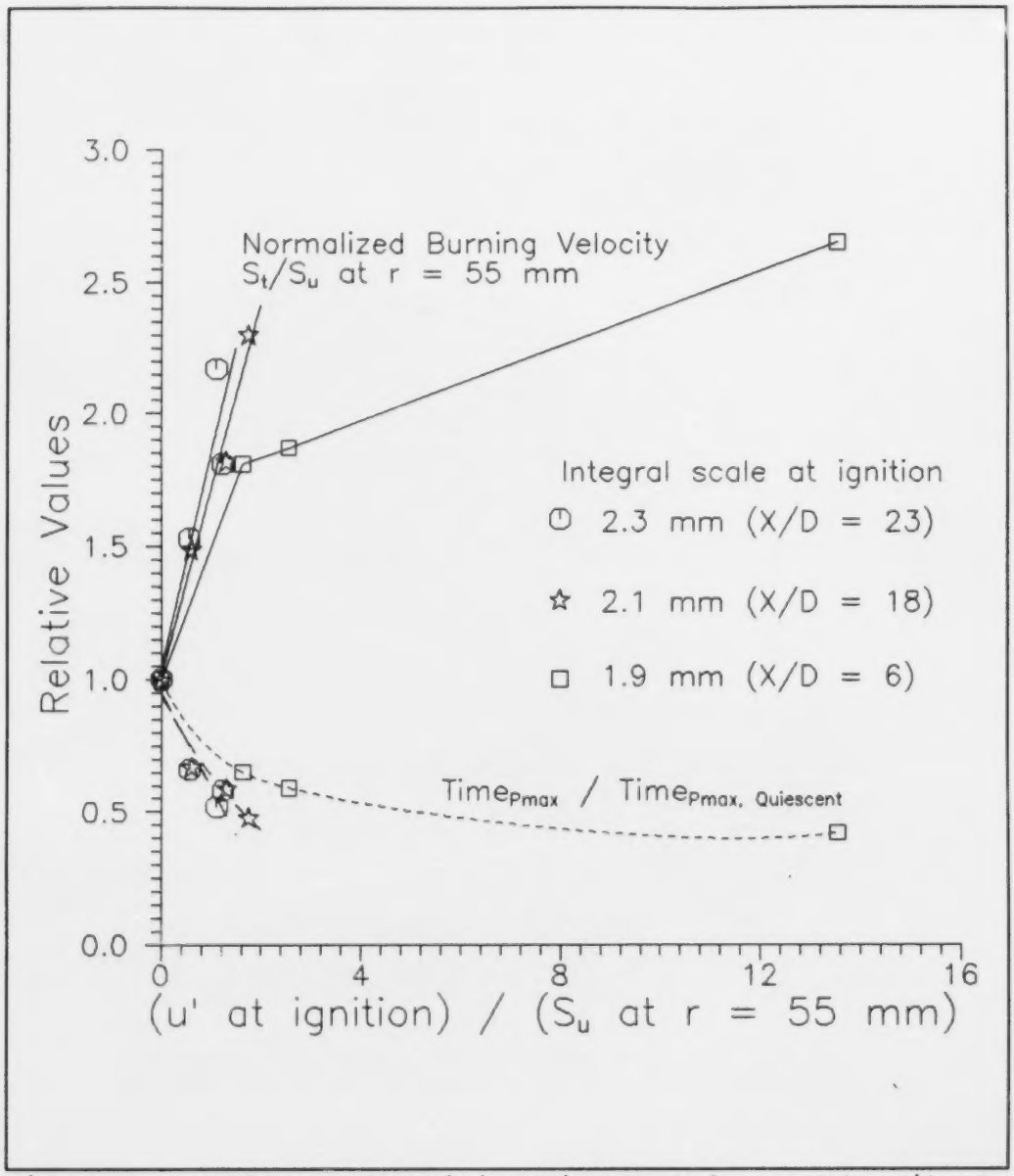

Figure 5.1 : Effect Of Ignition-Time Turbulence Intensity On Burning Rate Of Lean Propane-Air Flames (Ø = 0.75).
(X/D = Normalized Distance Downstream Of The Perforated Plate As In Equation 2.1)

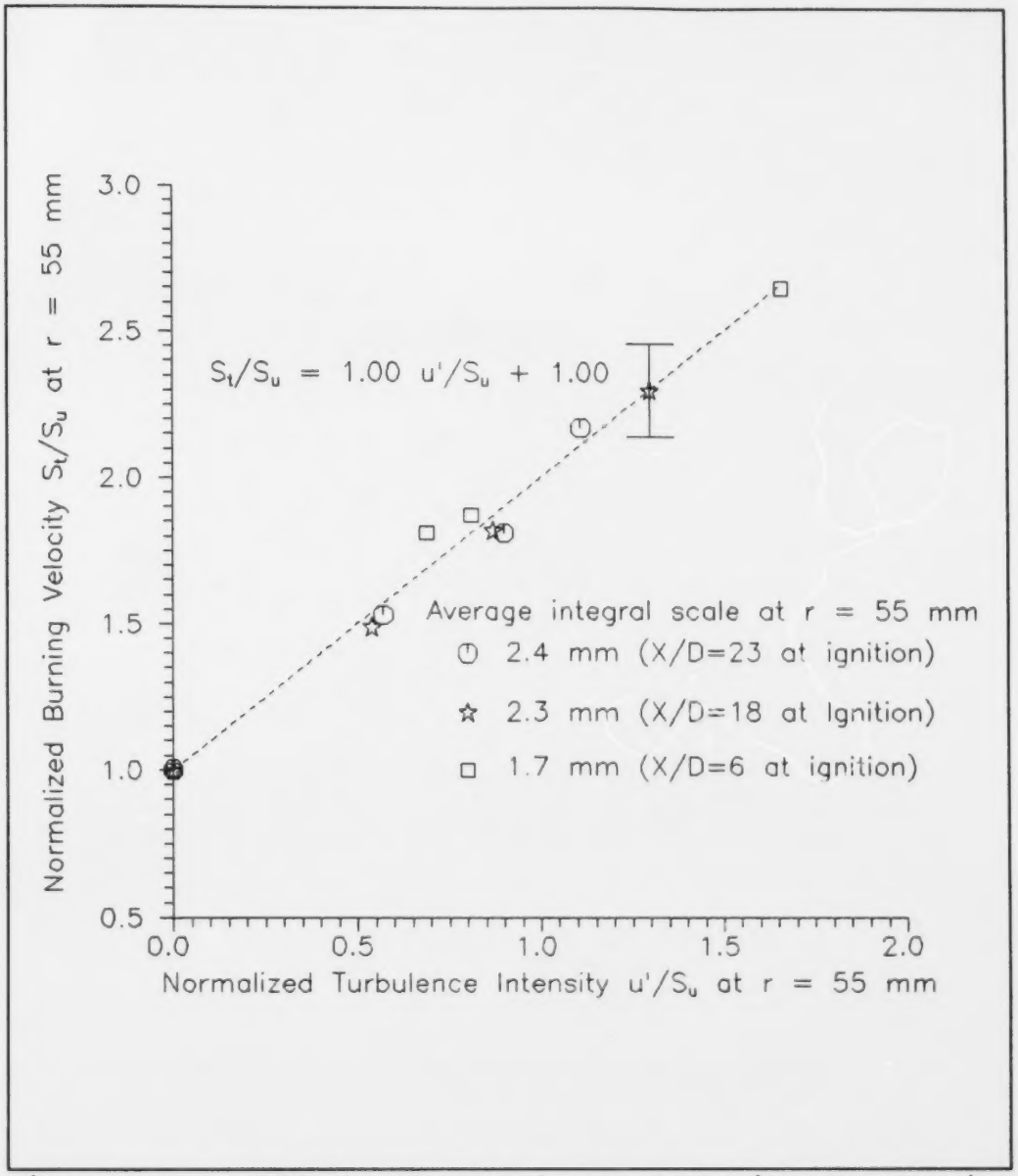

Figure 5.2 : Effect Of Turbulence Intensity On Burning Velocities Of Lean Propane-Air Flames (Ø = 0.75) At r = 55 mm. (T_u = 340 K, P = 170 kPa, X/D = Normalized Distance Downstream Of Plate, Error Bar = ±7%)

burning rates, the different symbols only designate data points of approximately equal integral scale for 110 mm diameter flames.

Results obtained from burning 95% stoichiometric propane-air mixtures are tabulated in Table 5.2. Propane-air mixture of 95% stoichiometry was used to study the effect of mixture composition on burning characteristics of near-stoichiometric propane-air flames. This richer mixture is expected to burn faster than the 75% stoichiometric propane-air mixture, giving a shorter combustion duration. As a result, there is less heat loss and a higher pressure rise. As expected, Table 5.2 shows higher pressure rises and shorter combustion durations compared with Table 5.1.

Figure 5.3 shows the effects of ignition-time turbulence intensity on burning velocity and total combustion period of the 95% stoichiometric propane-air flames. All curves are nonlinear and there are some overlapping. These nonlinear and overlapping lines are due to the over-prediction of turbulence intensity at 110 mm flame diameter by not accounting for the turbulence decay.

After correcting for turbulence decay and rapid distortion effects, Figure 5.4 shows the effect of turbulence intensity on burning velocity of 110 mm diameter flames. The straight line fits data points which correspond to the same ignition-time eddy scales or similar integral scale for 110 mm diameter flames. This linear line is described as

$$\frac{S_t}{S_u} = 1.02\ \frac{u'}{S_u} + 1.00\ ;\ \Lambda_{actual} \approx 2\ mm \qquad 5.2$$

The small differences in integral scale had negligible effect on

Table 5.2 : Summary Data From 95% Stoichiometric Propane-Air Turbulent Flames.

At ignition, P = 101 kPa, T_u = 23 °C									
u' (m/s)	.33	.66	.89	.35	.68	.91	.31	.56	.81
Λ (mm)	1.9	1.9	1.9	1.9	1.9	1.9	2.3	2.3	2.4
X/D	8.6	7.8	8.8	15	14	15	22	21	23
At r = 55 mm, T_u = 340 K, P = 172 kPa, r/R_{bomb} = 0.72									
u' (m/s)	.33	.47	.58	.31	.49	.62	.33	.50	.65
Λ (mm)	2.1	2.3	2.6	2.7	3.0	3.2	3.2	3.5	3.9
X/D	18	22	28	28	35	42	41	48	63
S_t (m/s)	.89	1.0	1.0	.79	.99	1.1	.82	1.0	1.1
At r = 55 mm, T_u = 340 K, P = 172 kPa, r/R_{bomb} = 0.72 (Including distortion in the normal direction only)									
u' (m/s)	.40	.58	.70	.38	.59	.75	.33	.61	.79
End of Explosion									
P_{max} (kPa)	839	864	853	856	871	855	871	862	858
T_{Pmax} (ms)	34	29	27	36	29	26	35	28	25

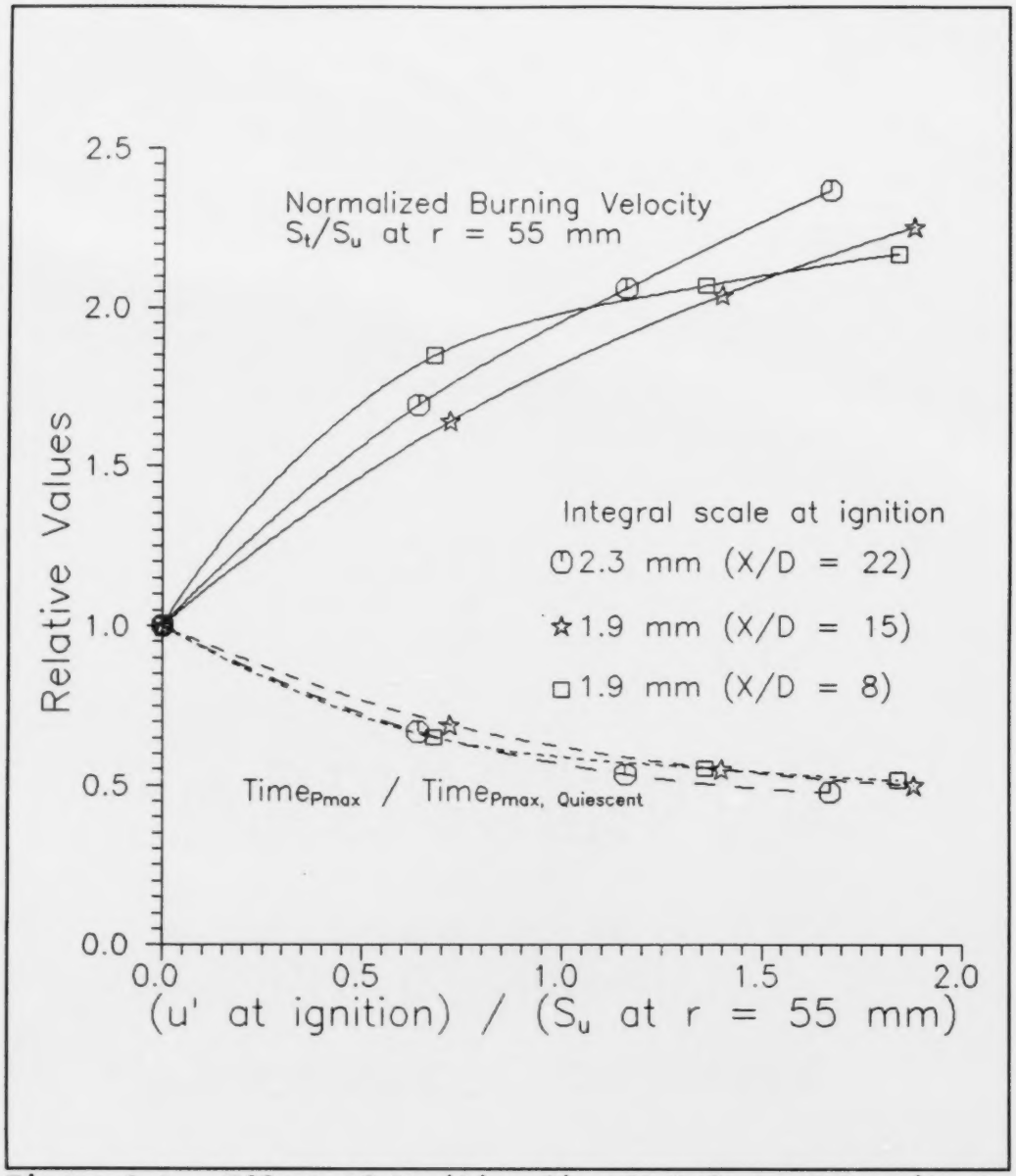

Figure 5.3 : Effect Of Ignition-Time Turbulence Intensity On Burning Rate Of Lean Propane-Air Flames (Ø = 0.95).
(X/D = Normalized Distance Downstream Of The Perforated Plate As In Equation 2.1)

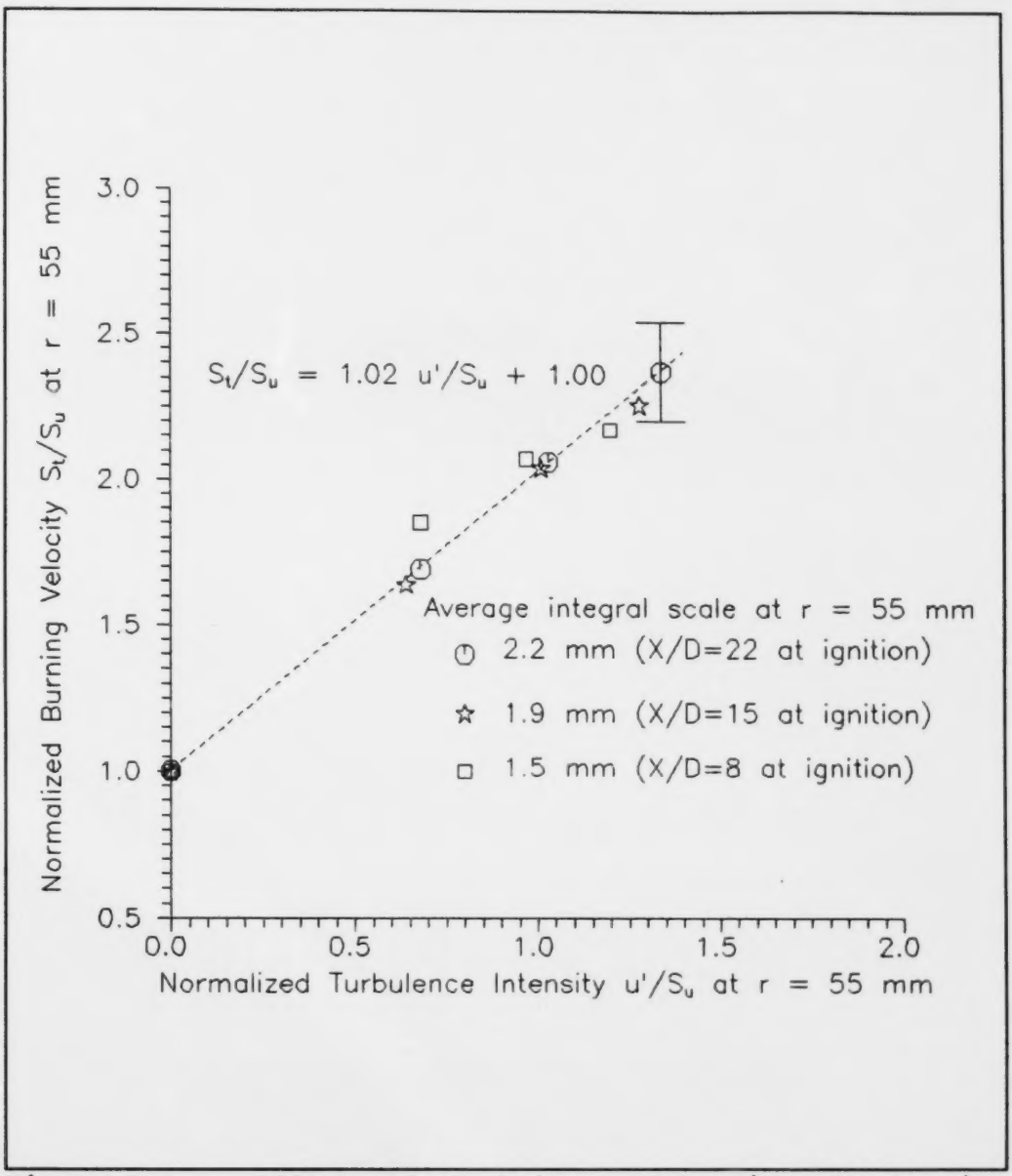

Figure 5.4 : Effect Of Turbulence Intensity On Burning Velocities Of Lean Propane-Air Flames (Ø = 0.95) At r = 55 mm. (T_u = 340 K, P = 172 kPa, X/D = Normalized Distance Downstream Of Plate, Error Bar = ±7%)

the relationship between burning velocity and turbulence intensity.

The effect of turbulence intensity due to rapid distortion in the transverse directions is expected to be much smaller than that in the normal direction. This effect as discussed in Section 2.4.2, could possibly be neglected in the rapid distortion model.

Figure 5.5 shows the plot of burning velocity as a function of corrected turbulence intensity for 110 mm diameter flames, considering only the normal-direction turbulence intensity. As expected, the slope is lower than that of Figure 5.4 due to higher turbulence intensity. The following equation describes the best linear fit line.

$$\frac{S_t}{S_u} = 0.85 \frac{u'}{S_u} + 1.00 \; ; \; \Lambda_{actual} = 2.0 \; mm \qquad 5.3$$

There is more scatter of data points in Figure 5.5 compared with Figure 5.4. This trend to more scatter, if true, may lead to the conclusion that the rapid distortion contribution in the transverse directions is important and must be included.

The relationship between burning velocity and turbulence intensity seems stronger for 95% stoichiometric propane-air flames compared with 75% stoichiometric propane-air flames (C_L = 1.02 versus 1.00). However, the maximum deviation from linearity shown in Figures 5.2 and 5.4 is about 9%. Therefore, the 2% effect of mixture composition on linear coefficient can be neglected over the range of mixture compositions considered.

The integral scales were about 2 mm for all runs and the

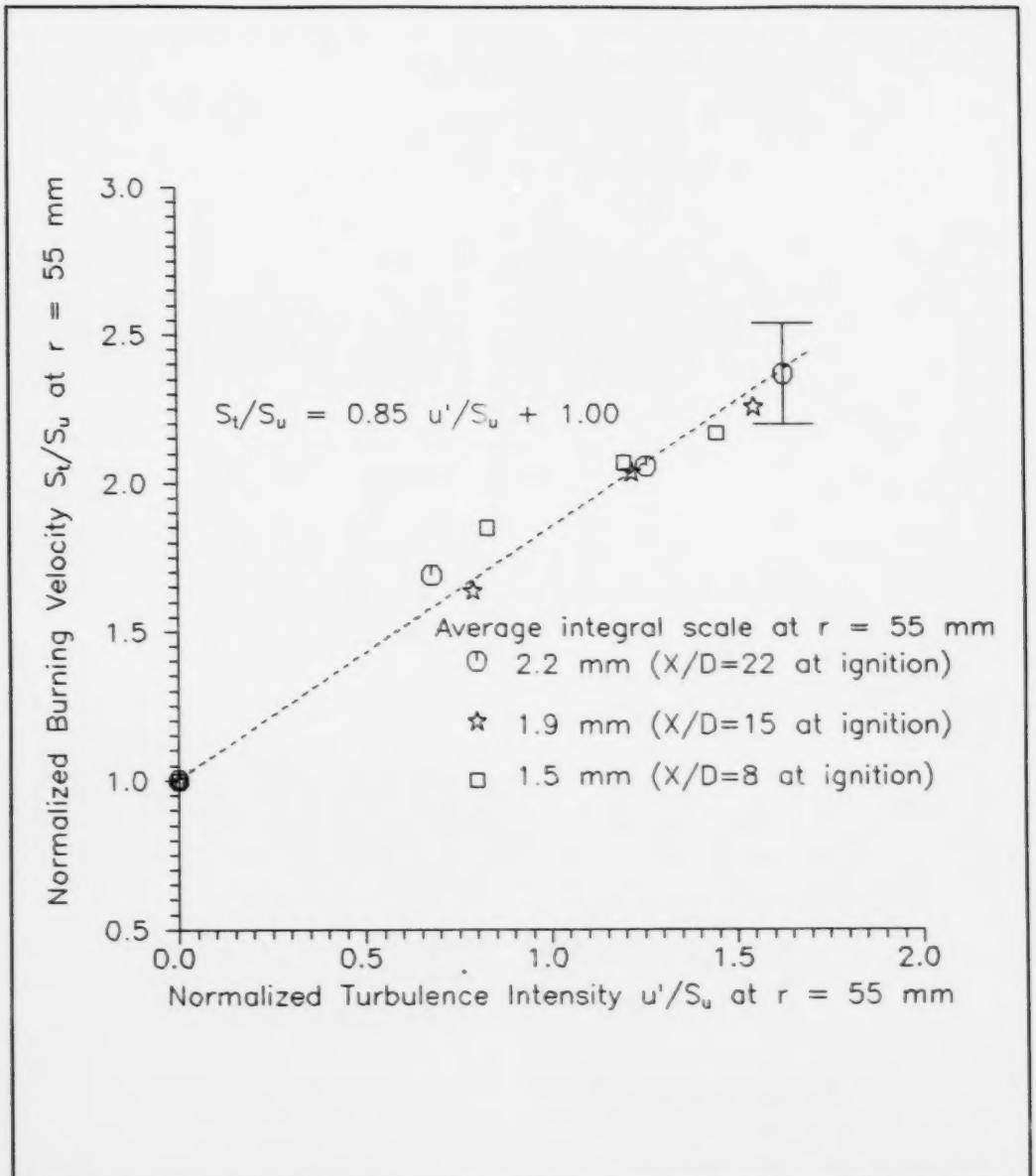

Figure 5.5 : Effect Of Turbulence Intensity (Normal Direction) On Burning Velocities Of Lean Propane-Air Flames (Ø = 0.95) At r = 55 mm.
(T_u = 340 K, P = 172 kPa, X/D = Distance Downstream Of Plate, Error Bar = ±7%)

effect of mixture composition was small. Therefore, the available data points can be combined into one graph of burning velocity as a function of turbulence intensity as shown in Figure 5.6. The corrected turbulence level takes into account of the effects of rapid distortion in all directions in conjunction with normal decay. The best linear fit gives

$$\frac{S_t}{S_u} = 1.01 \frac{u'}{S_u} + 1.00 \; ; \; \Lambda_{actual} \approx 2 \; mm \qquad 5.4$$

This equation illustrates that the linear coefficient between burning velocity and turbulence intensity is unity for the 110 mm diameter, lean propane-air flames.

5.2 Turbulent Burning Velocity Of Lean Methane-Air

Methane-air mixtures of 76% and 96% stoichiometric compositions were used to study the effect of turbulence on the burning characteristics of lean methane-air flames. All mixtures were ignited at 1 atm and 23°C. The significance of methane is its lower burning velocity compared with propane. The ignition-time turbulence intensity was varied from 0 to 6.7 m/s for 76% stoichiometric mixtures and 0 to 3.9 m/s for 96% stoichiometric mixtures. The perforated plate with 20 mm diameter holes was used to study the effect of medium scale turbulence on the burning velocity. The integral scale at ignition time was fixed at 7.6 mm.

Turbulent burning results from the 76% stoichiometric methane-air case are tabulated in Table 5.3. The maximum pressure rise is

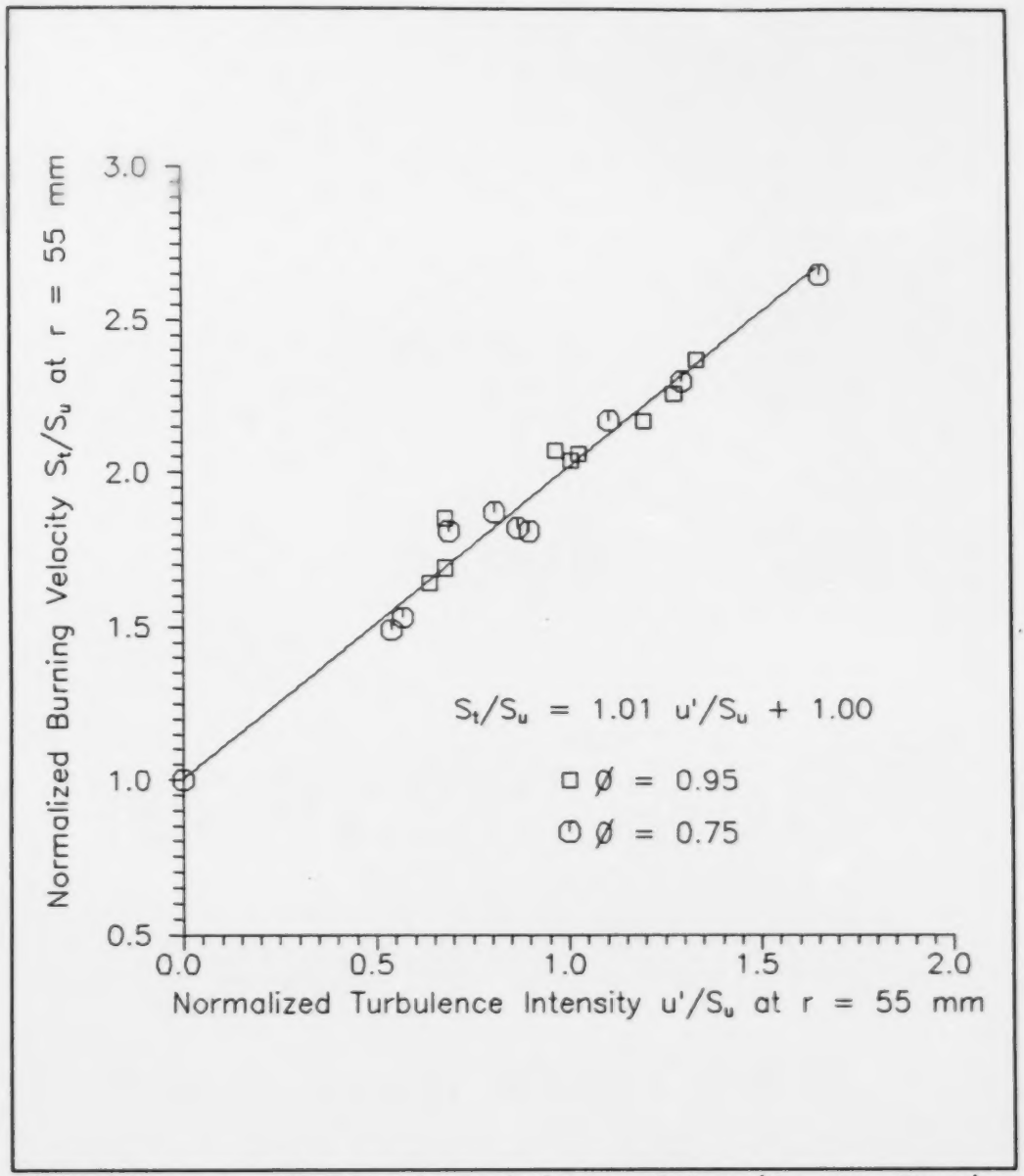

Figure 5.6 : Effect Of Turbulence Intensity On Burning Velocities Of Lean Propane-Air Flames At r = 55 mm. (T_u = 340 K, P = 171 kPa, Ø = 75 and Ø = 95 data combined)

Table 5.3 : Summary Data From 76% Stoichiometric Methane-Air Turbulent Flames.

At ignition, P = 101 kPa, T_u = 23 °C								
u' (m/s)	2.7	6.6	6.7	.42	.80	1.2	1.5	1.8
Λ (mm)	7.6	7.6	7.6	7.6	7.6	7.6	7.6	7.6
X/D	6.3	6.6	6.7	12	14	13	13	12
At r = 55 mm, T_u = 340 K, P = 168 kPa, r/R_{bomb} = 0.72								
u' (m/s)	1.5	1.7	1.8	.44	.76	1.0	1.2	1.4
Λ (mm)	7.6	7.7	7.8	8.3	9.5	9.7	10	9.7
X/D	13	15	15	17	23	24	25	24
S_t (m/s)	1.2	1.4	1.4	.59	.86	1.0	1.1	1.2
At r = 55 mm, T_u = 340 K, P = 168 kPa, r/R_{bomb} = 0.72 (Including intensity in the normal direction only)								
u' (m/s)	1.8	2.1	2.2	.54	.76	1.3	1.5	1.7
End of Explosion								
P_{max} (kPa)	705	705	703	699	707	708	703	696
T_{Pmax} (ms)	33	29	27	59	43	36	33	31

slightly lower than that of 75% stoichiometric propane-air case.

Figure 5.7 shows the effect of ignition-time turbulence intensity on burning rates. The integral scales remained constant at about 8 mm. Ignition occurred at two different normalized distances downstream of the perforated plate as designated by the two symbols. According to Equation 2.4, the region at X/D = 6.5 approximately corresponds to Kolmogorov scale of 0.09 mm while that at X/D = 13 represents 0.15 mm Kolmogorov scale. Similar to the propane-air case, the relationship between the turbulent burning velocity at 110 mm diameter flame and the ignition-time turbulence intensity is non-linear and misleading.

Considering the average turbulence intensity in all directions, Figure 5.8 shows the effect of turbulence intensity on burning velocity for 110 mm diameter flames. The linear line that fits all data points is

$$\frac{S_t}{S_u} = 0.69 \frac{u'}{S_u} + 1.00 \; ; \; \Lambda_{actual} \approx 6 \; mm \qquad 5.5$$

The 10% change in integral scale has no significant effect on the normalized burning velocity and turbulence intensity relationship.

Figure 5.9 shows the effect of turbulence on burning velocity while only accounting for turbulence intensity in the normal direction. The result is described as

$$\frac{S_t}{S_u} = 0.56 \frac{u'}{S_u} + 1.00 \; ; \; \Lambda_{actual} \approx 6 \; mm \qquad 5.6$$

The normal turbulence intensity is higher without the reduction

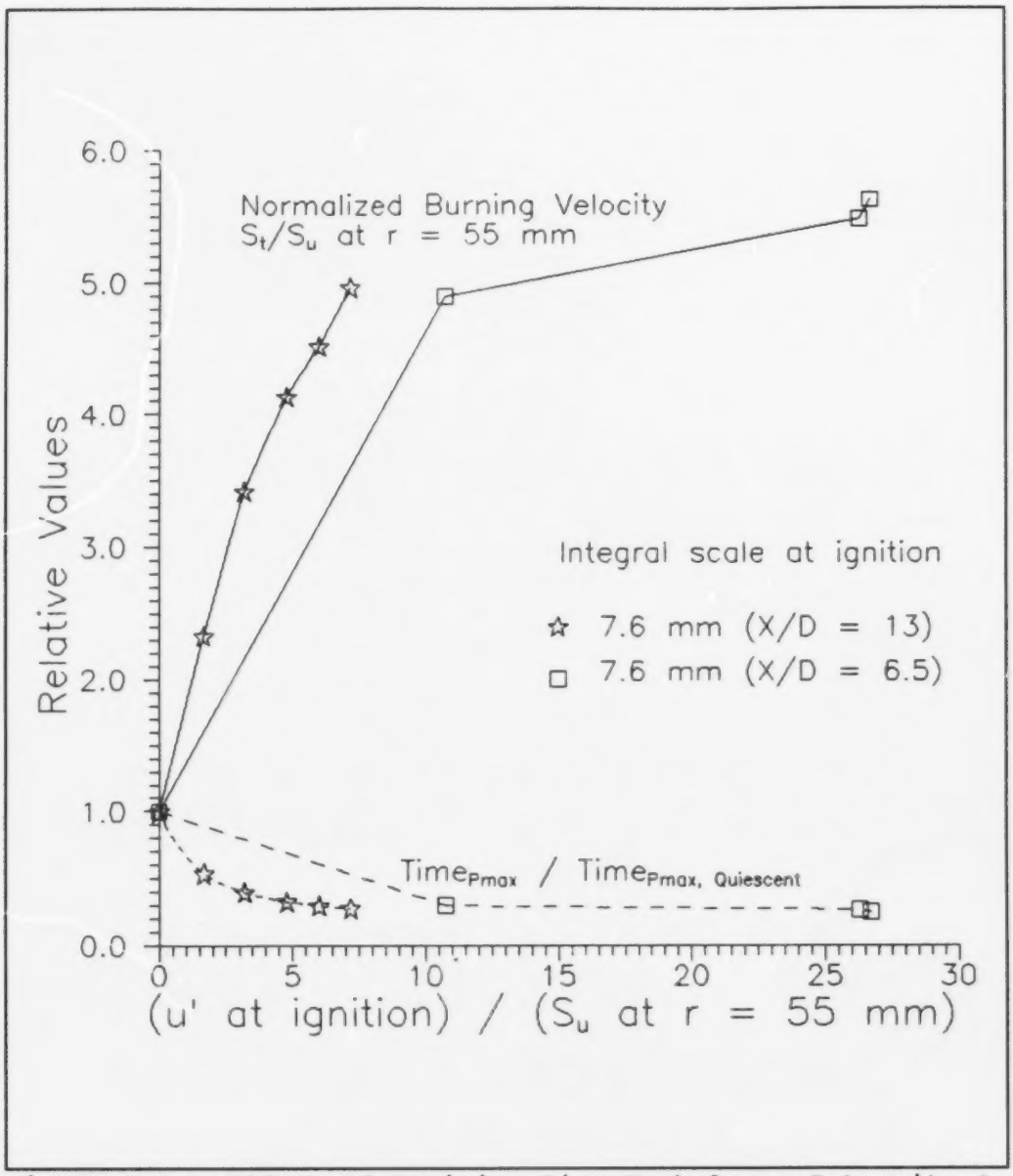

Figure 5.7 : Effect Of Ignition-Time Turbulence Intensity On Burning Rate Of Lean Methane-Air Flames (Ø = 0.76).
(X/D = Normalized Distance Downstream Of The Perforated Plate As In Equation 2.1)

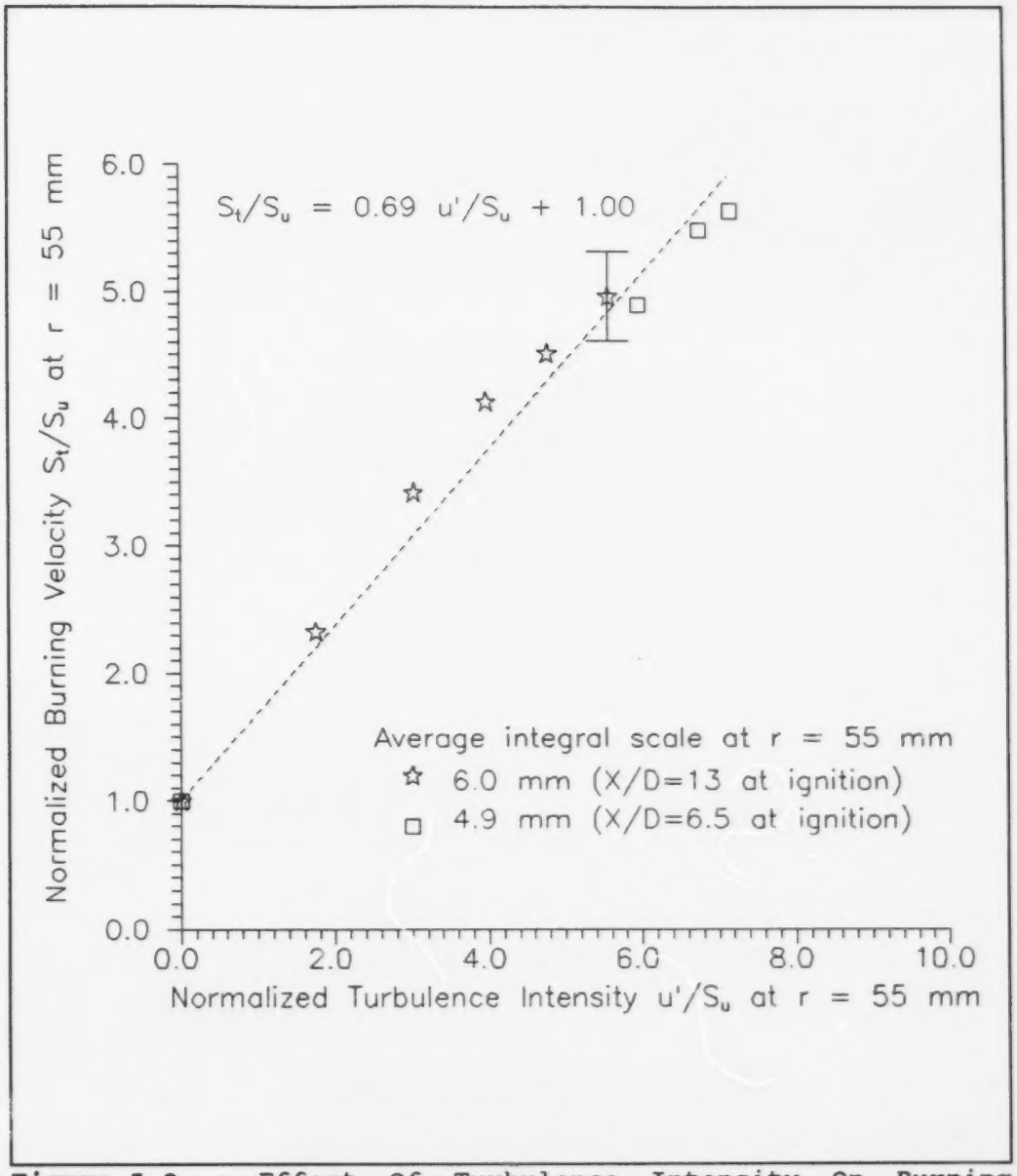

Figure 5.8 : Effect Of Turbulence Intensity On Burning Velocities Of Lean Methane-Air Flames (Ø = 0.76) At r = 55 mm. (T_u = 340 K, P = 168 kPa, X/D = Normalized Distance Downstream Of Plate, Error Bar = ±7%)

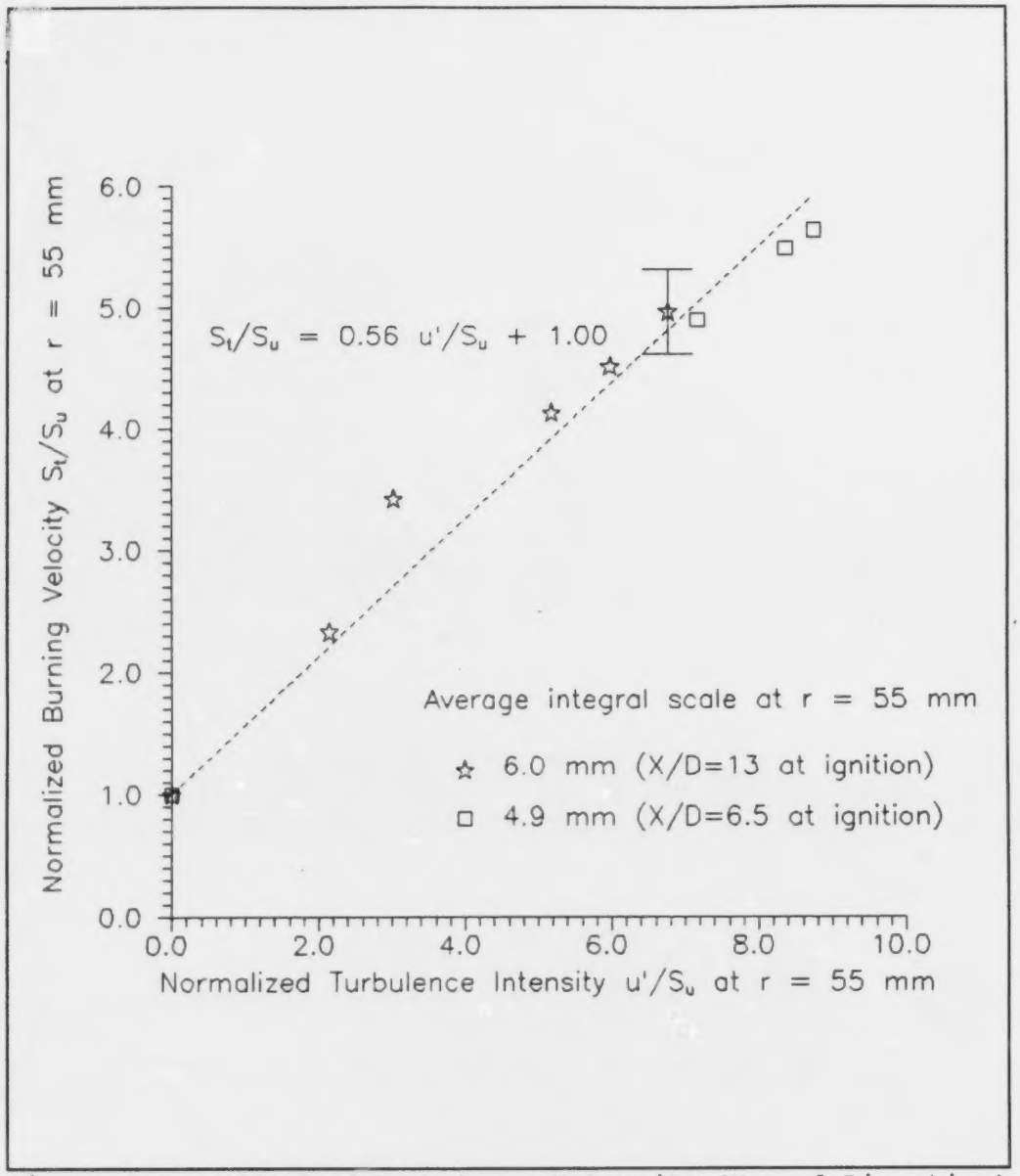

Figure 5.9 : Effect Of Turbulence Intensity (Normal Direction) On Burning Velocities Of Lean Methane-Air Flames (Ø = 0.76) At r = 55 mm.
(T_u = 340 K, P = 168 kPa, X/D = Distance Downstream Of Plate, Error Bar = ±7%)

effect in the transverse directions. As a result, the linear coefficient is smaller compared with that of Figure 5.8.

Turbulent burning results for 96% stoichiometric methane-air flame are tabulated in Tables 5.4a and 5.4b. As expected, the maximum pressure rise for this richer mixture is higher than the 76% stoichiometric methane-air flame. When comparing with 95% stoichiometric propane-air flame, this maximum pressure rise is smaller.

Figure 5.10 shows the effect of ignition-time turbulence on burning rates. Similar to the 76% stoichiometric methane-air flames, though the integral scales are relatively constant at ignition time, X/D varied from 7 to 13 at ignition. Consequently, the Kolmogorov scale increased from 0.09 mm to 0.15 mm. Once again, expressing turbulent burning velocities of 110 mm diameter flames as a function ignition-time turbulence is misleading.

Considering the effects of decay, rapid distortion and the average of intensity in all directions, Figure 5.11 shows the effect of turbulence intensity on burning velocity for 110 mm diameter flames. The best linear fit line is described as

$$\frac{S_t}{S_u} = 0.65\ \frac{u'}{S_u} + 1.00\ ;\ \Lambda_{actual} \approx 5\ mm \qquad 5.7$$

The effect of small changes in integral scale is negligible.

Figure 5.12 shows the turbulence intensity - burning velocity relationship based on turbulence intensity in the normal direction only. As expected, the turbulence intensity is higher without the negative averaging effect in the transverse directions. As a

Table 5.4a : Summary Data From 96% Stoichiometric Methane-Air Turbulent Flames.

At ignition, P = 101 kPa, T_u = 23 °C							
u' (m/s)	.52	1.0	3.1	3.9	2.0	2.2	3.0
Λ (mm)	7.6	7.6	7.6	7.6	7.6	7.6	7.6
X/D	7.0	6.9	7.4	6.5	8.7	9.2	9.7
At r = 55 mm, T_u = 340 K, P = 169 kPa, r/R_{bomb} = 0.72							
u' (m/s)	.59	.99	2.2	2.5	1.7	1.9	2.3
Λ (mm)	7.6	7.6	7.6	7.6	7.7	8.0	8.6
X/D	8.7	9.5	13	12	15	16	19
S_t (m/s)	.80	1.0	1.8	1.9	1.5	1.7	1.8
At r = 55 mm, T_u = 340 K, P = 169 kPa, r/R_{bomb} = 0.72 (Including intensity in the normal direction only)							
u' (m/s)	.72	1.2	2.7	3.0	2.0	2.3	2.8
End of Explosion							
P_{max} (kPa)	803	810	810	813	810	809	804
T_{Pmax} (ms)	39	30	18	18	22	20	18

Table 5.4b : Summary Data From 96% Stoichiometric Methane-Air Turbulent Flames.

At ignition, P = 101 kPa, T_u = 23 °C							
u' (m/s)	.36	.68	.96	1.4	1.4	1.6	1.9
Λ (mm)	7.6	7.6	7.6	7.6	7.6	7.6	7.6
X/D	11	13	15	12	13	13	12
At r = 55 mm, T_u = 340 K, P = 169 kPa, r/R_{bomb} = 0.72							
u' (m/s)	.47	.79	1.1	1.4	1.4	1.5	1.7
Λ (mm)	7.6	8.5	9.4	8.6	9.0	9.4	9.0
X/D	14	18	22	18	21	22	21
S_t (m/s)	.72	.98	1.2	1.4	1.5	1.5	1.5
At r = 55 mm, T_u = 340 K, P = 169 kPa, r/R_{bomb} = 0.72 (Including intensity in the normal direction only)							
u' (m/s)	.57	.96	1.3	1.7	1.6	1.8	2.1
End of Explosion							
P_{max} (kPa)	802	807	804	807	817	818	806
T_{Pmax} (ms)	40	30	27	23	22	22	21

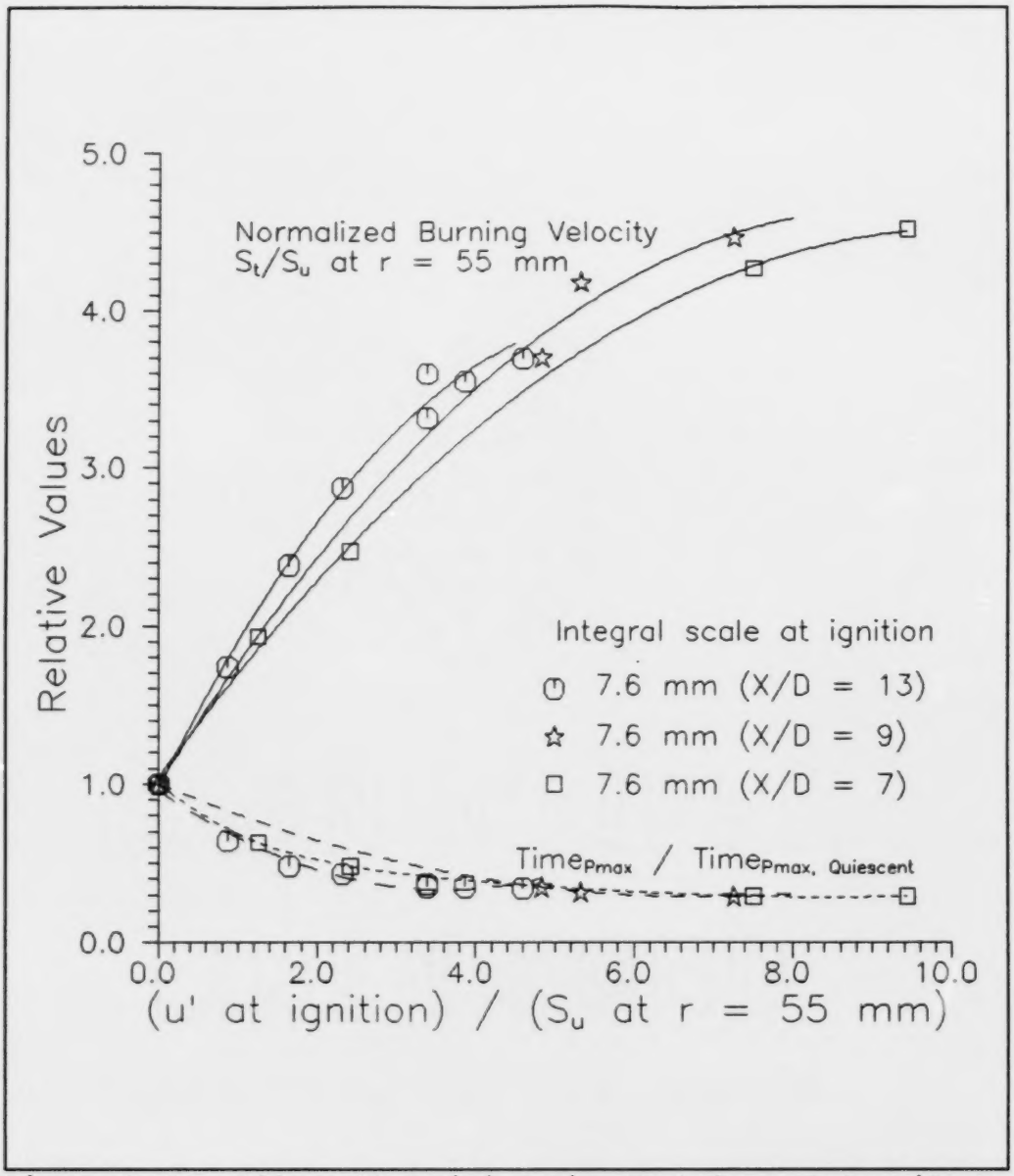

Figure 5.10 : Effect Of Ignition-Time Turbulence Intensity On Burning Rate Of Lean Methane-Air Flames (Ø = 0.96).
(X/D = Normalized Distance Downstream Of The Perforated Plate As In Equation 2.1)

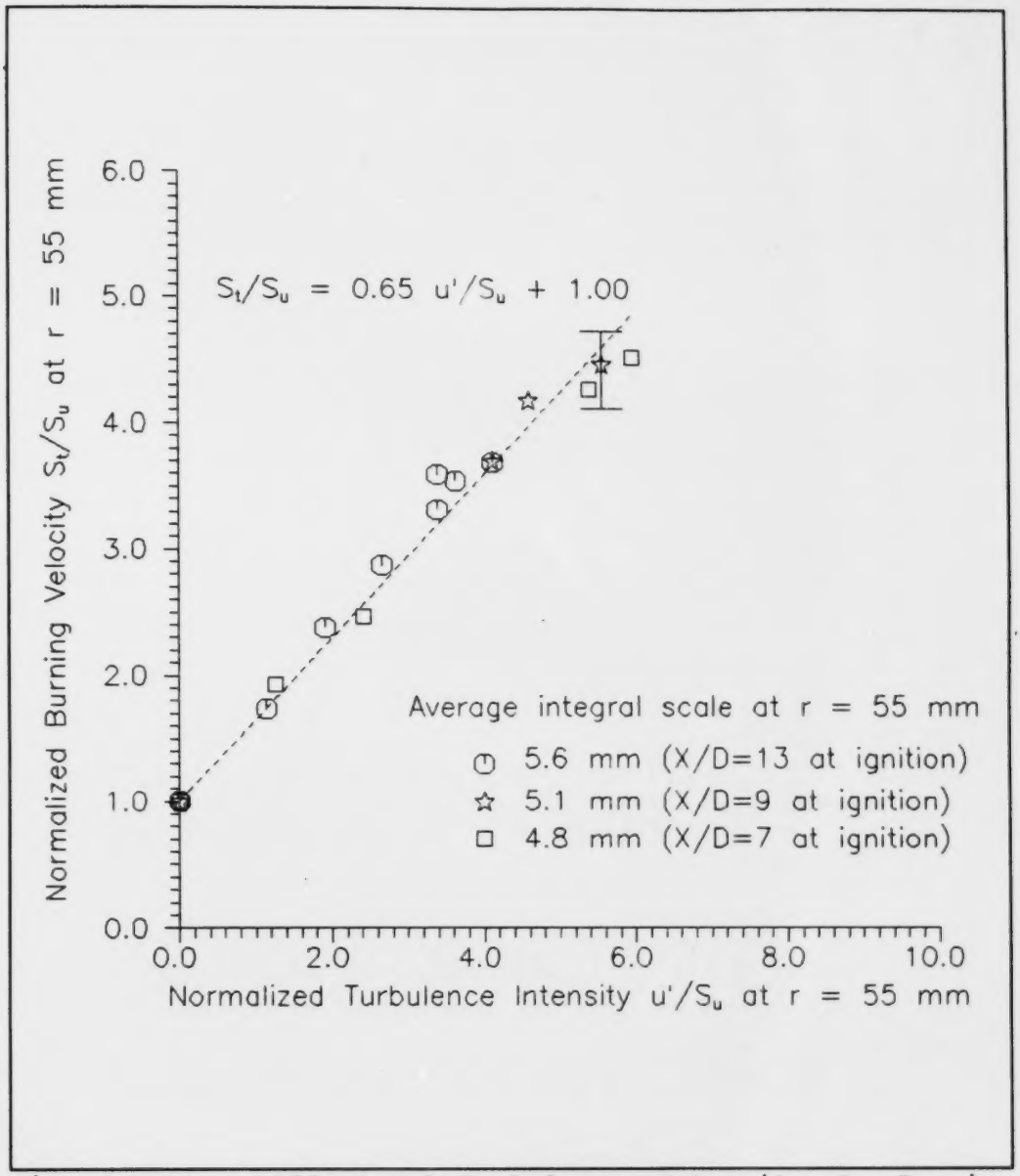

Figure 5.11 : Effect Of Turbulence Intensity On Burning Velocities Of Lean Methane-Air Flames (Ø = 0.96) At r = 55 mm. (T_u = 340 K, P = 169 kPa, X/D = Normalized Distance Downstream Of Plate, Error Bar = ±7%)

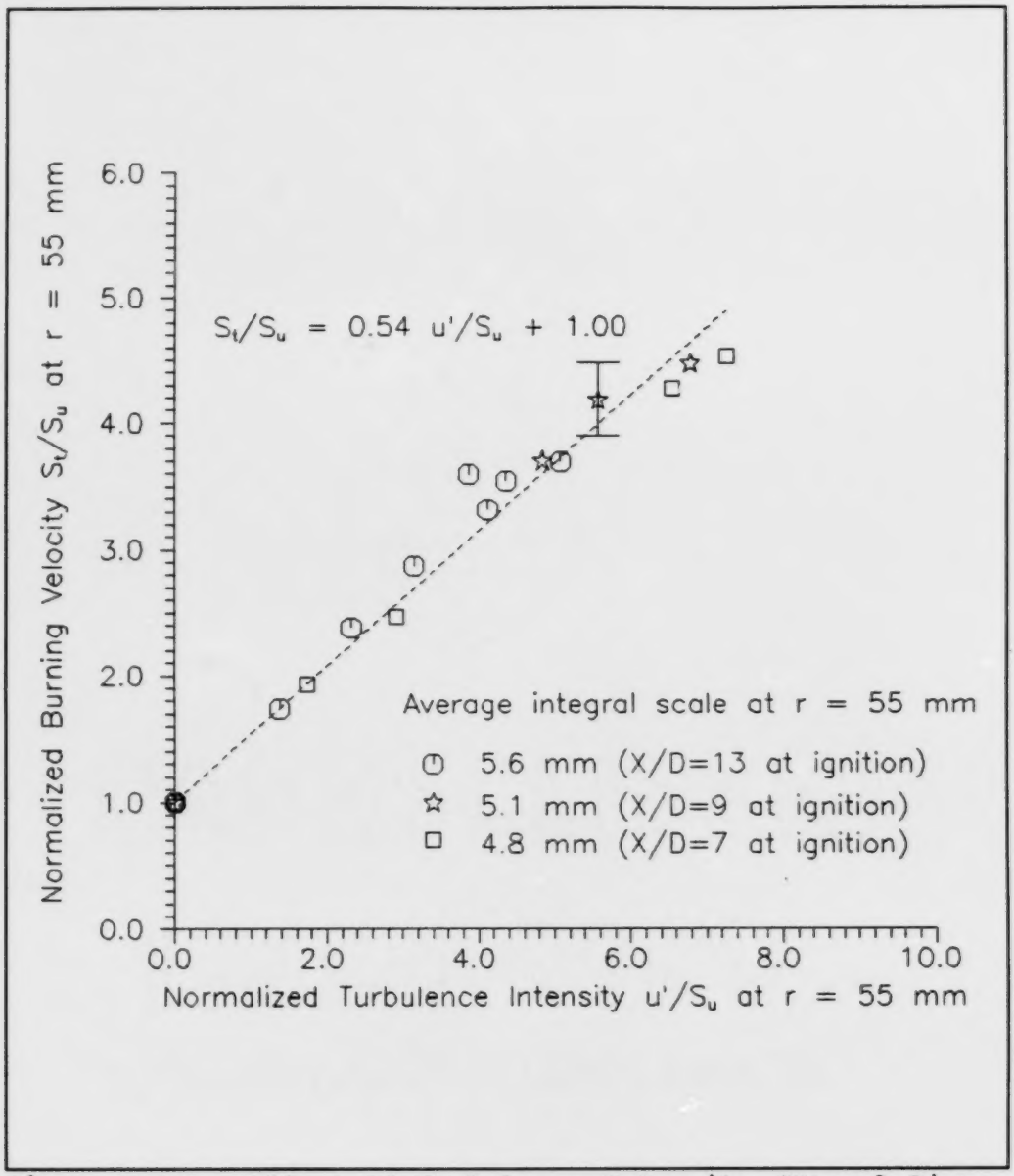

Figure 5.12 : Effect Of Turbulence Intensity (Normal Direction) On Burning Velocities Of Lean Methane-Air Flames (Ø = 0.96) At r = 55 mm.
(T_u = 340 K, P = 169 kPa, X/D = Distance Downstream Of Plate, Error Bar = ±7%)

result, the linear coefficient decreases. The result is described by the following equation.

$$\frac{S_t}{S_u} = 0.54\ \frac{u'}{S_u} + 1.00\ ;\ \Lambda_{actual} \approx 5\ mm \qquad 5.8$$

There is less scatter amongst data points in Figure 5.11 compared with Figure 5.12. This tends to imply that the rapid distortion in the transverse directions is important.

The relationship between burning velocity and turbulence intensity is relatively unaffected by mixture composition for the range of equivalence ratios considered (Ø = 0.76 to 0.96). With fixed integral scales of 7.6 mm at ignition for all runs, the available data points can be combined into one graph of burning velocity as a function of turbulence intensity for lean methane-air flames. This plot, shown in Figure 5.13, relates burning velocity with the actual turbulence intensity (average of components in all directions) for 110 mm diameter flames.

The best linear fit for all data points shown in Figure 5.13 gives

$$\frac{S_t}{S_u} = 0.67\ \frac{u'}{S_u} + 1.00\ ;\ \Lambda_{actual} \approx 6\ mm \qquad 5.9$$

This equation illustrates that the linear coefficient is 0.67 for lean methane-air flames. This linear coefficient is much smaller than that for lean propane-air flames.

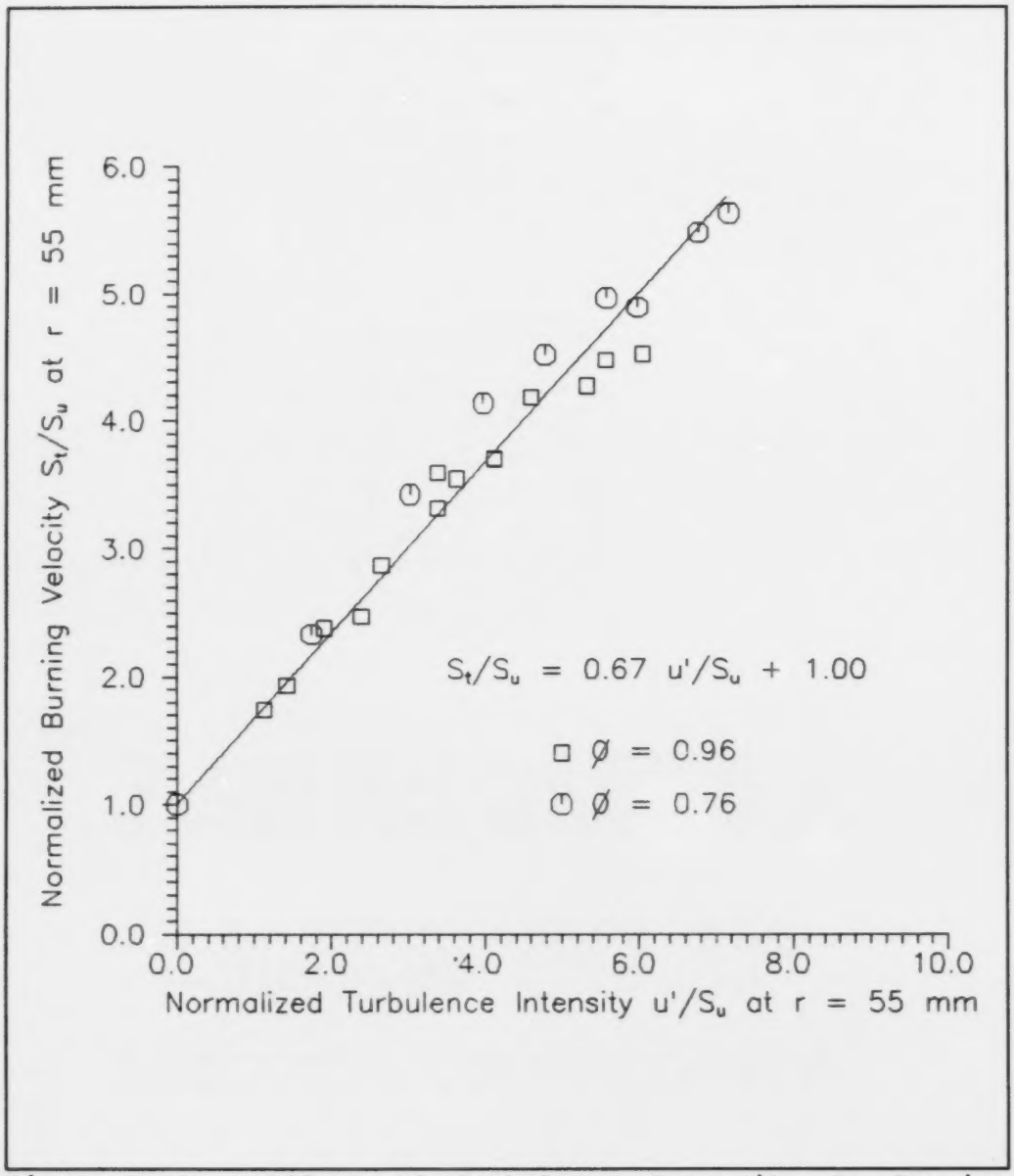

Figure 5.13 : Effect Of Turbulence Intensity On Burning Velocities Of Lean Methane-Air Flames At r = 55 mm. (T_u = 340 K, P = 169 kPa, Ø = 0.75 and Ø = 0.95 data combined)

5.3 Methane-Air Turbulent Flame Growth From High Speed Video

Using the high speed video camera running at 2000 frames per second, flame propagations in several 76% stoichiometric methane-air tests were taped in conjunction with the pressure traces. Image processing programs were then used to digitize the images and calculate the cross sectional area of the flame as discussed in Chapter 3. The measured flame cross-sectional area was converted to mean flame radius assuming a sphere. The flame growth rate was then used to calculate the burning velocity. The expansion factors from the multi-zone thermodynamic equilibrium model as discussed in Chapter 3 were used to convert the measured flame growth rate to burning velocity.

Flame sizes were measured from the time of ignition until the flame passed beyond the edge of the 110 mm diameter window. The window was not perfectly centred on the ignition point and turbulent flame growth was not uniform. As a result, the maximum flame size analyzed was approximately 60 mm diameter. Burning velocities were evaluated from the best of values from flames in the 38 mm to 53 mm diameter range ($0.25 < r/R_{bomb} < 0.35$, typically 4 to 7 images).

Samples of the video images obtained with laminar and turbulent flames are shown in Figure 5.14. These images have been "cut out" by the image processing software which searches for gradients in the Schlieren intensity image. This search takes place along rays from the center of the image, producing some roughness along the edges of the corrugated turbulent flames.

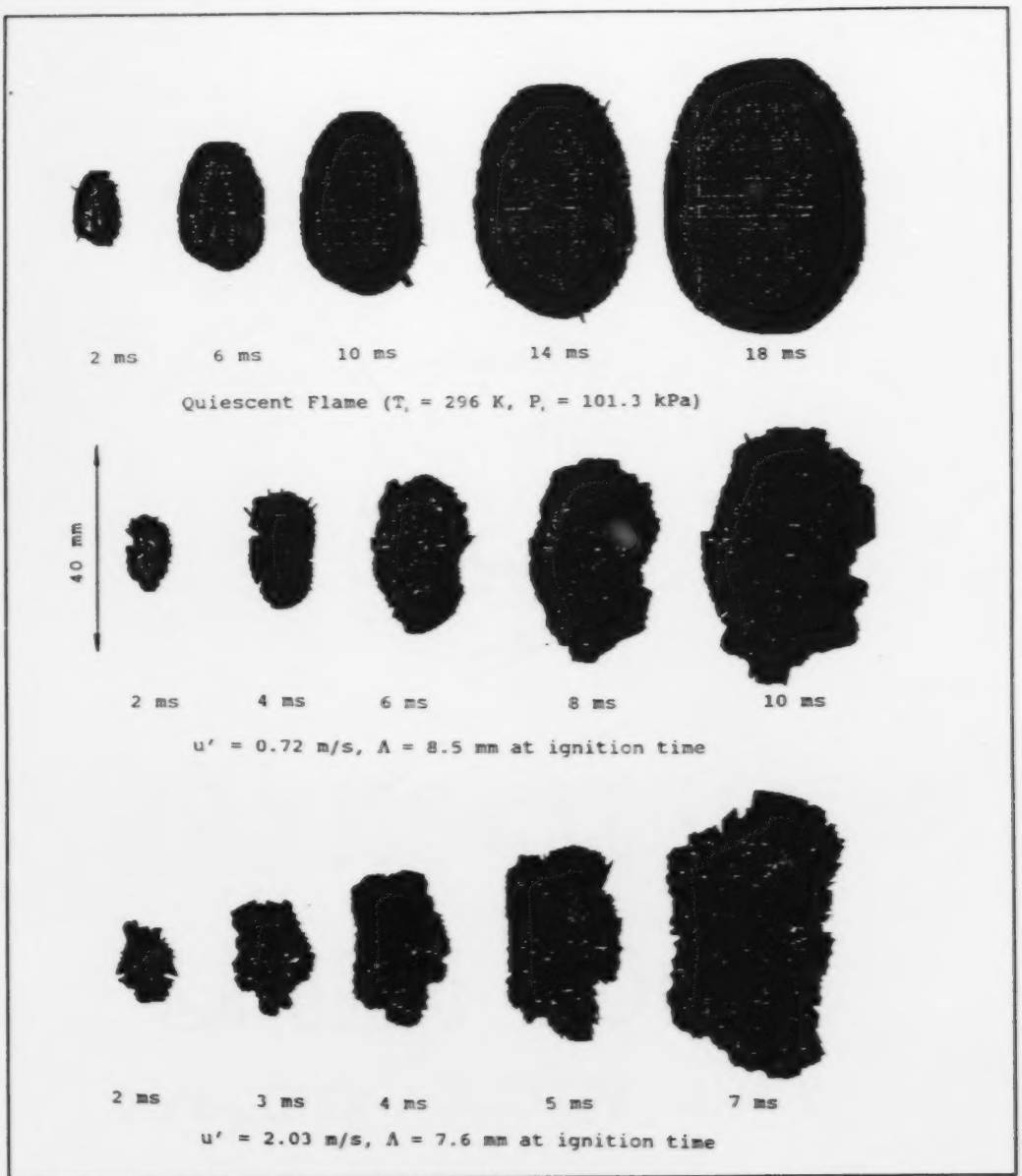

Figure 5.14 : Lean Methane-Air (Ø = 0.76) Turbulent Flames (compared with quiescent flame) From Video Images.

Figure 5.15 compares a typical low turbulence flame size ($u' = 0.4$ m/s, $\Lambda = 7.6$ mm, $X/D = 10$ at ignition time) obtained from the video images with that obtained from the pressure-based method. Similar to the case of laminar flame growth shown in Figure 4.14, pressure-based results are inherently noisy at the early stages of flame propagation. Consequently, the pressure-based results are only reliable for flames over 46 mm diameter ($r/R_{bomb} > 0.3$).

Figure 5.15 shows that the flame growth rate from the video images was about 13% higher than that measured by the pressure trace (about 3 mm in r at r = 25 mm). As previously mentioned, the Schlieren system would be expected to measure the leading edge of the flame front while the pressure trace gives the central flame front position. The difference as shown in Figure 5.15 is greater than this amount due to the same reasons discussed in Chapter 4. In short, under low turbulence conditions, the difference in flame growth between video-based method and pressure-based method is close to that of the laminar case. This validates the argument stated previously that though the burning velocities obtained by these two methods are different, the normalized burning velocities agree.

With high intensity turbulence, the difference between the flame growth obtained from the video images and the pressure trace is expected to increase. This larger difference in flame radius is due to the much thicker flame front present in high turbulence flames. Figure 5.16 illustrates a high turbulence flame growth recorded by both high speed video and pressure trace. The turbu-

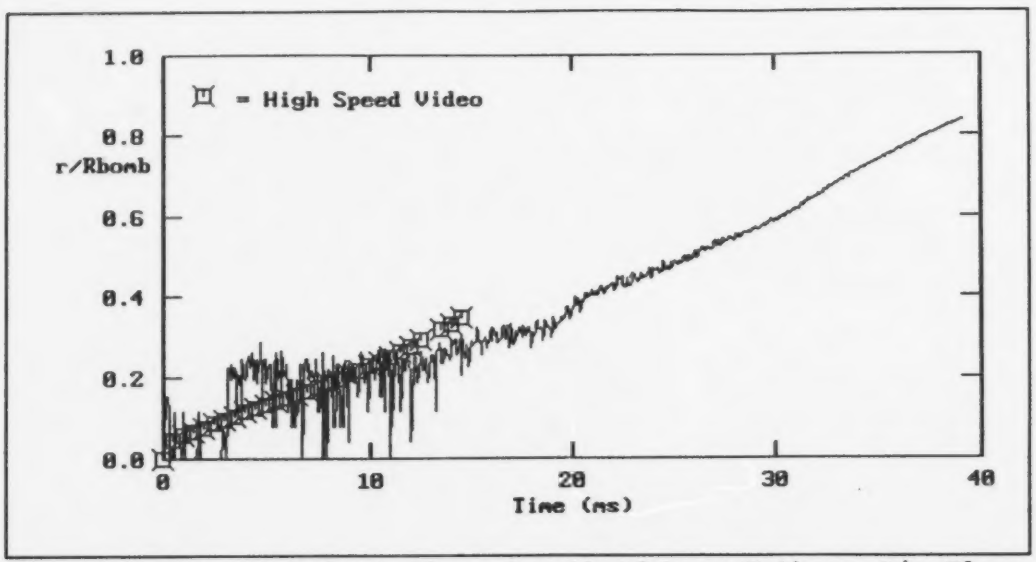

Figure 5.15 : Turbulent Flame Growth Of Lean Methane-Air Flame (Ø = 0.76, u' = 0.4 m/s, Λ = 7.6 mm, X/D = 10 at ignition).

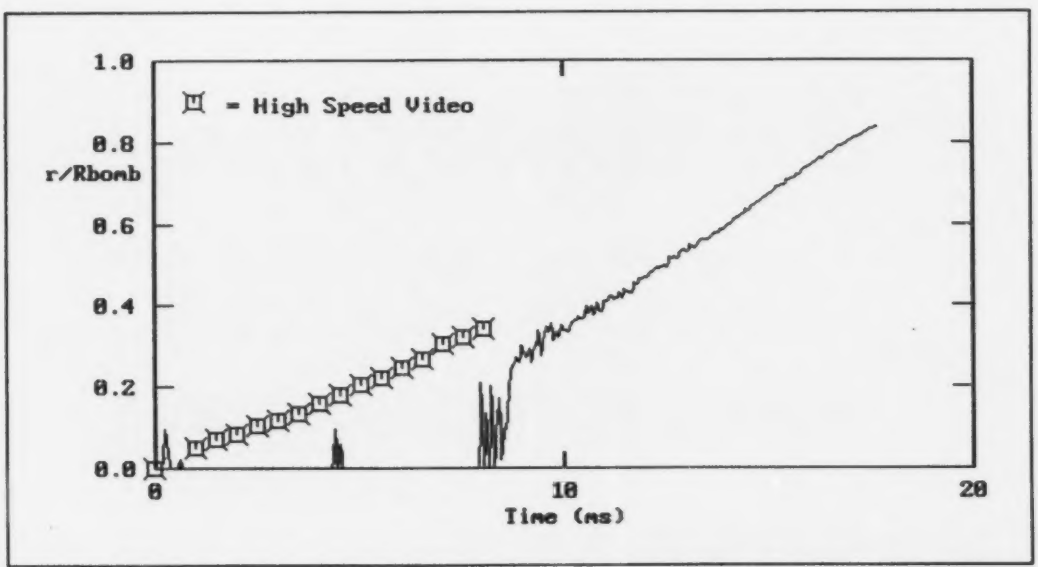

Figure 5.16 : Turbulent Flame Growth Of Lean Methane-Air Flame (Ø = 0.76, u' = 2 m/s, Λ = 7.6 mm, X/D = 9 at ignition).

lence intensity, u', at ignition time was 2 m/s (Λ = 7.6 mm, X/D = 9). The difference is large at about 5 mm at r = 25 mm due to the increasing flame thickness as progressively large eddies distort the flame front.

From Figures 5.15 and 5.16, the discrepancy between the flame growth obtained by the two methods becomes larger as the flame grows. This is due to the growing flame or reaction zone thickness as the flame propagates [AB87].

Table 5.5 tabulates the results for 46 mm diameter, methane-air flames obtained from the video images. The turbulence intensities were obtained by taking normal decay and rapid distortion effects into account. The effects due to rapid distortion at the 46 mm diameter flames were found to be small.

Figure 5.17 shows the plot of relative burning velocity measured from the flame images as a function of turbulence intensity. The best fit line is

$$\frac{S_t}{S_u} = 0.24 \frac{u'}{S_u} + 1.00 \qquad 5.10$$

The linear coefficient is much weaker at this early stage of flame propagation (46 mm diameter flames) than that found previously for 110 mm diameter flames.

There is a high scatter of the data points in Figure 5.17. One reason for this is that only single runs were used. Another reason is due to the poor time resolution of 0.5 ms interval between consecutive images.

Due to the window limitation on the cubical bomb and also the

Table 5.5 : Burning Velocity Of Lean Methane-Air Flame From Video Images at r = 23 mm (T_u = 298 K, P = 104 kPa).

u' (m/s)	u'/S_u	S_t (m/s)	Time (ms)	S_t/S_u
0	0	0.197	16.00	1
0.43	2.18	0.286	12.50	1.45
0.67	3.40	0.355	11.00	1.80
0.71	3.60	0.401	9.50	2.04
0.94	4.77	0.524	10.00	2.66
1.19	6.04	0.448	8.50	2.27
1.17	5.94	0.417	9.00	2.12
1.31	6.65	0.465	8.00	2.36
1.73	8.78	0.654	6.50	3.32

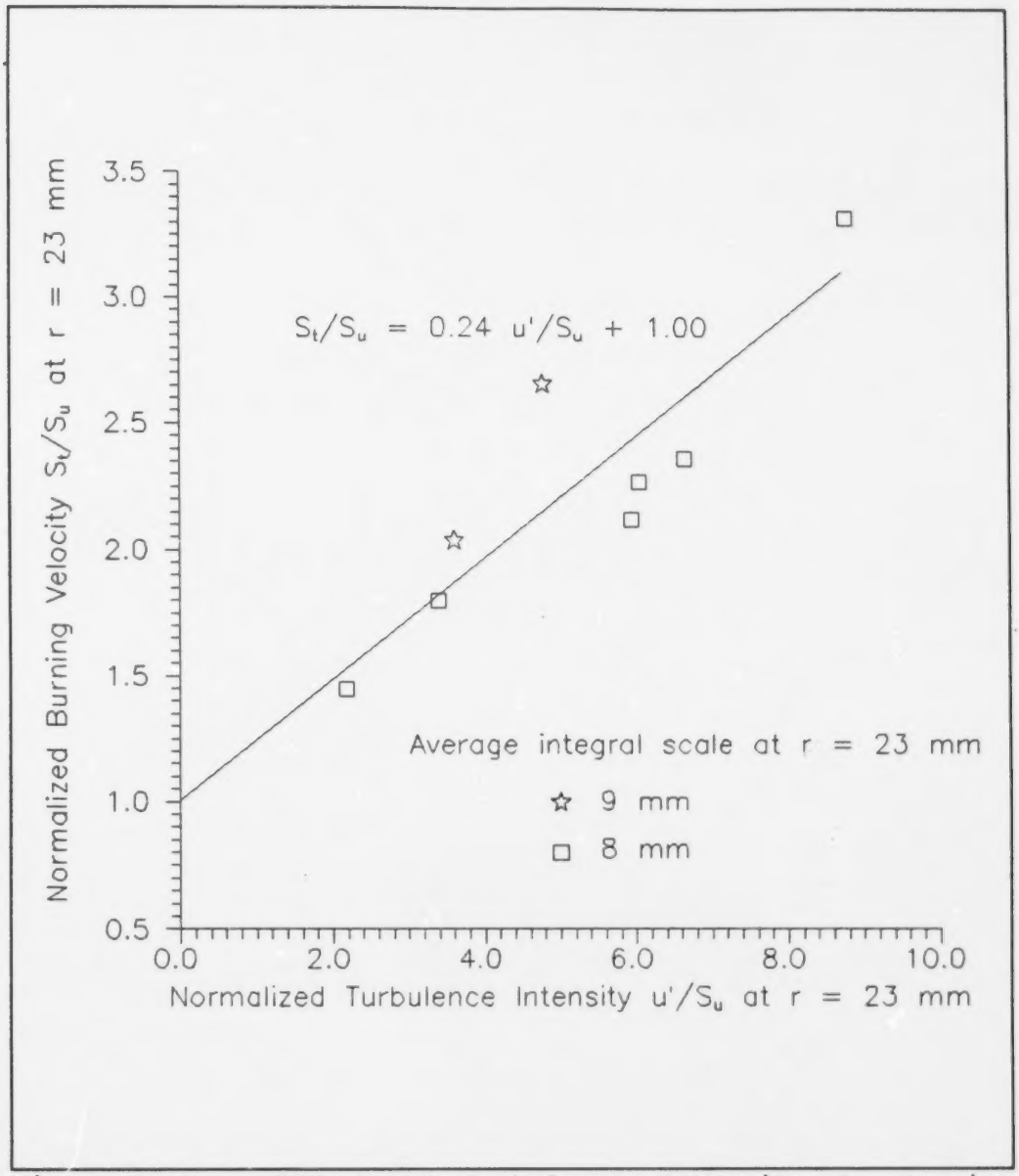

Figure 5.17 : Effect Of Turbulence Intensity On Burning Velocities Of Lean Methane-Air Flames (Ø = 0.76) At r = 23 mm. (T_u = 298 K, P = 104 kPa)

restrictions of the current image processing programs, which require a complete flame perimeter, no flame sizes greater than 62 mm diameter (r/R_{bomb} = 0.40) were measured from video images. At the early stages of flame growth, the pressure trace was very noisy as shown in Figures 5.15 and 5.16. Therefore, no direct comparison of the two methods (pressure-based and video image based) was possible. However, it is possible to obtain pressure-based results (with some higher noise level) down to a flame diameter of 60 mm.

Figure 5.18 shows a plot from the pressure-based method calculated at 68 mm flame diameter (T_u = 305 K, r/R_{bomb} = 0.45, P = 113 kPa). This figure shows a much weaker relationship between the burning velocity and turbulence intensity compared with the 110 mm flame diameter case.

$$\frac{S_t}{S_u} = 0.30 \frac{u'}{S_u} + 1.00 \qquad \textbf{5.11}$$

This confirms that the linear coefficient is weaker for smaller flames.

In summary, both pressure-based and image-based methods showed that the linear coefficient, C_L, increases as the flames grow from initial spark kernels. Even beyond the very early acceleration of the flame front mentioned in Agnew and Graiff [AG61], the flame continues to accelerate as it grows larger and larger. This acceleration is greater than that attributable to the increase in turbulence intensity due to rapid distortion. Therefore, the linear coefficient must be increasing with flame size.

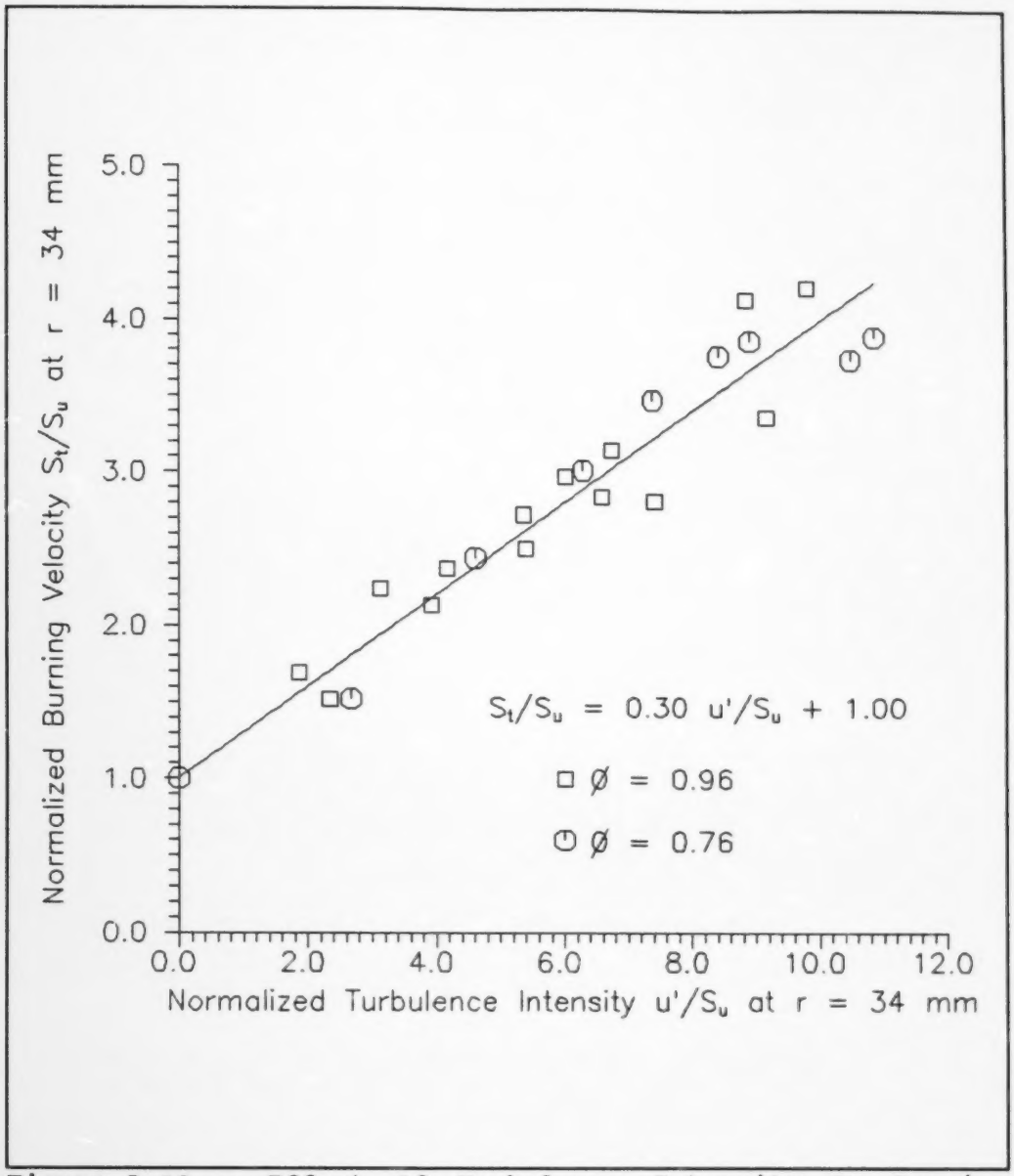

Figure 5.18 : Effect Of Turbulence Intensity On Burning Velocities Of Lean Methane-Air Flames At r = 34 mm. (T_u = 305 K, P = 113 kPa, Ø = 0.76 and Ø = 0.96 data combined)

5.4 The Effective Turbulence Intensity

The initial flame kernel is not exposed to the lower frequencies, larger eddies, in the turbulence. These larger eddies only convect the flame front as discussed by Abdel-Gayed and Bradley [AB87, AB86, AB84]. As the flame grows, progressively larger eddies become effective at shearing and distorting it.

For the cases studied here, due to the decaying turbulence and also the relatively large scales compared with laminar flame thickness, the effects of smaller scales die out quickly relative to the period of flame growth. In the present experimental apparatus, the small volume of the combustion chamber is probably inadequate for the flame to be fully developed, which would require it to be many times larger than the turbulent integral scale.

At this point, it is postulated that the increase in dependence of turbulent burning velocity on turbulence intensity, the linear coefficient, can be expressed as a function of flame size relative to the integral scale; that is,

$$\dot{C_L} = c_d \frac{r}{\Lambda_{actual}} \qquad 5.12$$

The dependence coefficient, c_d, indicates how strongly the linear coefficient depends on the normalized flame radius, r/Λ_{actual}.

5.4.1 Methane-Air Flames

For the methane-air flames, from ignition time to 110 mm diameter flames, the integral scale increased from 8 mm to 9 mm according to the normal decay model. After correcting for the flame

compression effect according to Equation 2.17, the integral scale actually decreases from 8 mm to 6 mm.

Figure 5.19 shows that the linear coefficient between S_t/S_u and u'/S_u for the lean methane-air flames studied can be given by:

$$C_L = 0.073 \frac{r}{\Lambda_{actual}} \qquad 5.13$$

5.4.2 Propane-Air Flames

For the lean propane-air case, no video images were recorded. Therefore, the change of linear coefficient with respect to flame size was found using the pressure trace at earlier stages of flame propagation.

Figure 5.20 shows the pressure-based results for 60 mm diameter flames (T_u = 305 K, r/R_{bomb} = 0.45, P = 113 kPa). The best linear fit line is described by Equation 5.14.

$$\frac{S_t}{S_u} = 0.60 \frac{u'}{S_u} + 1.00 \qquad 5.14$$

This equation shows a much weaker linear coefficient compared with the unity linear coefficient obtained for 110 mm diameter flames.

Due to the significant scatter in Figure 5.20, another location is required to confirm the dependence of linear coefficient on flame size. Figure 5.21 shows the plot of burning velocity at 92 mm diameter flame (T_u = 320 K, r/R_{bomb} = 0.60, P = 170 kPa) as a function of turbulence intensity. There is less scatter in this plot and hence the results give more confidence in

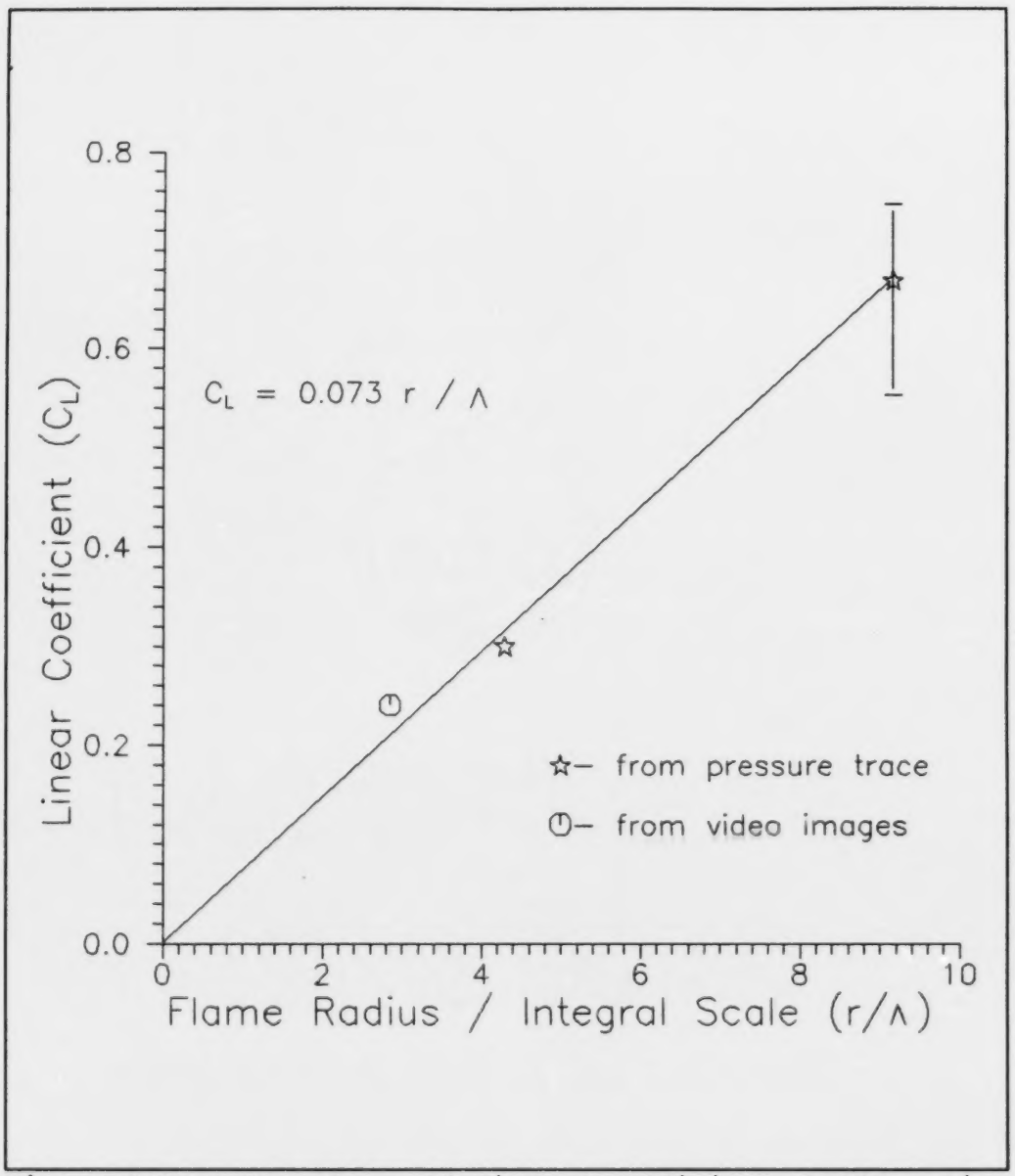

Figure 5.19 : Dependence Of Linear Coefficient On Flame Size (Lean Methane-Air).
(vertical solid line shows the estimated error due to different integral scales)

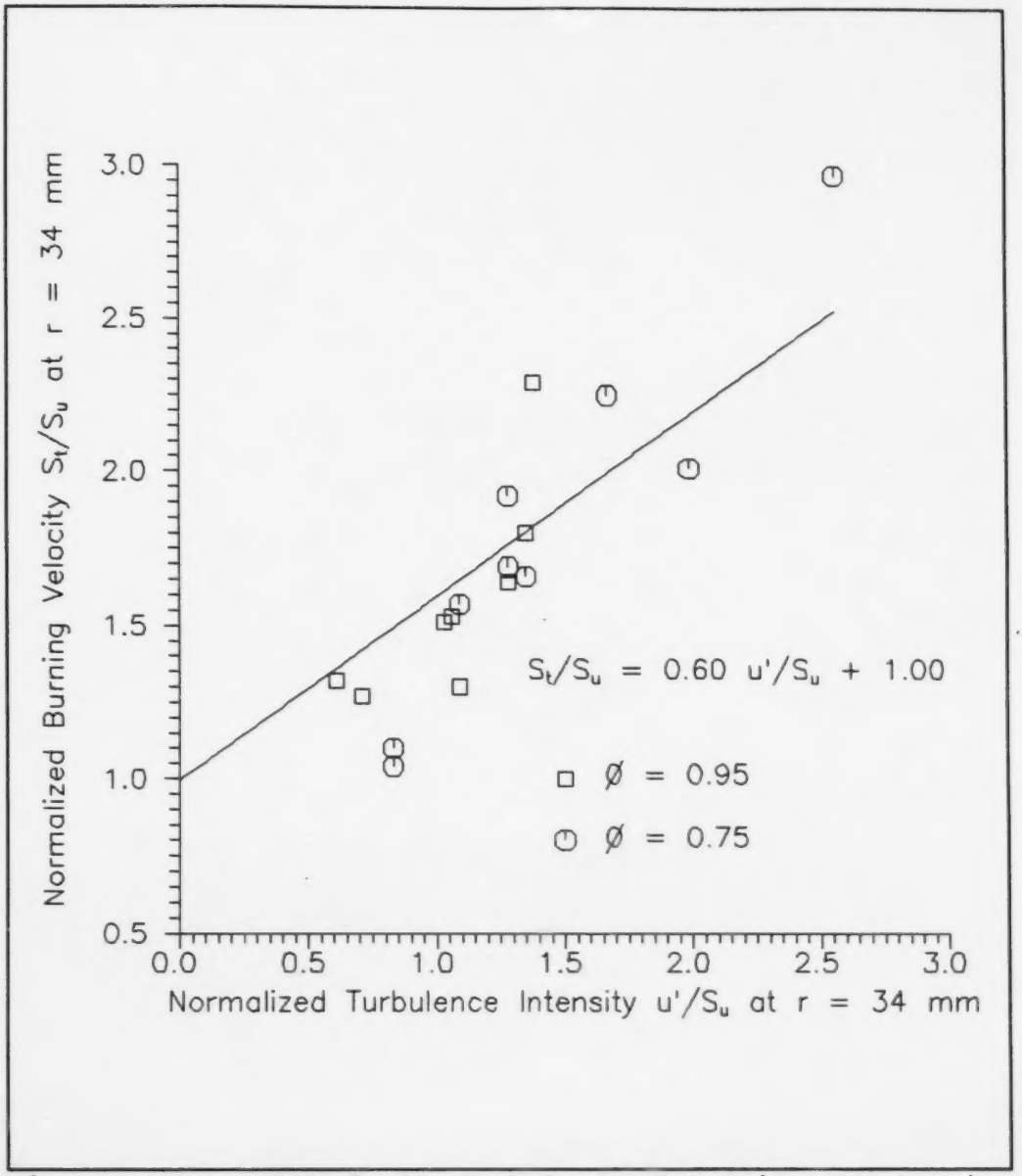

Figure 5.20 : Effect Of Turbulence Intensity On Burning Velocities Of Lean Propane-Air Flames At r = 34 mm. (T_u = 305 K, P = 113 kPa, Ø = 0.75 and Ø = 0.95 data combined)

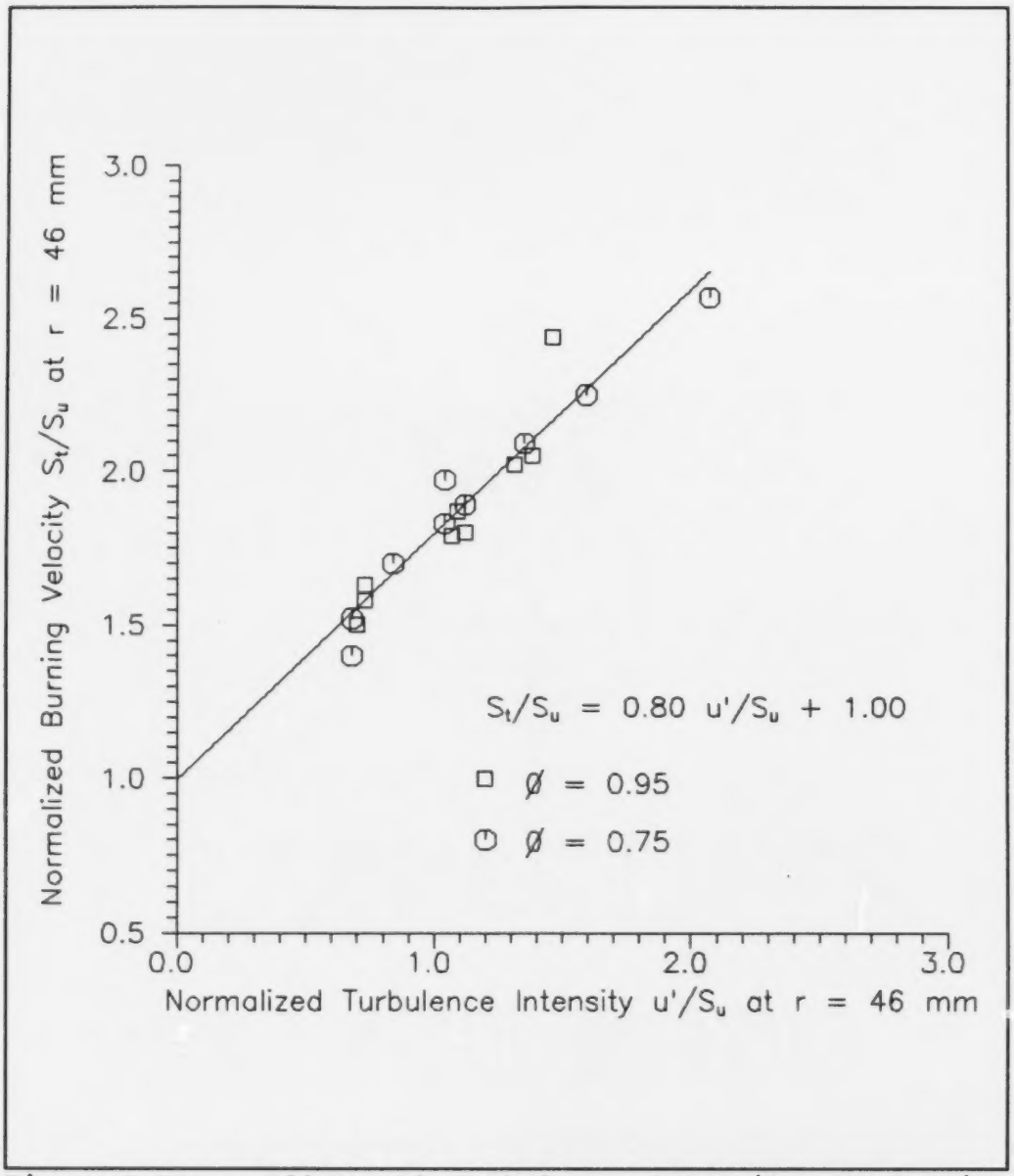

Figure 5.21 : Effect Of Turbulence Intensity On Burning Velocities Of Lean Propane-Air Flames At r = 46 mm. (T_u = 320 K, P = 135 kPa, Ø = 0.75 and Ø = 0.95 data combined)

the burning velocity and turbulence intensity relationship. The best fit line gives

$$\frac{S_t}{S_u} = 0.80 \frac{u'}{S_u} + 1.00 \qquad 5.15$$

Using the normal decay model, the integral scale increased from about 2 mm to approximately 3 mm at 110 mm diameter flame. After correcting for the temperature and pressure effects as described by Equation 2.17, the integral scale actually remained approximately constant at 2 mm.

The linear coefficient for this lean propane-air case is plotted against the relative flame radius (normalized by the integral scale) in Figure 5.22. The equation

$$C_L = 0.036 \frac{r}{\Lambda_{actual}} \qquad 5.16$$

describes the relationship between the linear coefficient and the flame size.

The dependence coefficient is much weaker for this lean propane-air case compared with that of the lean methane-air case. There are a few possible reasons for this factor of two difference. Using the perforated plate with 5 mm diameter holes, the eddies generated are much smaller ($\Lambda \approx 2$ mm) compared with those in the methane-air case ($\Lambda \approx 8$ mm). These smaller eddies become effective at shearing and distorting the flame front faster than the larger eddies of the methane-air case. While the integral scale of the methane-air case is only convecting the flame front, the integral scale of this propane-air case is already creating more wrinkling.

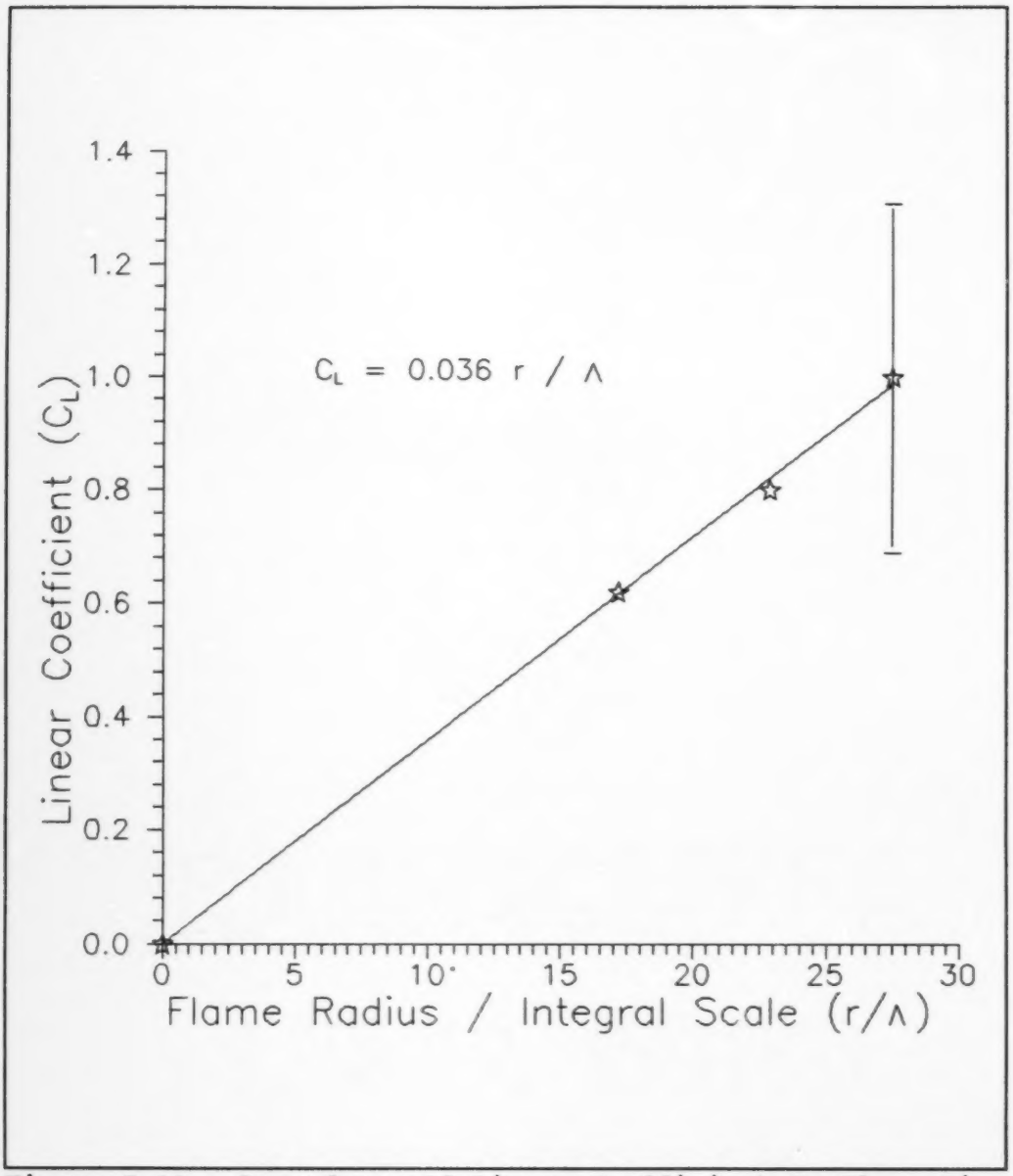

Figure 5.22 : Dependence Of Linear Coefficient On Flame Size (Lean Propane-Air).
(vertical solid line shows the estimated error due to different integral scales)

Using the very different scales and ranges of turbulence intensity for the two cases, propane-air and methane-air flames, the combustion mechanisms are expected to be different. Combustion in the lean propane-air case undergoes major effects due to relatively smaller eddies while combustion of the lean methane-air case depends mostly on large scale wrinkling. In addition, there could be a larger error involved in the propane-air case due to larger scatter of data points, less consistency in fixing integral scale and a lower purity fuel used. The discrepancies in linear coefficient and dependence coefficient could be caused by the different fuels used. This point can not be justified here until further experiments with the same fuel are performed using both 5 mm and 20 mm diameter plates under the same conditions.

5.5 Comparison Of Turbulent Burning Velocity With Published Results

The present results can be compared with the two-eddy theory of Abdel-Gayed and Bradley [AB81]. Their theory relates flame front advance to turbulent Reynolds number (R_A) based on the interaction between integral scale and Kolmogorov scale. The burning rate is a function of eddy decay and chemical reaction for large integral scale and dissipative Kolmogorov scale as discussed in Chapter 2.

Figure 5.23 shows the comparison between results obtained from the present study with those predicted by the two-eddy theory. The two dashed lines are the results predicted by the two-eddy theory over the two different ranges of turbulent Reynolds number considered. The solid line with equation

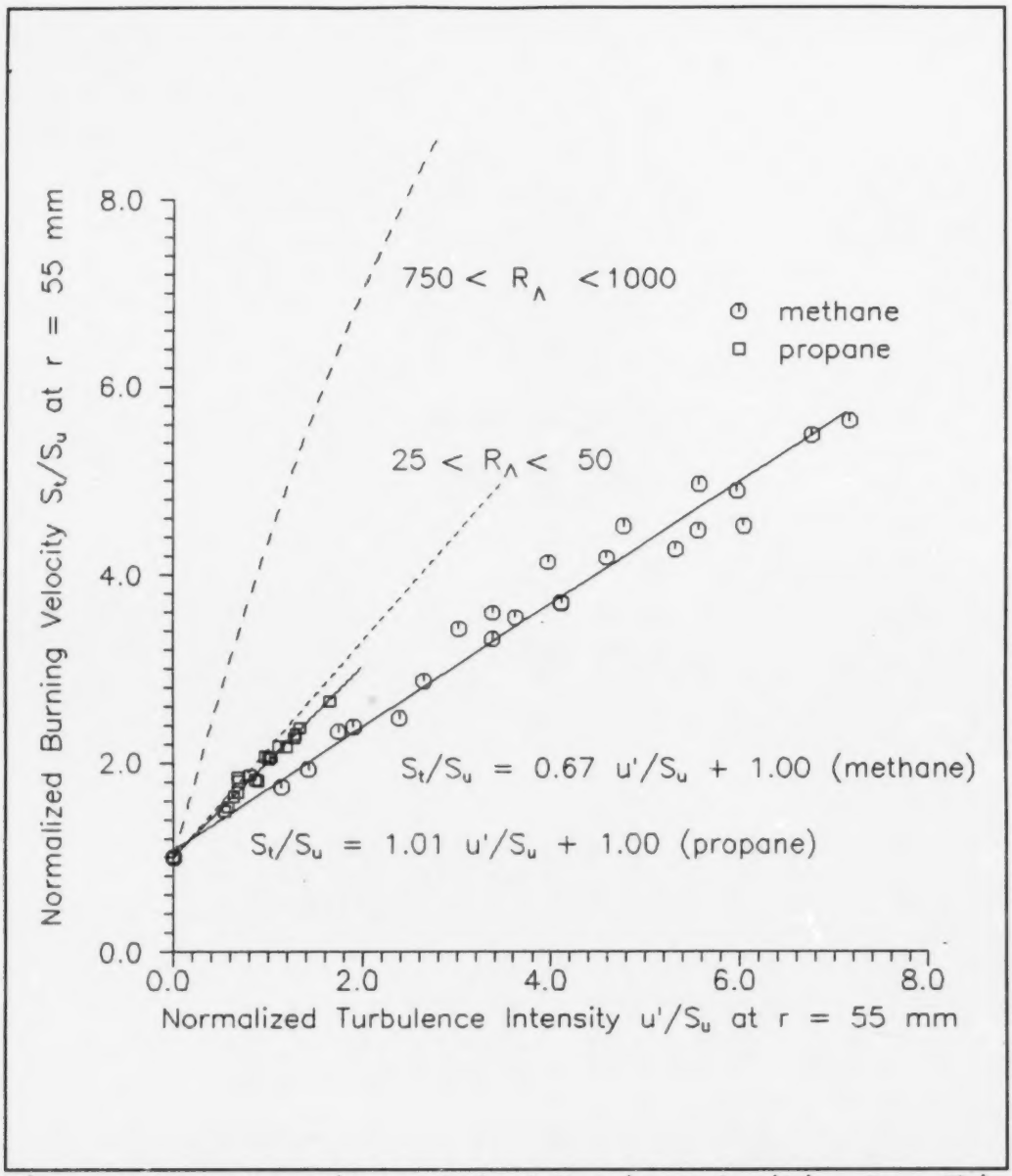

Figure 5.23 : Comparing Turbulent Burning Velocities From This Study (points) With The Two-Eddy Theory Of Abdel-Gayed And Bradley [AB81].

$$\frac{S_t}{S_u} = 1.01\frac{u'}{S_u} + 1.00 \quad (propane) \qquad 5.17$$

shows the best fit linear line for 110 mm diameter, lean propane-air flames. For 110 mm diameter, lean methane-air flames, a weaker linear coefficient is obtained from the present study as shown by the solid line labelled

$$\frac{S_t}{S_u} = 0.67\ \frac{u'}{S_u} + 1.00 \quad (methane) \qquad 5.18$$

For the 110 mm diameter, lean propane-air flames, R_A was estimated to be about 50. The two-eddy theory gives a linear coefficient of about 1 over the same range of turbulence intensities. The present 110 mm diameter, propane-air flames have a linear coefficient that agrees reasonably well with the prediction of the two-eddy theory, but slightly weaker.

With R_A of about 800 for the 110 mm diameter, lean methane-air flames, the two-eddy theory gives a slope of about 2 over the same range of turbulence intensities. This slope or linear coefficient is about 3 times the value obtained from the present 110 mm diameter, lean methane-air flames.

For the present methane-air results to agree with those of the two-eddy theory, the value for r/Λ_{actual} has to be about 27. The flame radius has to be about 27 times larger than the integral scale in order for the available turbulence to be totally effective. This value of r/Λ_{actual} seems high because it requires the flame diameter to be 55 times larger than integral scale. There are two possible

reasons why the stirred bomb results of Abdel-Gayed and Bradley would lead to this value. First, they used the progress of the leading edge of the flame front to calculate the burning velocity. This would give a larger burning velocity than the mean position obtained from current pressure-based results. The other reason is the continuous enhancement of burning velocity by the smaller scales in their stirred bomb. This is not present in this decaying turbulence. Cant and Bray [CB89] found that the turbulent conditions in a stirred bomb cause combustion to take place much more rapidly than in natural decaying turbulence.

With the above explanation of the discrepancy between the present methane-air results with the prediction of the two-eddy theory, it becomes obvious why the propane-air result agrees with that predicted by the two-eddy theory. For the propane-air flames studied, because of the small scale turbulence used, the flames are almost fully developed at diameters of 110 mm according to the two-eddy theory. It happened that at the 110 mm diameter flame size considered in this study, the effectiveness of the turbulence coincided with that predicted by the two-eddy theory. For the 110 mm diameter flame, the integral scale was about 1/28 of the flame radius. This is consistent with the methane-air case which must be extrapolated to $r/\Lambda_{actual} = 27$ for the present result to agree with that predicted by the two-eddy theory. In short, the two-eddy theory seems consistent in predicting a flame diameter to integral scale ratio of 55 for a fully developed spherical flame.

CHAPTER 6: CONCLUSIONS AND RECOMMENDATIONS

6.1 Conclusions

6.1.1 Pressure Effects On Laminar Burning Velocities

The pressure effects on laminar burning velocities of lean propane-air and lean methane-air gas mixtures were investigated by varying the initial pressure from 0.5 to 2.6 atm. The pressure exponents and burning velocities were compared with those in the literature.

The pressure exponents for the propane-air flames were about -0.6 compared with the more acceptable value of -0.2. Some researchers [Gl87, Ku87, Ku60] found that the pressure exponent varied with temperature, pressure, chemical reaction involved and burning velocity. As a result, the published pressure exponents ranged from -0.1 to -0.7.

Despite the different pressure effects, laminar burning velocities of propane-air flames at atmospheric conditions agreed with those in the literature. In general, the laminar burning velocities from this study are slightly higher than the more acceptable values in the literature.

The methane-air case produced more consistent results than the propane-air case. The higher consistency resulted from both a higher purity fuel and a wider range of initial pressure used. The pressure exponents varied from -0.58 to -0.71 compared with -0.5 obtained by Bradley and Hundy [BH71]. The burning velocities of

methane-air flames are within 10% difference compared with the more acceptable published results.

In both propane-air and methane-air cases, the pressure effect on laminar burning velocity decreases with increasing lean equivalence ratio. This is consistent with other results.

6.1.2 Effects Of Eddy Scales On Turbulent Burning Velocities

In this study, the perforated plate with 5 mm diameter holes was used for the propane-air tests and the perforated plate with 20 mm hole diameter holes was used for the methane-air tests. With a fixed plate hole diameter for either case, the integral scale was only varied over a small range.

With less than 20% changes in integral scale, the effect on turbulent burning velocity was negligible. From propane-air case to methane-air case, the linear coefficient, C_L, decreased from 1 to 0.65 for a 110 mm diameter flame. This significant decrease in linear coefficient could be due to the large increase in integral scale (2 to 8 mm). However, as the fuels are different, the conclusion that small scale turbulence is more effective in enhancing the burning velocity can not be confirmed.

6.1.3 Effects Of Turbulence Intensity On Turbulent Burning Velocities

The turbulence at the measurement time was found to correlate better with burning velocity than the ignition-time turbulence. The relationship between ignition-time turbulence and turbulent burning

velocities during the combustion process was very non-linear and misleading. Therefore, measurements of u'/S_u effects on S_t/S_u must properly model rapid distortion and turbulence decay effects.

Turbulence intensity has a strong effect on burning velocity. There is a linear relationship between the normalized turbulent burning velocity and turbulence intensity for both lean propane-air and lean methane-air cases. In either the propane-air or the methane-air case studied, the relationship was the same for lean mixtures (ϕ = 0.75) and rich mixtures (ϕ = 0.95). The linear coefficient between normalized turbulent burning velocity and turbulence intensity was the same at both equivalence ratios.

The linear coefficient, C_L, increases as the flame grows. For the propane-air case, the linear coefficient increased from 0.6 to 1.0 as the flame diameter increased from 60 mm (T_u = 305 K, r/R_{bomb} = 0.45, P = 113 kPa) to 110 mm (T_u = 340 K, r/R_{bomb} = 0.72, P = 170 kPa). In the lean methane-air case, the linear coefficient increased from 0.3 to 0.7 as the spherical flame grew from 46 mm (T_u = 298 K, r/R_{bomb} = 0.3, P = 104 kPa) to 110 mm (T_u = 340 K, r/R_{bomb} = 0.72, P = 170 kPa) in diameter.

It was postulated that the linear coefficient can be related to the normalized flame radius, r/Λ_{actual},

$$C_L = c_d \frac{r}{\Lambda_{actual}} \qquad 6.1$$

The dependence coefficient, c_d, was found to be 0.036 for the lean propane-air case and 0.073 for the lean methane-air case.

6.1.4 Flame Growth From High Speed Video

The flame growth measured from the high speed video images was found to be faster than that obtained from the pressure trace. This difference in flame growth increases with turbulence intensity and flame size.

The Schlieren system is expected to measure the leading edge of the flame front while the pressure trace gives the central flame front position. For a laminar flame ignited at 1 atm and 296 K, the difference in flame size measured by the two independent methods (pressure trace and video image) was found to be greater than this amount. A 13% difference in flame radius (4 mm) was obtained for a 30 mm radius flame. The difference other than the flame thickness was mostly due to error in the area calculation program used. The image processing program detected a larger area than the actual flame size. With the 13% difference in flame size, the burning velocity calculated from the video images was about 30% higher than that from the pressure trace. This 30% difference was due to the square of the flame radius difference.

6.1.5 Effect Of Rapid Distortion In A Closed Chamber Combustion

Rapid distortion has a significant effect on the later stages of combustion in the closed combustion chamber. The rapid distortion increases the turbulence intensity in the normal direction significantly, while tending to reduce the turbulence intensity in the transverse directions.

There appeared to be more scatter of data points if the

contribution of rapid distortion due to the transverse components is omitted. Whether or not the transverse components of the turbulence should be omitted in rapid distortion analysis cannot be demonstrated from these results.

6.2 Recommendations

6.2.1 Pressure And Temperature Effects On Laminar Burning Velocities

The effects of pressure on laminar burning velocities were found to be larger than the more acceptable results from the literature. Further study of this case can be carried out over a wider range of pressure with a higher purity of fuel, especially propane.

As the initial temperature was fixed at 23°C throughout this study, the temperature effects were not studied. The proper way to study this temperature effect on burning velocity would be to preheat the combustion chamber to vary the initial temperature. This temperature effect, if obtained, can be compared with the published results. The temperature effect could explain some of the disagreements between present results and those of others.

6.2.2 Turbulence Measurements

The actual turbulence during the process of combustion is still questionable. Checkel's wind tunnel equations (unpublished work) used the same set of equations for all perforated plates.

However, McDonell's measurements [Mc88] found that the equations for each plate could be quite different. At this point, it is believed that the difference from plate to plate is likely due to the change in the ratio of plate hole diameter to plate thickness. Using the design of an orifice for the holes on the perforated plates would probably minimize this plate thickness effect on the turbulence generated.

6.2.3 Correlating Eddy Scales With Turbulent Burning Velocities

It is difficult to correlate eddy scales with burning velocity accurately using a closed bomb method. This is due to different rates of turbulence decay which result in different scales and turbulence intensities throughout the combustion process. Moreover, rapid distortion affects the turbulence condition significantly, especially at the later stages of combustion.

Only the pre-ignition eddy scales and turbulence intensity can be controlled accurately. At ignition or immediately after this, the flame kernel is too small to produce any measurable pressure rise. Other factors that further complicate the analysis of a small flame kernel include large flame thickness, curvature and quenching effects.

Burner methods may be used as an independent method for studying the effect of eddy scales on burning velocity. This is because steady scales can be maintained at a specific location.

Despite the problems encountered using the present cubical combustion chamber, the present combustion chamber represents the

actual internal combustion engine closely.

Further studies on the effects of eddy scales on the burning velocity can be carried out using different plates but keeping the mixture the same. The results obtained from these studies would probably explain the changing dependence coefficient, c_d of Equation 6.1. Similar cubical combustion chambers with larger and smaller volumes than the present chamber could be used to validate the developing turbulent flame results.

6.2.4 High Speed Video Images

In this study, the use of images obtained from the high speed video was limited by both the image processing method and the small window of the combustion chamber. The image processing program tends to include area beyond the flame front and should be improved.

The window on the combustion chamber could be widened and centralized. This would allow the capture of the flame front by the video up to the point where the flame front touches the walls.

REFERENCES

[AB72] G.E. Andrews and D. Bradley, "The Burning Velocity of Methane-Air Mixtures", Combustion and Flame 19: pp 275-288, 1972

[AB81] R.G. Abdel-Gayed and D. Bradley, "A Two-Eddy Theory of Premixed Turbulent Flame Propagation", Phil. Trans. R. Soc. London, A301, pp 1-25, 1981

[AB84] R.G. Abdel-Gayed, D. Bradley, M.N. Hamid and M. Lawes, "Lewis Number Effects on Turbulent Burning Velocity", Twentieth Symposium (Intl) on Combustion, pp 505-512, 1984

[AB87] R.G. Abdel-Gayed, D. Bradley and M. Lawes, "Turbulent Burning Velocities: a general correlation in terms of straining rates", Proc. R. Soc. Lond. A. 414. 389-413, 1987

[AG61] J.T. Agnew and L.B. Graiff, " The Pressure Dependence of Laminar Burning Velocity by the Spherical Bomb Method", Combustion and Flame 5: pp 209-219, 1961

[Be77] R.S. Benson, Advanced Engineering Thermodynamics, Pergamon Press Ltd., 2nd Ed., 1977

[BH71] D. Bradley and G.F. Hundy, "Burning Velocities of Methane-Air Mixtures using Hot-Wire Anemometers in Closed-Vessel Explosions", Thirteenth Symposium (Int) on Combustion, pp 575-583, 1971

[BL75] D.R. Ballal and A.H. Lefebvre, "The Structure and Propagation of Turbulent Flames", Proc. R. Soc. Lond. A.344, pp 217-234, 1975

[BP51] W.D. Baines and E.G. Peterson, "An Investigation of Flow Through Screens", Trans. of the ASME, Vol 73, p. 467, 1951

[BT37] C.L. Bouchard, C.F. Taylor and E.S. Taylor, "Variables Affecting Flame Speed", SAE J., Vol 41, No 5, 1937

[CB88] R.S. Cant and K.N.C. Bray, "Strained Laminar Flamelet Calculations of Premixed Turbulent Combustion in a Closed Vessel", Twenty-Second Symposium (Int) on Combustion, pp 791-799, 1988

[CB88a] T.C.Chew and R.E. Britter, "Effect of Geometrical Straining on Turbulence Levels in Explosions and Common Burner Configurations", Cambridge University Engineering Department report, 1988

[CB89] R.S. Cant and K.N.C. Bray, "A Theoretical Model of Premixed Turbulent Combustion in Closed Vessels", Combustion and Flame 76: pp 243-263, 1989

[CC66] G. Comte-Bellot and S. Corrsin, "The Use of a Contraction to Improve the Isotropy of Grid-generated Turbulence", Journal of Fluid Mechanics, Vol 25, p. 657, 1966

[Ch81] M.D. Checkel, Turbulence Enhanced Combustion of Lean Mixtures, PhD Thesis, Cambridge University, 1981

[Ch86] M.D. Checkel, "Measurements of Turbulence Behind 60% Solid Perforated Plates", ASME Trans., J. of Fluids Engineering, March 1986

[CT83] M.D. Checkel and A. Thomas, "Turbulent Explosions in Closed Vessels", Paper C57/1983, Combustion in Engineering, I.Mech.E., Oxford, 1983

[Di67] W.A. Dietz, "Response Factors for Gas Chromatographic Analyses", J. of G. C., February 1967

[DO81] J.D. Dale and A.K. Oppenheim, "Enhanced Ignition for I.C. Engines with Premixed Gases", SAE 810146, 1981

[El28] O.C. Ellis, "Flames Movement in Gaseous Explosive Mixtures", Fuel 7, p. 245, 1928

[EW27] O.C. Ellis and R.V. Wheelers, "The Movement of Flame in Closed Vessels: After Burning", J. Chem. Soc., pp 310-322, 1927

[Fr48] F.N. Frenkial, "The Decay of Isotropic Turbulence", Trans. of the ASME, Vol 70, p. 311, 1948

[Fr65] R.M. Fristrom, "Definition of Burning Velocity and a Geometric Interpretation of The Effects of Flames Curvature", Phys. of Fluids 8 (2), pp 273-280, 1965

[Gi57] M. Gilbert, "The Influence of Pressure on Flame Speed", Sixth Symposium (Int) on Combustion, pp 74-83, 1956

[Gl87] I. Glassman, Combustion, Academic Press, 2nd Ed., 1987

[Gr85] R.L. Grob, Modern Practice of Gas Chromatography, 2nd Ed., John Wiley and Sons, 1985. See Chapter Six, M.J. O'Brien, "Detectors"

[Hi75] J. Hinze, Turbulence, McGraw-Hill, 2nd Ed., 1975

[HS87] C.M. Ho and D.A. Santavicca, "Turbulence Effects on Early Flame Kernal Growth", SAE 872100, 1987

[Ku60] D.K. Kuehl, "Laminar-Burning Velocity of Propane-Air Mixtures", Eigth Symposium (Int) on Combustion, pp 510-521, 1960

[Ku86] K.K. Kuo, Principles of Combustion, John Wiley & Sons, 1986

[LA87] M.T. Lim, R.W. Anderson and V.S. Arpaci, "Prediction of Spark Kernel Development in Constant Volume Combustion", Combustion and Flames 69: pp 303-316, 1987

[LK76] D.R. Lancaster, R.B. Krieger, S.C. Sorenson and W.L. Hull, "Effect of Turbulence on Spark Ignition Engine Combustion", SAE 760160, 1976

[LL88] Y. Liu and B. Lenze, "The Influence of Turbulence on the Burning Velocity of Premixed CH_4-H_2 Flames with Different Laminar Burning Velocities", Twenty-Second Symposium (Int) on Combustion, pp 747-754, 1988

[LV68] B. Lewis and G. von Elbe, Combustion, Flames and Explosions of Gases, Academic Press Inc., 2nd Ed., 1968

[Pa89] F. Paschen, Wied. Ann., 37, 69, 1889

[Mc88] B.J. McDonell, Burning Rates of Propane-Air Mixtures in Homogeneous Decaying Turbulence, MSc Thesis, Department of Mechanical Engineering, University of Alberta, 1988

[MC88] R.M. Modien and M.D. Checkel, "The Effect of High Intensity Turbulence and Turbulence Scale on Burning Velocity for 85% Stoichiometric Methane-Air Mixtures", The Combustion Institute / Canadian Section, Spring Technical Meeting, June 1988

[MK80] M. Metghalchi and J.C. Keck, "Laminar Burning Velocity of Propane-Air Mixtures at High Temperature and Pressure", Combustion and Flame 38: pp 143-154, 1980

[Mo90] R.M. Modien, The Effects of Enhanced Ignition Systems and Turbulence on Flame Development, MSc Thesis, Department of Mechanical Engineering, University of Alberta, 1990

[OH71] S. Ohigashi, Y. Hamamoto and A. Kizima, "Effects of Turbulence on Flame Propagation in Closed Vessels", Bull. of the JSME, Vol 14, No 74, 1971

[OI84] S. Okajima, K. Iinuma, S. Yamaguchi and S. Kumagai, "Measurement of Slow Burning Velocities and Their Pressure Dependence using a Zero-Gravity Method", Twentieth Symposium (Int) on Combustion, pp 1951-1956, 1984

[PC89] Propane-Carburation, some technical considerations, 1989

[RB73] D.M. Rosie and E.F. Barry, "Quantitation of Thermal Conductivity Detectors", Journal of Chromatographic Science, Vol 11, 1973

[Re87] W.C. Reynolds, "STANJAN, An Interactive Program for Equilibrium Analysis by the Method of Element Potentials", v 3.81, Mechanical Engineering Department, Stanford University, 1987

[RG80] C.J. Rallis and A.M. Garforth, "The Determination of Laminar Burning Velocity", Prog. Energy Combust. Sci., Vol 6, pp 303-329, 1980

[Th86] A. Thomas, "The Development of Wrinkled Turbulent Premixed Flames", Combustion and Flames 65 : 291-312, 1986

[TS88] R.E. Teets and J.A. Sell, "Calorimetry of Ignition Sparks", SAE 880204, 1988

[UW67] M.S. Uberoi and S. Wallace, "Effects of Grid Geometry on Turbulence Decay", The Physics of Fluids, Vol 10, No 6, p. 1216, 1967

[VS90] B.D. Videto and D.A. Santavicca, "Flame-Turbulence Interactions in a Freely-Propagating, Premixed Flame", Combust. Sci. and Tech., Vol 70, pp 47-73, 1990

[VS78] G.J. Van Wylen and R.E. Sonntag, Foundamentals of Classical Thermodynamics, John Wiley and Sons, 2nd Ed., 1978

[Wi85] F.A. Williams, Combustion Theory, The Benjamin/Cummings Publishing Company, Inc., 2nd Ed., 1985

[Ze41] Y.B. Zeldovich, Zh. Eksp. Teor. Fiz. 11, 159 (1941). See Y.S. Shchetinkov, "The Physics of the Combustion of Gases", Chapter 5, Edited Translation FTD-HT-23-496-68, Translation Revision, Foreign Technology Division, Wright-Patterson AFB, Ohio, 1969

Appendix A : Burning Velocity Calculations

This appendix describes the burning velocity calculations based on pressure traces. The geometric method used in this study was compared with the simple Lewis and von Elbe method [LV68].

The multi-zone thermodynamic equilibrium model was used in a program (NBPMAK.bas) to generate arbitrary pressure traces. These pressure traces were generated with constant burning velocity of 0.4 m/s. The initial spark kernel was fixed with a radius of 5 mm and the time step used was 0.5 ms. At each time step, the volume burned was increased by burning a new volume equal to the previous flame area multiplied by 0.4 m/s.

The Lewis and von Elbe method was used to calculate the corresponding burning velocity based on the equilibrium pressure obtained from STANJAN [Re87]. This burning velocity was compared with the "original" burning velocity calculated as

$$S_u = \frac{dV_{bb}}{4\ \pi\ R_{last}^2\ dt} \qquad \textbf{A.1}$$

where S_u = Burning Velocity

dV_{bb} = Volume of the Burning Element before burning

R_{last} = Radius after the last element burnt

dt = time step

The "original" burning velocity should give exactly the original 0.4 m/s.

The burning velocity calculated by the analysis program is slightly different since it divides the incremental volume burned

by the geometric average of current and previous flame areas. The burning velocity calculation based on the geometric method is calculated as

$$S_u = \frac{R_i - R_{flame}}{dt} \qquad \text{A.2}$$

where R_i = Flame Radius before burning

R_{flame} = Geometric Mean Flame Radius described as

$$R_{flame} = \sqrt{\frac{R_{last}^2 + R_b^2}{2}} \qquad \text{A.3}$$

where R_b = Flame Radius

Figures A.1 and A.2 show the burning velocity results for 75% and 95% stoichiometric methane-air flames respectively. These methane-air mixtures were theoretically ignited at 1 atm and 296 K. The burning velocities based on the geometric method increased asymptotically towards 0.4 m/s as expected. This confirms that the geometric flame calculation works with the smooth pressure trace generated by NBPMAK.bas.

To test all of the analysis programs, theoretical results obtained from NEWBOMB.bas program were used to interpolate the pressure trace generated by NBPMAK.bas. The procedure is the same as that used in analyzing burning velocity from an experimental pressure trace. Program NEWBP2.bas was used to interpolate the pressure trace (generated from NBPMAK.bas) with the theoretical values to get the corresponding burning temperature, specific heats, unburnt and burnt volumes, mass burnt, and flame radius.

After interpolation, the resulting parameters were used to calculate the final burning velocity. Figures A.3 and A.4 show the final burning velocities (after interpolation) for the 75% and 95% stoichiometric methane-air mixtures respectively. The final burning velocities based on the "original" method show higher burning velocities initially. These higher burning velocities were due to the large initial burnt volume resulting from the large spark volume used. The larger burning volume affects the initial burning velocities via dV_{bb} used in Equation A.1.

The "geometric" burning velocity is the one used in real analysis. The fluctuation in the final burning velocities based on the "geometric" method was due to interpolation error. In the actual procedure when dealing with experimental pressure traces, the calculated burning velocities were filtered and a linear fit between 84 and 115 mm diameter was used to estimate the burning velocity. Choosing 75% stoichiometric methane-air mixture at R_{flame} = 55 mm, the "geometric" model should be expected to read 0.38 m/s (Figure A.1) and actually obtains 0.39 m/s (Figure A.3). This is taken as confirmation that the analysis programs can correctly analyze a pressure trace with known burning velocity.

References:

[LV68] B. Lewis and G. von Elbe, Combustion, Flames and Explosions of Gases, Academic Press Inc., 2nd Ed., 1968

[Re87] W.C. Reynolds, "STANJAN, An Interactive Program for Equilibrium Analysis by the Method of Element Potentials", v 3.81, Mechanical Engineering Department, Stanford University, 1987

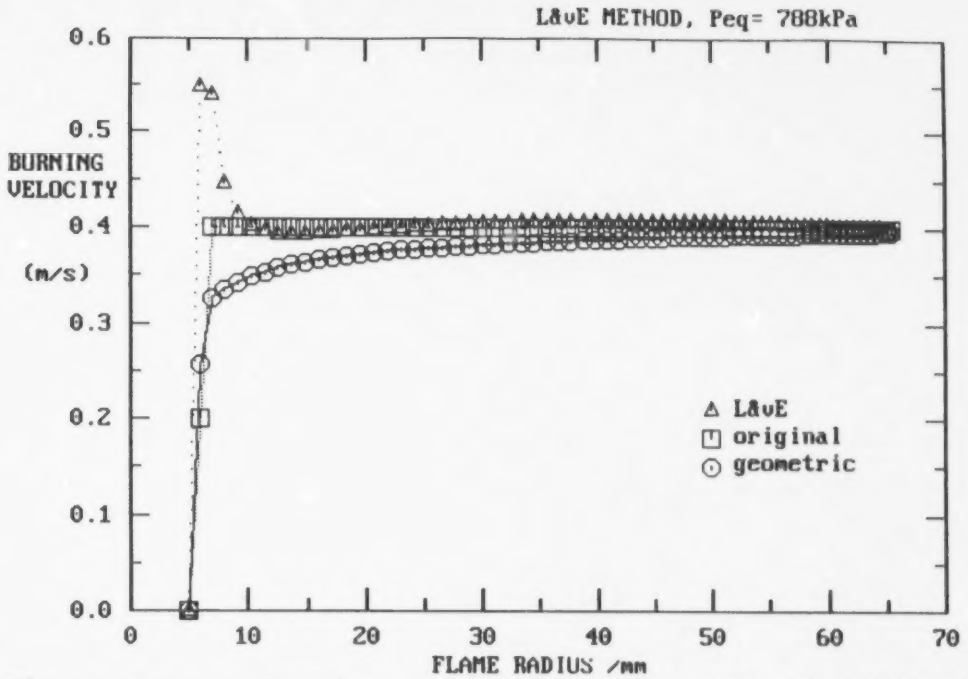

Figure A.1 : Burning Velocities For 75% Stoichiometric Methane-Air Mixture Ignited At 1 atm and 296 K.

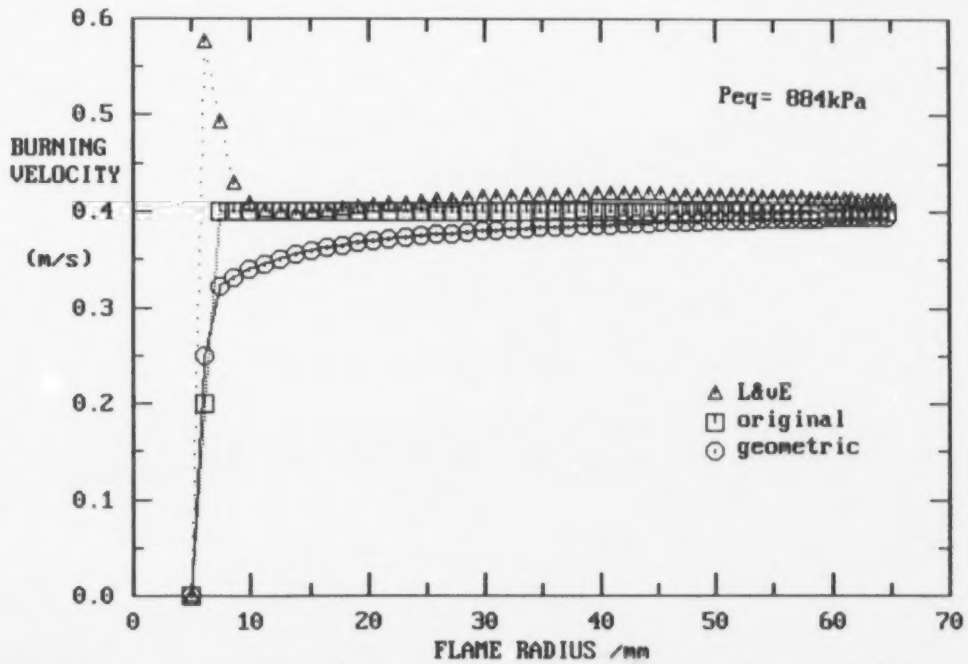

Figure A.2 : Burning Velocities For 95% Stoichiometric Methane-Air Mixture Ignited At 1 atm and 296 K.

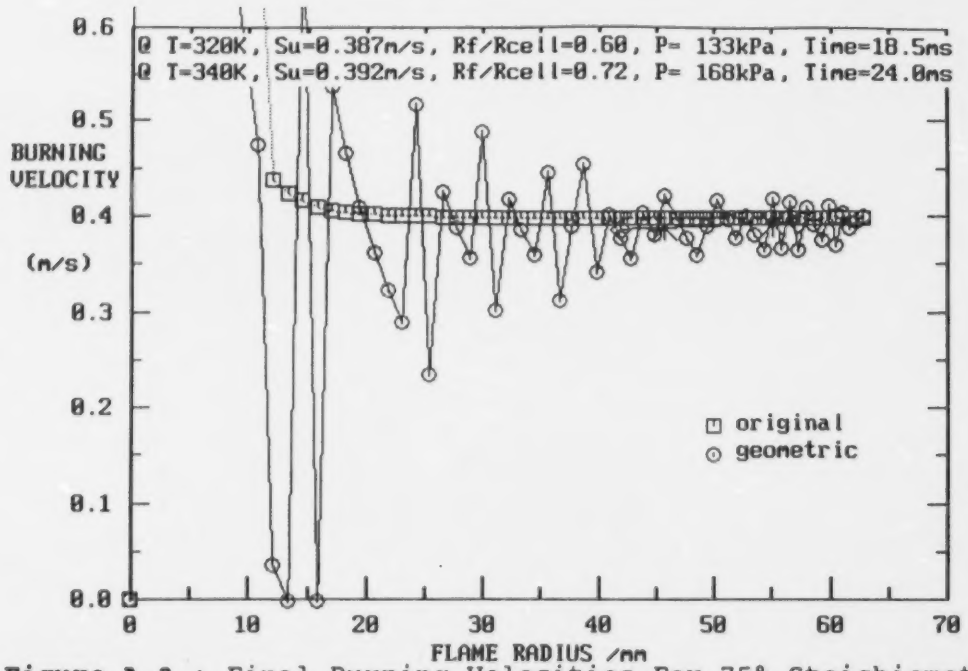

Figure A.3 : Final Burning Velocities For 75% Stoichiometric Methane-Air Mixture Ignited At 1 atm and 296 K.

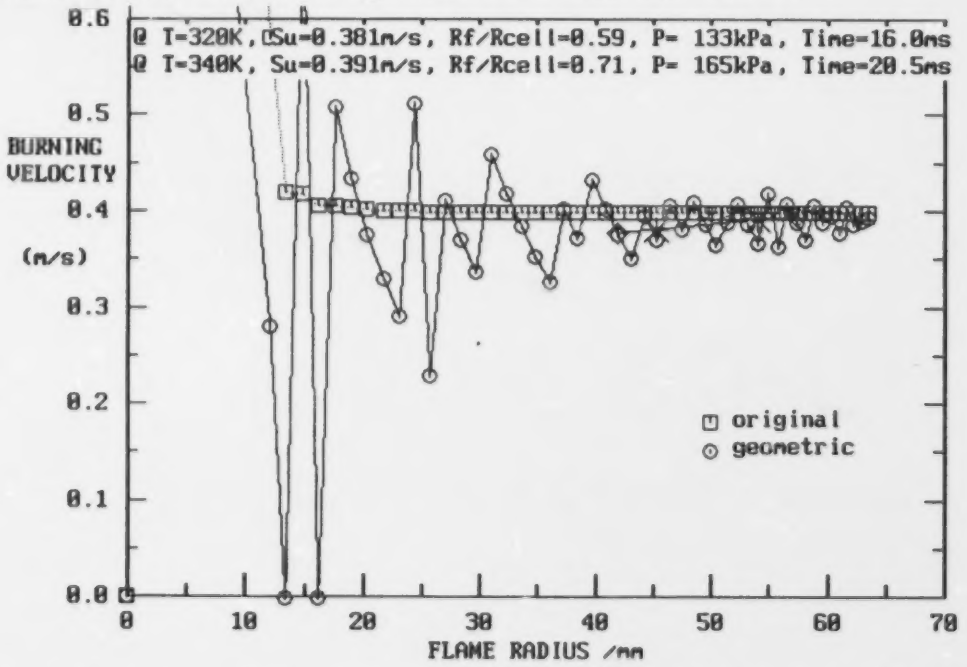

Figure A.4 : Final Burning Velocities For 95% Stoichiometric Methane-Air Mixture Ignited At 1 atm and 296 K.

Appendix B : Air-Fuel Mixer Calibration

This appendix details the actual re-calibration of air-fuel mixer performed on September 1990.

Figure B.1 shows a schematic of the actual air-fuel mixer used in the experiment. This apparatus regulates the volumetric flow rates of the gases through the critical flow orifices and then mixes them to produce homogeneous mixtures with the mixer.

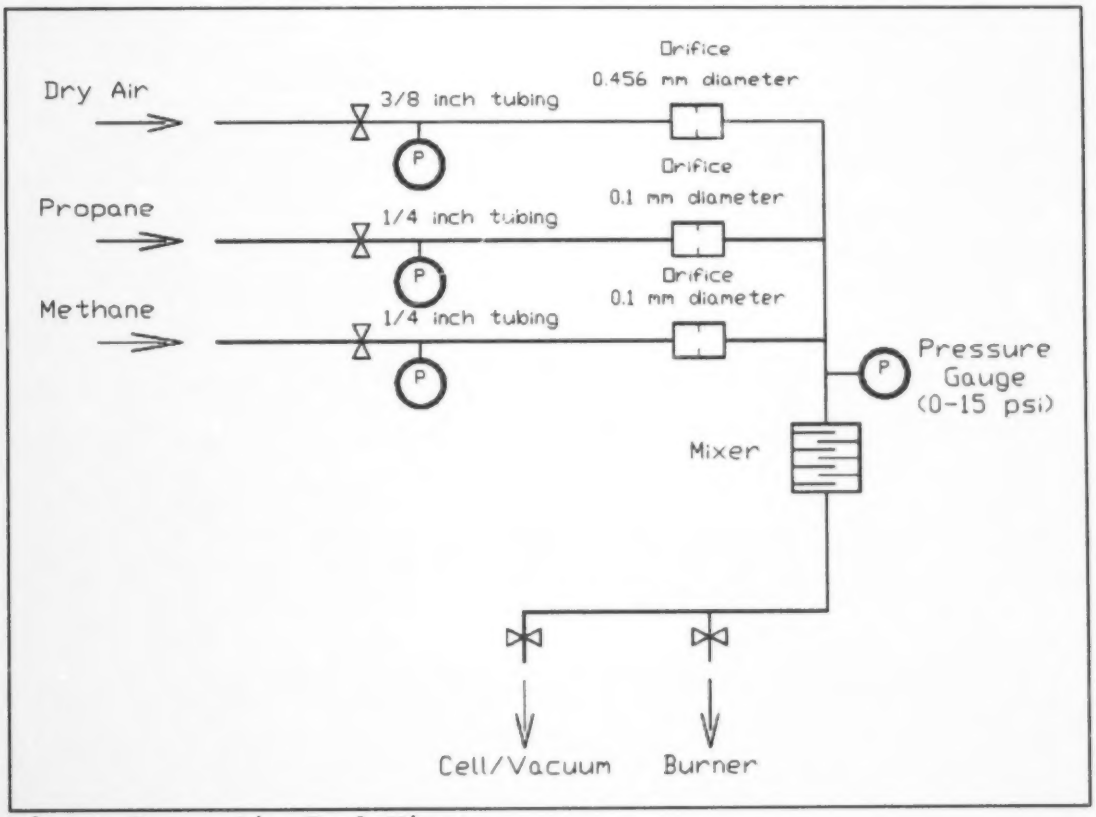

Figure B.1 : Air-Fuel Mixer.

Flow regulation operates by using critical (choked) flow orifices. The critical flow orifices are made of brass orifice plates with diameters of 0.1 mm for the fuels and 0.456 mm for the air. Once critical flow is obtained, the flow is only a function of the upstream gas pressure and temperature. With approximately constant room temperature, the flow rate is directly proportional to the upstream gas pressure.

Critical flow is achieved when the upstream pressure is sufficiently larger than the critical pressure, P^* of equation B.1 [WS78].

$$\frac{P^*}{P_{up}} = \left(\frac{2}{\gamma + 1}\right)^{\frac{\gamma}{\gamma - 1}} \qquad \textbf{B.1}$$

where γ = specific heat ratio

P^* = critical (downstream combustion chamber) pressure

P_{up} = upstream gas pressure

Setting the fuel gas (methane or propane) pressures at 220 kPa, the upstream air pressure was varied to obtain the required mixture stoichiometry for a downstream pressure of 1 atm. Table B.1 shows the specific heat ratio at 300 K and the corresponding minimum upstream pressure for each gas.

The upstream air pressure was calibrated to flow rate using a rotameter (Century Flowmeter Kit, Tube Catalog No 448-324 with 0.25 inch diameter of Black CD Glass). The flow rate was corrected to

standard conditions (25°C and 700 mm Hg) and plotted on Figure B.2.

The propane and methane flow rates, being too low for practical rotameter application, were calibrated using the "Bubble in Burette" technique as shown in Figure B.3. The rubber ball was squeezed until the level of the bubble fluid was above the mouth of the tube through which the mixer gas passed through. The rise of the bubble through the 100 ml burette was timed to obtain the flow rate. These flow rates were also corrected to standard conditions (25°C and 700 mm Hg) and plotted on Figures B.4 and B.5 respectively.

Table B.1 : Properties For Critical Flow At 300 K.

Gas	Specific heat ratio γ	P^*/P_{up}	P_{up} for $P^* = 1$ atm
Air	1.400	0.528	1.893
Methane	1.299	0.546	1.832
Propane	1.126	0.579	1.726

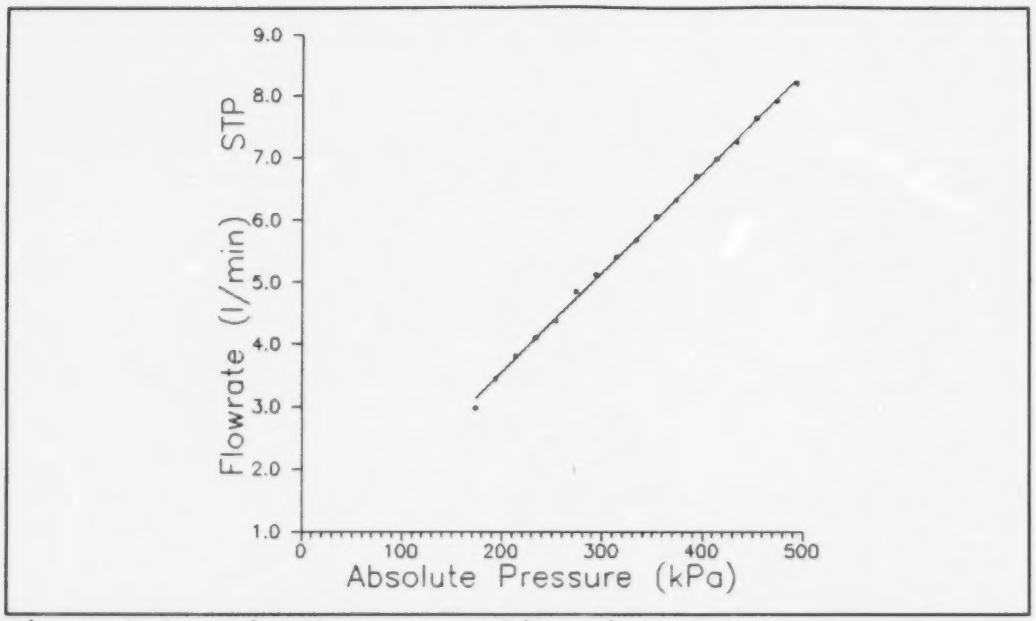

Figure B.2 : Air Flow Rate Calibration.
(Y = 0.0160206 * X + 0.341594)

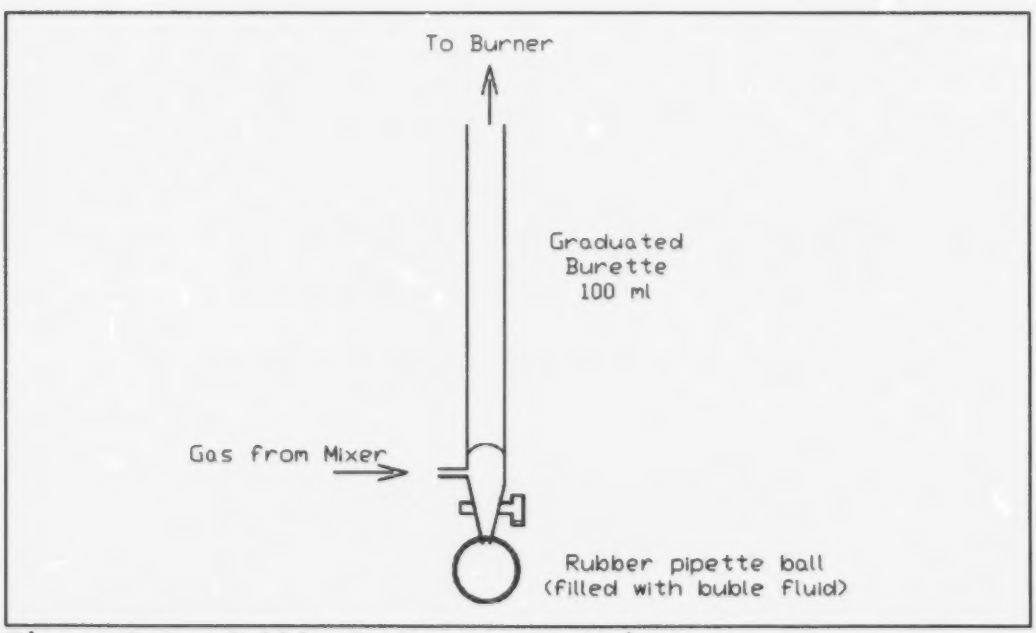

Figure B.3 : Bubble In Burette Technique.

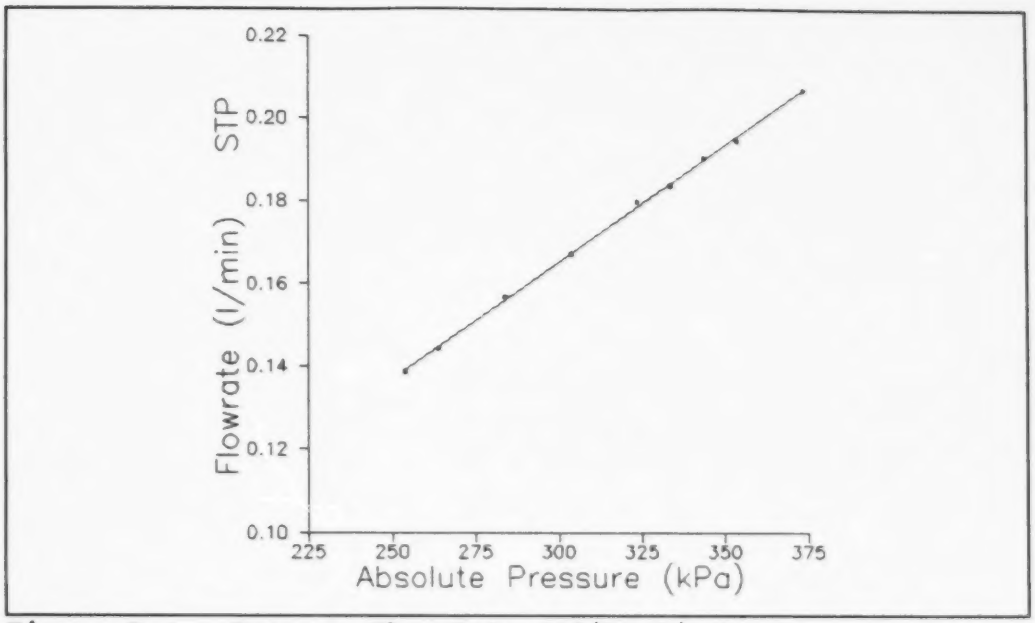

Figure B.4 : Propane Flow Rate Calibration.
(Y = 0.0005664 * X - 0.004684)

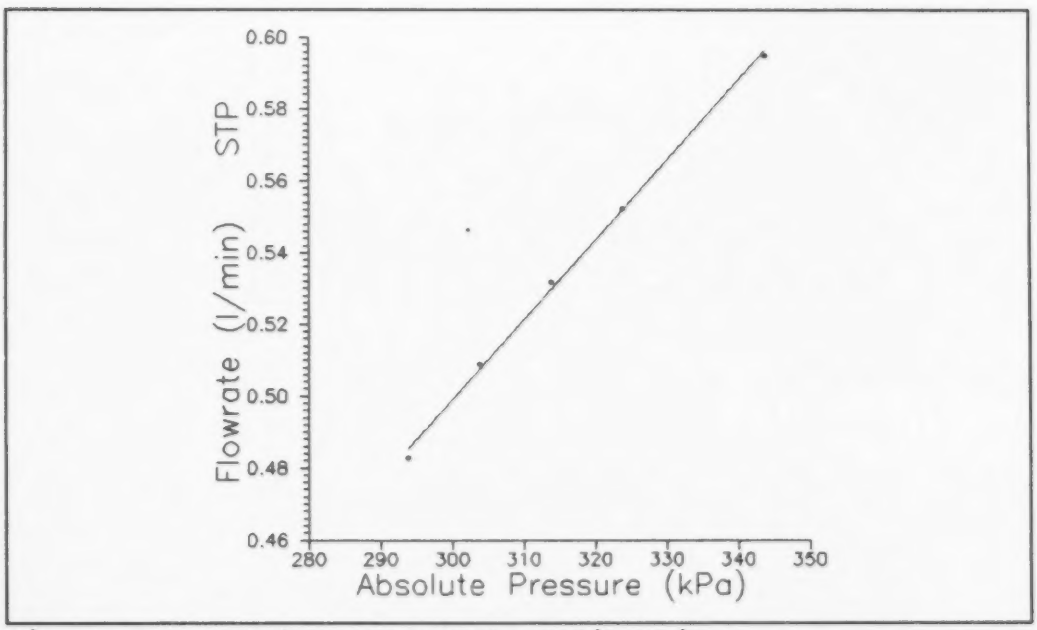

Figure B.5 : Methane Flow Rate Calibration.
(Y = 0.002223 * X - 0.1679)

Mixer1.bas and Mixer2.bas listed here are the two programs used for tabulating the A/F (Air to Fuel) ratios for the choked flow method based on the calibrated flow rates. Mixer1.bas tabulates air supply pressure for the corresponding equivalence ratio. Mixer2.bas tabulates the results in term of A/F ratio on mass basic. The calibration results are listed in Tables B.1, B.2, B.3 and B.4.

Reference

[WS78] G.J. van Wylen and R.E. Sonntag, Foundamentals of Classical Thermodynamics, SI Version 2ᵉ, John Wiley & Sons, 1978

```
'     Mixer1.bas
'     Sep 1990          DSK Ting
' This program tabulates A/F ratios for the gas mixer based on the calibrated
' flowrates. (Based on the original Fortran Program by B. McDonell)
      DIM phi(11), Qair(20), AirP(20), Barom(10)
      OPEN "c:\qb\ting\data.dat" FOR OUTPUT AS #1
      PRINT #1, "          Table A.1 : Table of Methane Equivalence Ratios"
      PRINT #1,
      PRINT #1, "          Methane supply pressure setting at 220 kPa"
      PRINT #1,
      PRINT #1, "          Stoichiometric A/F = 17.19 (mass basic)"
      PRINT #1,
' Range of barometric pressures to be considered:
      PRINT #1, "          Barometer:"
      PRINT #1, "          (mmHg)";
      FOR i = 1 TO 9
            Barom(i) = 680! + 5 * (i - 1)
            PRINT #1, USING "######"; Barom(i);
      NEXT i
      PRINT #1, : PRINT #1,
      PRINT #1, "          Equiv ratio         AIR supply pressure setting (kPag) :"
' Range of equivalence ratios to be considered:
      FOR i = 1 TO 11
            phi(i) = .5 + (i - 1) * .05
      NEXT i
' Calculate air pressures for methane using Aug 1990 calibration data
' Stoichiometric A/F ratio (volume basic) for methane
      AFstoi = 9.52
      FOR i = 1 TO 11
            PRINT #1,
            PRINT #1, "          ";
            PRINT #1, USING "####.##"; phi(i);
            FOR j = 1 TO 9
                  QCH4 = .00222284# * (220 + .133322 * Barom(j)) - .167852
                  Qair(j) = (AFstoi * QCH4) / phi(i)
                  AirP(j) = (Qair(j) + .006) / .019682 - (Barom(j) * .133322)
                  PRINT #1, USING "####.#"; AirP(j);
            NEXT j
      NEXT i
' Propane table:
      PRINT #1, : PRINT #1, : PRINT #1,
      PRINT #1, : PRINT #1, : PRINT #1,
      PRINT #1, "          Table A.2 : Table of Propane Equivalence Ratios"
      PRINT #1,
      PRINT #1, "          Propane supply pressure setting at 220 kPa"
      PRINT #1,
      PRINT #1, "          Stoichiometric A/F = 15.64 (mass basic)"
      PRINT #1,
      PRINT #1, "          Barometer:"
      PRINT #1, "          (mmHg)";
      FOR i = 1 TO 9
            PRINT #1, USING "######"; Barom(i);
      NEXT i
      PRINT #1, : PRINT #1,
      PRINT #1, "          Equiv ratio         AIR supply pressure setting (kPag) :"
' Calculate air pressures for propane using Aug 1990 calibration data
' Stoichiometric A/F ratio (volume basic) for propane
      AFstoi = 23.8
      FOR i = 1 TO 11
            PRINT #1; PRINT #1, "          ";
            PRINT #1, USING "####.##"; phi(i);
            FOR j = 1 TO 9
                  QC3H8 = .000566388# * (220 + .133322 * Barom(j)) - .00468412#
                  Qair(j) = (AFstoi * QC3H8) / phi(i)
                  AirP(j) = (Qair(j) + .006) / .019682 - (Barom(j) * .133322)
                  PRINT #1, USING "####.#"; AirP(j);
            NEXT j
      NEXT i
END
```

```
'     Mixer2.bas
'     Sep 1990          DSK Ting
' This program tabulates A/F ratios for the gas mixer base on the calibrated
' flowrates. (Based on the original Fortran Program by B. McDonell)
      DIM AF(27), Qair(20), AirP(20), Barom(10)
      OPEN "c:\qb\ting\data.dat" FOR OUTPUT AS #1
      PRINT #1, "          Table A.3 : Table of Methane A/F Ratios"
      PRINT #1,
      PRINT #1, "          Methane supply pressure setting at 220 kPa"
      PRINT #1,
      PRINT #1, "          Stoichiometric A/F = 17.19 (mass basic)"
      PRINT #1,
' Range of barometer pressures to be considered:
      PRINT #1, "          Barometer:"
      PRINT #1, "          (mmHg)";
      FOR i = 1 TO 9
            Barom(i) = 680! + 5 * (i - 1)
            PRINT #1, USING "######"; Barom(i);
      NEXT i
      PRINT #1, : PRINT #1,
' Range of A/F ratios to be considered:
      PRINT #1, "          A/F ratio           Air supply pressure setting (kPag)"
      AF(1) = 17.2
      FOR i = 2 TO 27
            AF(i) = 17! + (i - 1) * .5
      NEXT i
' Calculate air pressure for methane using Aug 1990 calibration data
      FOR i = 1 TO 27
            PRINT #1; PRINT #1, "           ";
            PRINT #1, USING "####.#"; AF(i);
            FOR j = 1 TO 9
                  QCH4 = .00222284# * (220 + .133322 * Barom(j)) - .167852
                  Qair(j) = AF(i) * (16.04 / 28.97) * QCH4
                  AirP(j) = (Qair(j) + .006) / .019682 - (Barom(j) * .133322)
                  PRINT #1, USING "####.#"; AirP(j);
            NEXT j
      NEXT i
' Propane table
      PRINT #1; PRINT #1,
      PRINT #1, "          Table A.4 : Table of Propane A/F Ratios"
      PRINT #1,
      PRINT #1, "          Propane supply pressure setting at 220 kPa"
      PRINT #1,
      PRINT #1, "          Stoichiometric A/F = 15.64 (mass basic)"
      PRINT #1,
' Range of barometer pressures to be considered:
      PRINT #1, "          Barometer:"; PRINT #1, "          (mmHg)";
      FOR i = 1 TO 9
            PRINT #1, USING "######"; Barom(i);
      NEXT i
      PRINT #1, : PRINT #1,
' Range of A/F ratios to be considered:
      PRINT #1, "          A/F ratio           Air supply pressure setting (kPag)"
      AF(1) = 15.64
      FOR i = 2 TO 27
            AF(i) = 16! + (i - 1) * .5
      NEXT i
' Calculate air pressure for methane using Aug 1990 calibration data
      FOR i = 1 TO 27
            PRINT #1, PRINT #1, "           ";
            PRINT #1, USING "####.#"; AF(i);
            FOR j = 1 TO 9
                  QC3H8 = .000566388# * (220 + .133322 * Barom(j)) - .00468412#
                  Qair(j) = AF(i) * (44.097 / 28.97) * QC3H8
                  AirP(j) = (Qair(j) + .006) / .019682 - (Barom(j) * .133322)
                  PRINT #1, USING "####.#"; AirP(j);
            NEXT j
      NEXT i
END
```

Table B.1 : Table of Methane Equivalence Ratios.

Methane supply pressure setting at 220 kPa

Stoichiometric A/F = 17.19 (mass basic)

Barometer: (mmHg)	680	685	690	695	700	705	710	715	720
Equiv ratio	AIR supply pressure setting (kPag) :								
0.50	415.3	416.1	416.8	417.6	418.4	419.1	419.9	420.7	421.4
0.55	369.3	370.0	370.6	371.2	371.9	372.5	373.1	373.8	374.4
0.60	331.0	331.5	332.1	332.6	333.1	333.7	334.2	334.7	335.2
0.65	298.6	299.0	299.5	299.9	300.3	300.8	301.2	301.7	302.1
0.70	270.8	271.2	271.5	271.9	272.2	272.6	273.0	273.3	273.7
0.75	246.7	247.0	247.3	247.6	247.9	248.2	248.5	248.8	249.1
0.80	225.7	225.9	226.1	226.4	226.6	226.8	227.0	227.3	227.5
0.85	207.1	207.3	207.4	207.6	207.8	208.0	208.1	208.3	208.5
0.90	190.6	190.7	190.8	190.9	191.1	191.2	191.3	191.5	191.6
0.95	175.8	175.9	175.9	176.0	176.1	176.2	176.3	176.4	176.5
1.00	162.5	162.5	162.6	162.6	162.7	162.7	162.8	162.8	162.9

Table B.2 : Table of Propane Equivalence Ratios.

Propane supply pressure setting at 220 kPa

Stoichiometric A/F = 15.64 (mass basic)

Barometer: (mmHg)	680	685	690	695	700	705	710	715	720
Equiv ratio	AIR supply pressure setting (kPag) :								
0.50	323.9	324.1	324.3	324.6	324.8	325.1	325.3	325.6	325.8
0.55	286.2	286.4	286.5	286.7	286.9	287.0	287.2	287.3	287.5
0.60	254.8	254.9	255.0	255.1	255.2	255.3	255.4	255.5	255.6
0.65	228.3	228.3	228.3	228.4	228.4	228.4	228.5	228.5	228.6
0.70	205.5	205.5	205.5	205.5	205.5	205.4	205.4	205.4	205.4
0.75	185.8	185.7	185.7	185.6	185.6	185.5	185.4	185.4	185.3
0.80	168.5	168.4	168.3	168.2	168.1	168.0	167.9	167.9	167.8
0.85	153.3	153.2	153.0	152.9	152.8	152.6	152.5	152.4	152.3
0.90	139.8	139.6	139.4	139.3	139.1	139.0	138.8	138.6	138.5
0.95	127.6	127.5	127.3	127.1	126.9	126.7	126.5	126.3	126.2
1.00	116.7	116.5	116.3	116.1	115.9	115.7	115.5	115.3	115.1

Table B.3 : Table of Methane A/F Ratios.
Methane supply pressure setting at 220 kPa
Stoichiometric A/F = 17.19 (mass basic)
Barometer:

(mmHg)	680	685	690	695	700	705	710	715	720
A/F ratio	Air supply pressure setting (kPag)								
17.2	162.6	162.6	162.7	162.7	162.8	162.8	162.9	162.9	163.0
17.5	167.0	167.0	167.1	167.2	167.2	167.3	167.3	167.4	167.5
18.0	174.3	174.4	174.5	174.6	174.7	174.7	174.8	174.9	175.0
18.5	181.7	181.8	181.9	182.0	182.1	182.2	182.3	182.4	182.5
19.0	189.0	189.1	189.3	189.4	189.5	189.6	189.8	189.9	190.0
19.5	196.4	196.5	196.7	196.8	197.0	197.1	197.2	197.4	197.5
20.0	203.7	203.9	204.1	204.2	204.4	204.6	204.7	204.9	205.1
20.5	211.1	211.3	211.5	211.6	211.8	212.0	212.2	212.4	212.6
21.0	218.4	218.6	218.8	219.1	219.3	219.5	219.7	219.9	220.1
21.5	225.8	226.0	226.2	226.5	226.7	226.9	227.2	227.4	227.6
22.0	233.1	233.4	233.6	233.9	234.1	234.4	234.6	234.9	235.1
22.5	240.5	240.8	241.0	241.3	241.6	241.8	242.1	242.4	242.7
23.0	247.8	248.1	248.4	248.7	249.0	249.3	249.6	249.9	250.2
23.5	255.2	255.5	255.8	256.1	256.4	256.8	257.1	257.4	257.7
24.0	262.5	262.9	263.2	263.5	263.9	264.2	264.5	264.9	265.2
24.5	269.9	270.2	270.6	271.0	271.3	271.7	272.0	272.4	272.7
25.0	277.2	277.6	278.0	278.4	278.7	279.1	279.5	279.9	280.2
25.5	284.6	285.0	285.4	285.8	286.2	286.6	287.0	287.4	287.8
26.0	291.9	292.4	292.8	293.2	293.6	294.0	294.5	294.9	295.3
26.5	299.3	299.7	300.2	300.6	301.1	301.5	301.9	302.4	302.8
27.0	306.7	307.1	307.6	308.0	308.5	308.9	309.4	309.9	310.3
27.5	314.0	314.5	315.0	315.4	315.9	316.4	316.9	317.4	317.8
28.0	321.4	321.9	322.4	322.9	323.4	323.9	324.4	324.9	325.4
28.5	328.7	329.2	329.8	330.3	330.8	331.3	331.8	332.4	332.9
29.0	336.1	336.6	337.1	337.7	338.2	338.8	339.3	339.9	340.4
29.5	343.4	344.0	344.5	345.1	345.7	346.2	346.8	347.4	347.9
30.0	350.8	351.3	351.9	352.5	353.1	353.7	354.3	354.9	355.4

Table B.4 : Table of Propane A/F Ratios.
Propane supply pressure setting at 220 kPa
Stoichiometric A/F = 15.64 (mass basic)
Barometer:

(mmHg)	680	685	690	695	700	705	710	715	720
A/F ratio	Air supply pressure setting (kPag)								
15.6	116.8	116.6	116.4	116.2	116.0	115.8	115.5	115.3	115.1
16.5	128.2	128.0	127.8	127.6	127.5	127.3	127.1	126.9	126.7
17.0	134.8	134.7	134.5	134.3	134.1	134.0	133.8	133.6	133.5
17.5	141.4	141.3	141.1	141.0	140.8	140.7	140.5	140.4	140.2
18.0	148.1	147.9	147.8	147.6	147.5	147.4	147.2	147.1	146.9
18.5	154.7	154.6	154.4	154.3	154.2	154.1	153.9	153.8	153.7
19.0	161.3	161.2	161.1	161.0	160.9	160.8	160.6	160.5	160.4
19.5	167.9	167.8	167.7	167.6	167.5	167.4	167.4	167.3	167.2
20.0	174.6	174.5	174.4	174.3	174.2	174.1	174.1	174.0	173.9
20.5	181.2	181.1	181.0	181.0	180.9	180.8	180.8	180.7	180.6
21.0	187.8	187.7	187.7	187.6	187.6	187.5	187.5	187.4	187.4
21.5	194.4	194.4	194.3	194.3	194.3	194.2	194.2	194.2	194.1
22.0	201.0	201.0	201.0	201.0	201.0	200.9	200.9	200.9	200.9
22.5	207.7	207.7	207.7	207.6	207.6	207.6	207.6	207.6	207.6
23.0	214.3	214.3	214.3	214.3	214.3	214.3	214.3	214.3	214.3
23.5	220.9	220.9	221.0	221.0	221.0	221.0	221.0	221.1	221.1
24.0	227.5	227.6	227.6	227.6	227.7	227.7	227.7	227.8	227.8
24.5	234.2	234.2	234.3	234.3	234.4	234.4	234.5	234.5	234.6
25.0	240.8	240.8	240.9	241.0	241.0	241.1	241.2	241.2	241.3
25.5	247.4	247.5	247.6	247.6	247.7	247.8	247.9	248.0	248.0
26.0	254.0	254.1	254.2	254.3	254.4	254.5	254.6	254.7	254.8
26.5	260.7	260.8	260.9	261.0	261.1	261.2	261.3	261.4	261.5
27.0	267.3	267.4	267.5	267.6	267.8	267.9	268.0	268.1	268.3
27.5	273.9	274.0	274.2	274.3	274.4	274.6	274.7	274.9	275.0
28.0	280.5	280.7	280.8	281.0	281.1	281.3	281.4	281.6	281.7
28.5	287.1	287.3	287.5	287.6	287.8	288.0	288.1	288.3	288.5
29.0	293.8	293.9	294.1	294.3	294.5	294.7	294.8	295.0	295.2

Appendix C : Flame Area Finding Algorithm

This appendix describes the flame area finding algorithm in the image processing program called FLASH.

The algorithm is :

1) The user selects the centre of the flame, which becomes an origin for the polar coordinate system used in finding the flame edge.

2) A vertical distance is marked off between features with a known distance apart to obtain a calibration for the area of each pixel in mm^2. The distance between the spark electrodes and the ionization probe (40 mm) was used throughout this study. The horizontal calibration factor of the pixel dimension is 4/3 * 480/512 of the vertical calibration factor because of the characteristics of the television screen and the video digitizing hardware.

3) The user then marks the outside limit of the flame edge by dragging the circumference of a circle from the centre of the flame. The program assumes that the flame edge is within this limit.

4) A set of rays of the image are extracted using the user defined origin, and going from the circle circumference towards the centre of the flame. The rays are taken in a counter-clockwise direction from $\theta = 0$. The angle increment is fixed at 0.05 radians.

5) In each ray, the edge is found by looking for a large negative value in the derivative of the ray. The initial value to look

for is arbitrarily set at -5.5. If the initial value of -5.5 is not found, the criterion value will be decreased by 0.5 (adding 0.5 to the previous value), and the search is made again until a match is found.

6) The edge on each ray is saved for later use.

7) When all rays have been covered, the edge points are joined by straight lines and the screen is wiped blank outside the line (flame area).

8) The pixels inside the line (flame area) are then counted, and their number multiplied by the calibration constant to give the actual area.

The present flame area finding algorithm tends to detect an edge outside the actual flame edge. This larger flame edge leads to a larger flame area calculated.

Appendix D : Spark Ignition Results

This appendix covers the ignition spark in room air tests. The high capacitance ignition system was tested in quiescent air in the combustion chamber prior to any experimental runs.

The purpose of the tests was to study the effects of spark gap and stored energy on the actual energy transferred across the spark gap. Two sets of tests were conducted. The first set of tests was carried out with fixed voltage (500 V) and capacitance (2.5 μF), while varying the spark gap from 1 to 4.5 mm. The second set of tests was conducted with fixed spark gap of 4.5 mm and fixed capacitance of 2.5 μF while varying the voltage from 300 to 600 V.

Figure D.1 shows the sketches of the effect of spark gap on the spark. Each of the sketches illustrates the average of five runs. The maximum deviation of gap energy illusrated by the area under the plot was found to be less than 20%.

A summary results of the spark gap effects on spark energy are tabulated in Table D.1. The energy efficiency is defined as the fraction of the stored energy crossing the spark gap.

Results in Table D.1 are plotted in Figure D.2. This figure shows that the energy efficiency increases while the discharge duration decreases, with increasing spark gap. With an input energy of 312.5 mJ (500 V, 2.5 μF), the energy efficiency maximized at the 4.50 mm spark gap over the range of spark gap tested. Hence, a spark gap of 4.50 mm was used throughout this study. This energy efficiency is expected to decrease with further increase in spark gap.

Figure D.3 shows the effect of stored voltage on the spark. The spark gap and the capacitance were fixed at 4.50 mm and 2.5 μF respectively. Each sketch illustrates the average of five runs. The deviation of gap energy (area under the plot) for each run was found to be less than 20% from the average. The effects of input voltage on spark energy were summarized in Table D.2.

From Table D.2, with a fixed spark gap of 4.50 mm and a fixed capacitance of 2.5 μF, both energy efficiency and spark discharge duration increase with increasing stored voltage and energy. This is illustrated in Figure D.4. The discharge duration doubled from 0.5 ms to 1 ms and the energy efficiency increased from 2.2% to 7.6%, as the input energy tripled from 113 mJ to 450 mJ. Since the capacitance ignition system was designed for a maximum input energy of 300 mJ, an input energy of 312.5 mJ (500 V and 2.5 μF) was used. Further increase of input voltage or energy may result in auto-spark. In fact, auto-sparking occurred when increasing the input voltage above 1000 V with a 1 mm spark gap. Under auto-sparking condition, the voltage is expected to be high enough to ionize the spark gap prior to triggering.

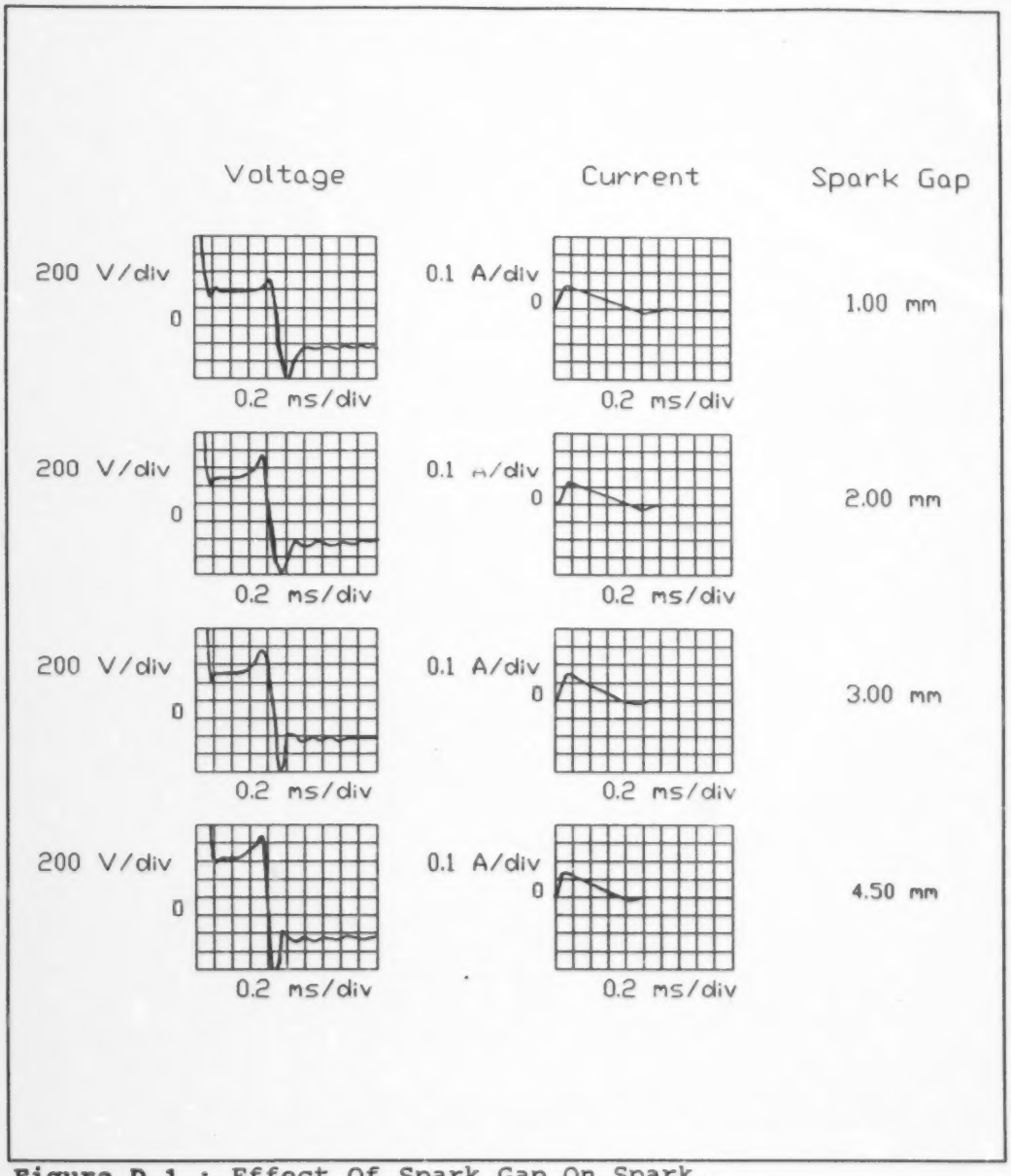

Figure D.1 : Effect Of Spark Gap On Spark.
(Input Energy = 312.5 mJ, 500 V, 2.5 μF)

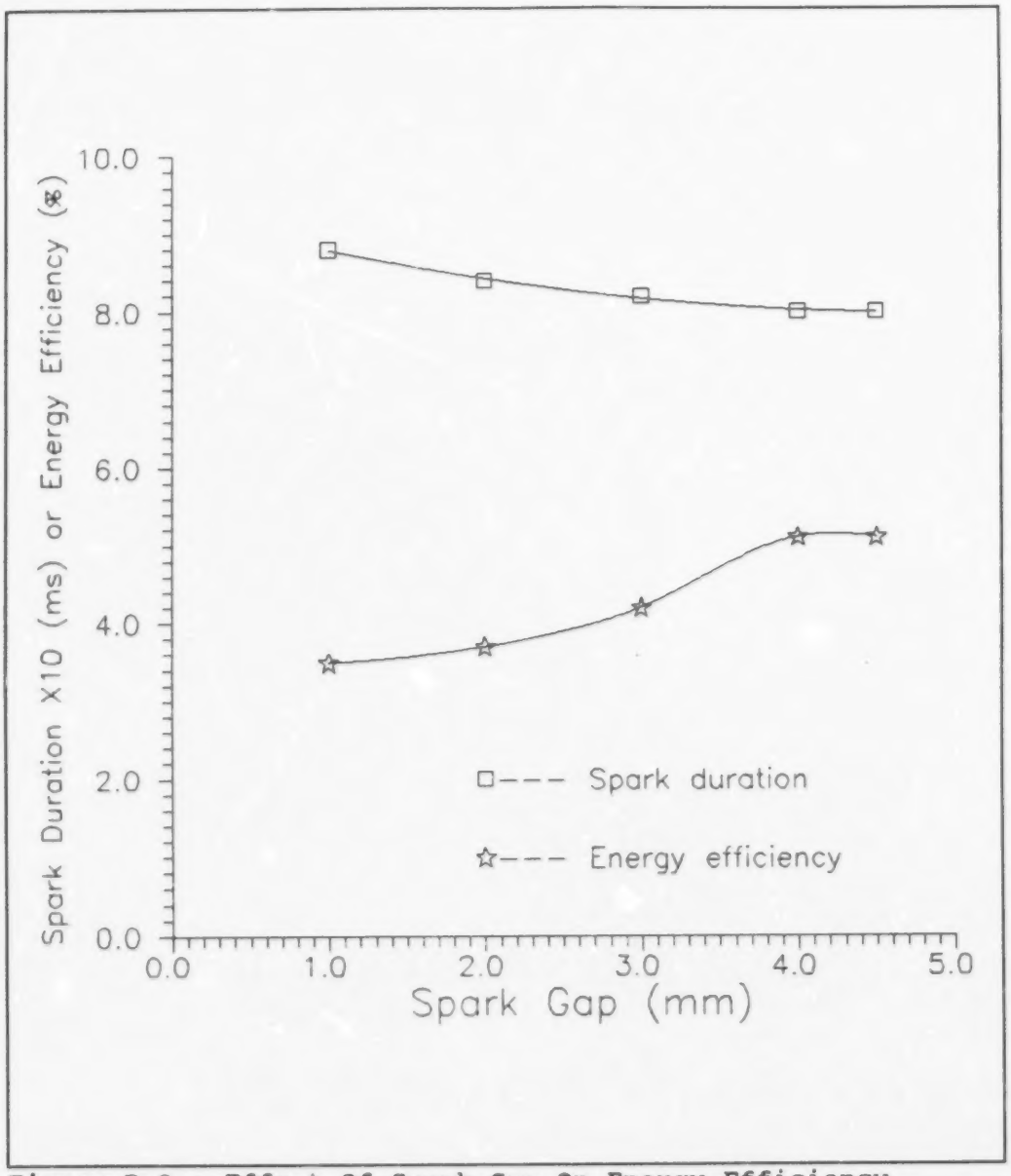

Figure D.2 : Effect Of Spark Gap On Energy Efficiency.
(Input Energy = 312.5 mJ, 500 V, 2.5 μF)

Table D.1 : Effect Of Spark Gap On Energy Efficiency.
(Input Energy = 312.5 mJ, 500 V, 2.5 μF)

Spark Gap (mm)	Voltage Discharge Duration (ms)	Output Energy VIt (mJ)	Average Output Power (W)	Energy Efficiency (%)
1.00	0.88	10.8	13	3.5
2.00	0.84	11.7	15	3.7
3.00	0.82	13.2	17	4.2
4.00	0.80	15.8	21	5.1
4.50	0.80	16.0	21	5.1

Table D.2 : Effect Of Stored Voltage (Input Energy) On Energy Efficiency. (Spark Gap = 4.50 mm, 2.5 μF)

Voltage Discharge Duration (ms)	Stored Voltage (V)	Input Energy $\frac{1}{2}CV^2$ (mJ)	Output Energy VIt (mJ)	Average Output Power (W)	Energy Efficiency (%)
0.52	300	112.5	2.5	5	2.2
0.66	400	200.0	5.5	9	2.8
0.86	500	312.5	15.5	19	5.0
1.00	600	450.0	34.0	35	7.6

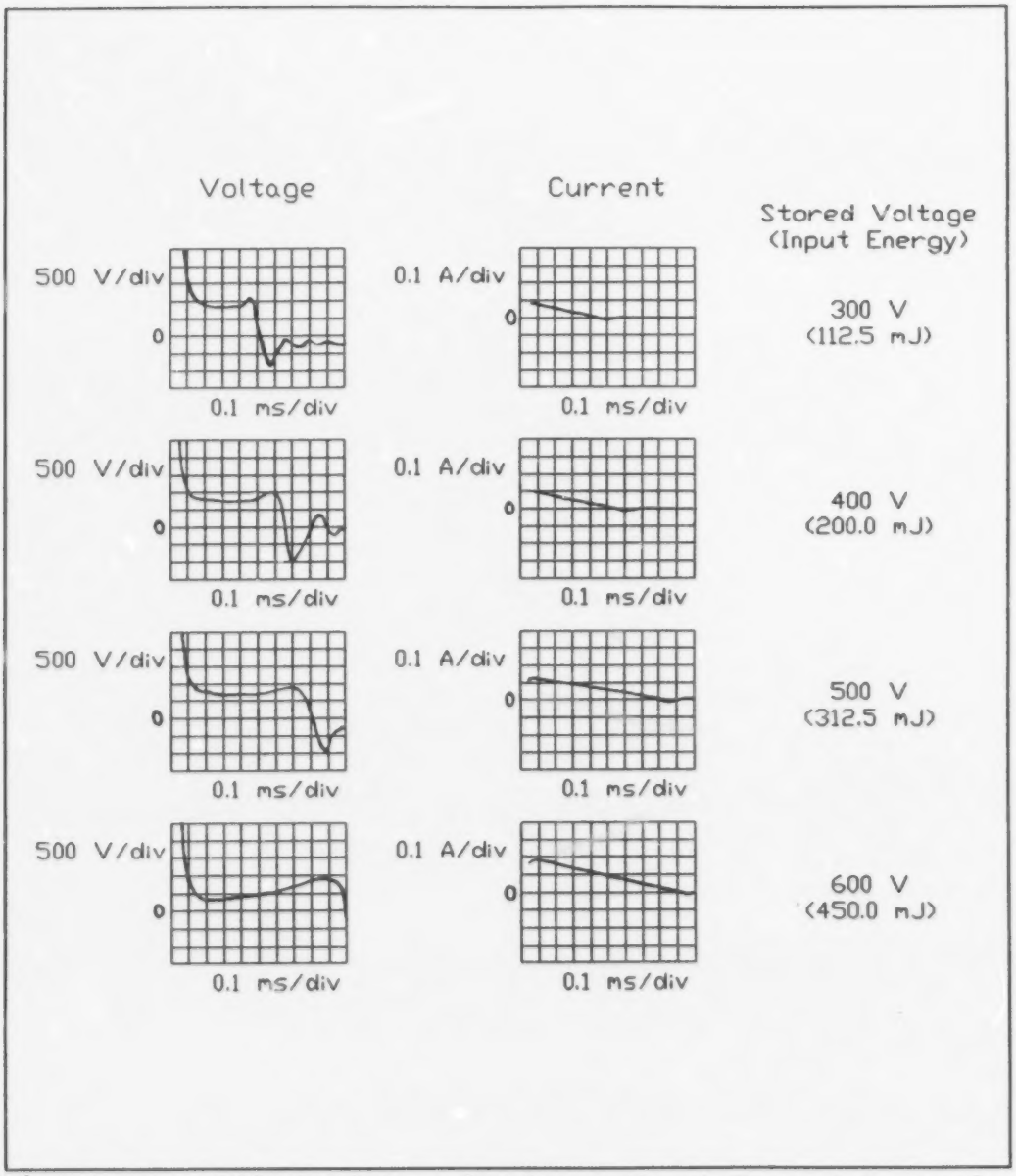

Figure D.3 : Effect Of Stored Voltage (Input Energy) On Spark. (Spark Gap = 4.50 mm, 2.5 μF)

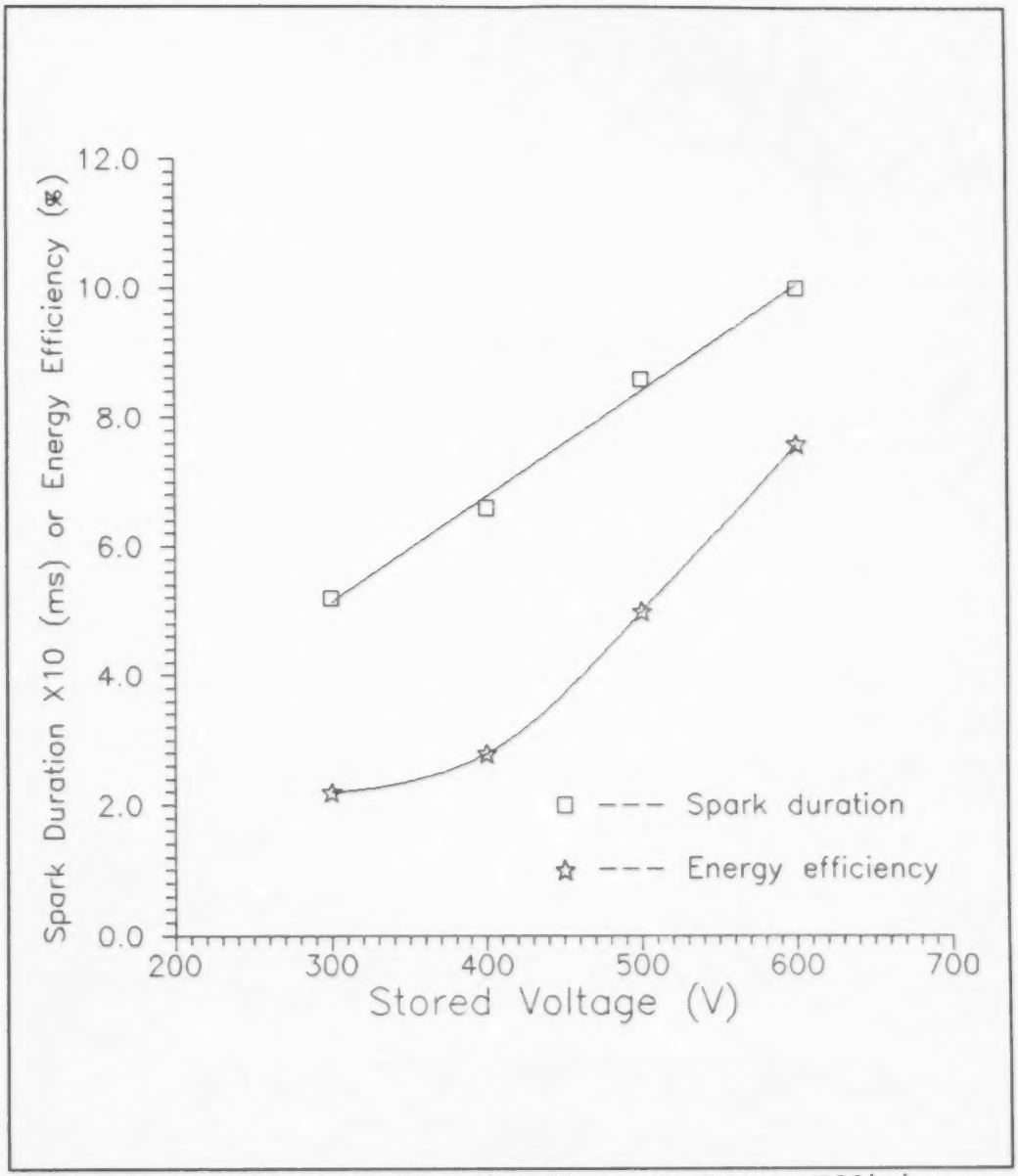

Figure D.4 : Effect Of Stored Voltage On Energy Efficiency. (Spark Gap = 4.50 mm, 2.5 μF)

Appendix E : Gas Chromatograph

This appendix details the calibrations and measurements of gas compositions with the gas chromatograph (Model P 200 manufactured by MTI). This section includes the analyses of the dry air supply, methane supply and natural propane supply.

The important features of this gas chromatograph analysis procedure are the choice of column and the "method". A method consists of

a) carrier gas (He)

b) carrier gas flowrate (set by carrier gas pressure)

c) column temperature

d) conductivity sensor sensitivity

The methods used in this study are as described in Table E.1. Method PropL.Met, used for checking the purity of the supply gases, is attached at the end of this appendix. The methods used for analyzing the hydrocarbon-air mixtures throughout this study are listed as Meth.Met and Prop.Met. Meth.Met method was used for analyzing methane-air mixtures while Prop.Met method was used for analyzing propane-air mixtures. Lower temperatures and pressures were used in Meth.Met and Prop.Met methods in order to separate air from methane in column B. Moreover, with the use of these lower temperatures and pressures, better separations between different compounds were achieved, as no major heavy hydrocarbon were present in any of the supply gases.

The sequence in which the hydrocarbons elute, as taken from a Hewlett Packard publication [HP89], is tabulated in Table E.2, with

their relative response factors taken from Dietz [Di67]. The relative response factor is defined as the relative ratio of signal-to-sample size. The calculated areas are divided by these relative response factors to give the actual relative areas.

Figure E.1 shows the actual chromatogram from channel A (Mol Sieve 5A column) of the extra dry air supply from new cylinder. Note that the method setting for channel A was always the same for all the methods involved in this study. This was because only oxygen, nitrogen and methane were analyzed using this column. The original cylinder of extra dry air supply had a low proportion of oxygen (oxygen plus argon to air ratio was 0.207 compared with 0.218 for normal air), hence it was not used. Since oxygen and argon did not separate in this column, it was assumed that the oxygen to oxygen plus argon ratio was 20.8 to 21.8. Table E.3 shows the actual result after taking the different relative response factors into account.

Figure E.2 is the gas chromatogram of the same extra dry air sample analyzed by channel B (Pora Plot Q column) using the method called PropL.Met. Note that channel B did not separate nitrogen from oxygen and argon. With all the methods used throughout this study, air elutes as a single gas from column B.

Figures E.3 and E.4 show channel A and channel B chromatograms from the analysis of the methane supply (using PropL.Met) respectively. This method can elute compounds as heavy as i-Pentane out of channel B. This high temperature method was used for channel B (air and methane were not separated in column B) in order to ensure

that all possible hydrocarbons present would elute within the elution time given. The actual location of each compound was determined by running a calibration gas using the same method. The calibration gas used was ASTM Blend BL 5244 from Matheson which consisted of the compounds listed in Table E.4.

The actual result of the calibration gas analysis is tabulated in Table E.5. Note that hydrocarbons heavier than methane did not elute from column A.

Figure E.5 shows the chromatogram of channel B obtained by analyzing the natural propane supply using PropL.Met. It is obvious that this propane supply was not of very high purity. Table E.6 shows the actual results obtained from analyzing the propane supply using both column A and column B.

Table E.1 : Method Description.

Method	Description
PropL.Met	for checking purity of the supply gas
Meth.Met	for analyzing Methane-Air Mixtures
Prop.Met	for analyzing Propane-Air Mixtures

Table E.2 : Elution Sequence Of Hydrocarbons In Refinery Gas.

Hydrocarbon	Relative Response Factor
1) Methane	35.7
2) Ethylene	48
3) Ethane	51.2
4) Propylene	64.5
5) Propane	64.5
6) i-Butane	82
7) Butene-1	81
8) n-Butane	85
9) t-Butene-2	85
10) c-Butene-2	87
11) i-Pentane	102
12) n-Pentane	105

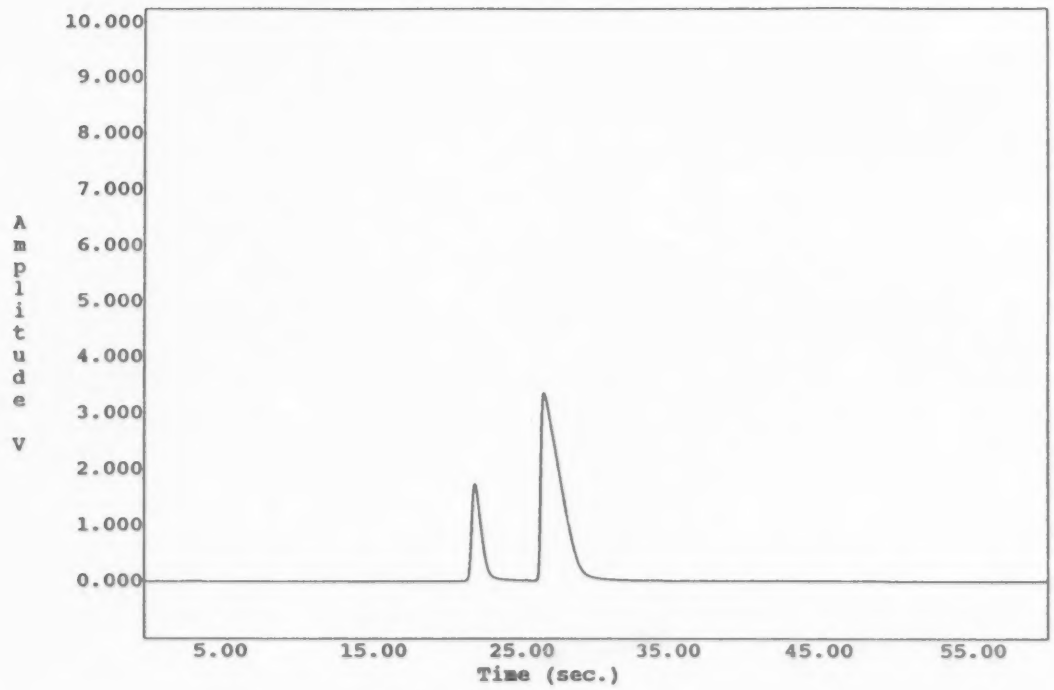

Channel: A
Current Time: Jan 20, 1992 14:33:02
Method: b:\propl.met
File : b:\air2.dat
Data file creation time:
Instrument ID:
Column Type:
Carrier Gas:
Column Head Pressure: 12.0
Column Temperature: 50 C
Instrument Gain: LOW
Sample Time: 5 seconds
Inject Time: 40 milliseconds
Run Time: 60 seconds

Figure E.1 : Extra Dry Air Supply From Column A

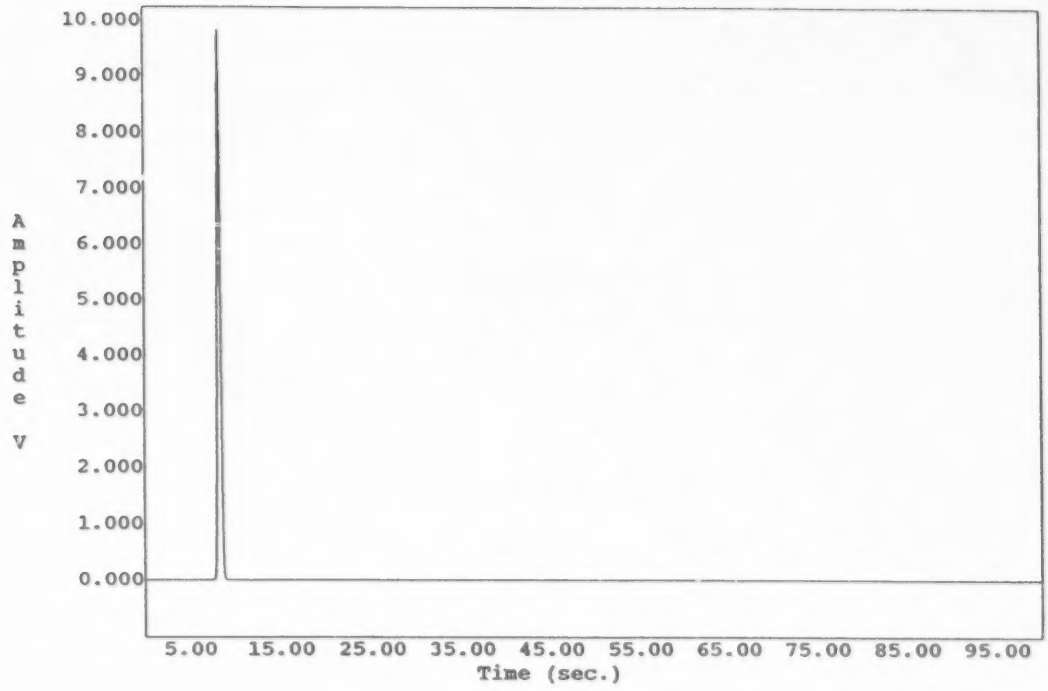

Channel: B
Current Time: Jan 20, 1992 14:35:35
Method: b:\propl.met
File : b:\air2.dat
Data file creation time:
Instrument ID:
Column Type:
Carrier Gas:
Column Head Pressure: 10.4
Column Temperature: 115 C
Instrument Gain: LOW
Sample Time: 5 seconds
Inject Time: 30 milliseconds
Run Time: 100 seconds

Figure E.2 : Extra Dry Air Supply From Column B

Table E.3 : Composition Of Extra Dry Air Supply Used In This Study.

Compound	Concentration (% by Volume)
oxygen (+ Argon)	21.6
nitrogen	78.4

Table E.4 : Composition Of Calibration Gas (ASTM Blend BL 5244).

Compound	Concentration (% volume)
Ethane	4.00
Propylene	4.00
Propane	87.00
i-Butane	3.00
n-Butane	1.00
i-Pentane	1.00

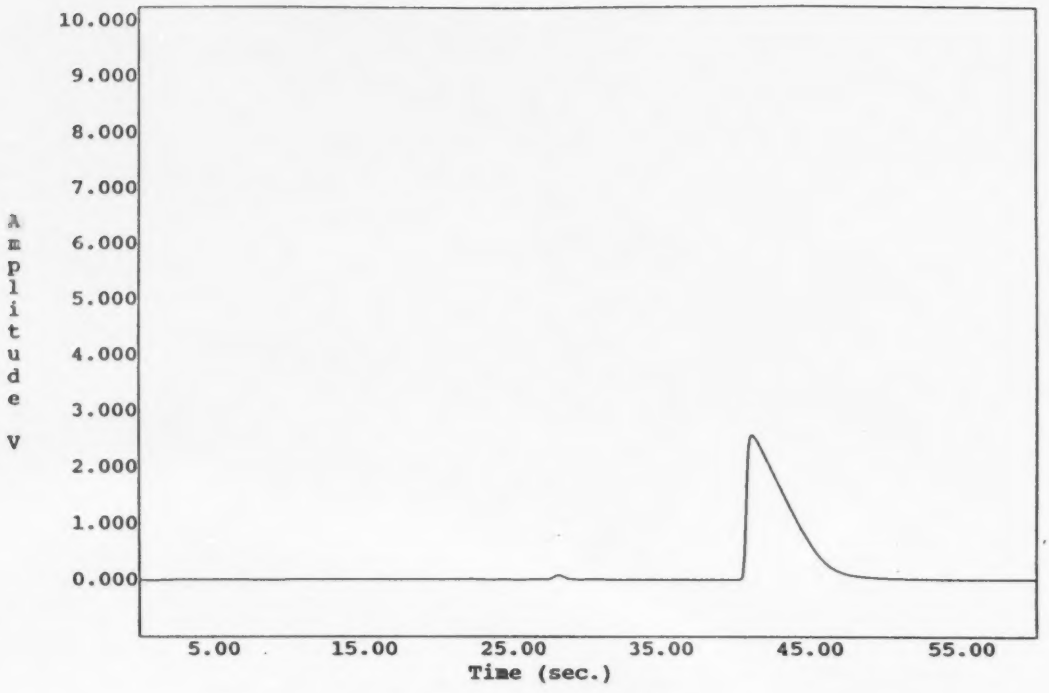

Channel: A
Current Time: Jan 20, 1992 14:59:08
Method: b:\meth.met
File : b:\meth1.dat
Data file creation time:
Instrument ID:
Column Type:
Carrier Gas:
Column Head Pressure: 11.9
Column Temperature: 49 C
Instrument Gain: LOW
Sample Time: 5 seconds
Inject Time: 40 milliseconds
Run Time: 60 seconds

Figure E.3 : Methane Supply From Column A

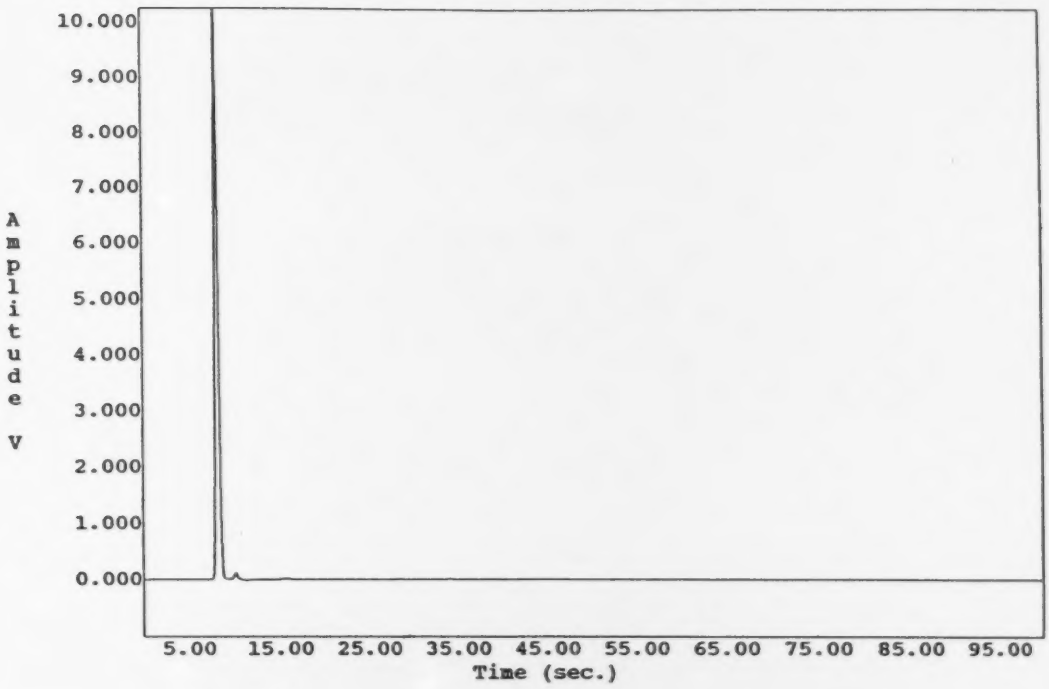

Channel: B
Current Time: Jan 20, 1992 14:58:27
Method: b:\meth.met
File : b:\meth1.dat
Data file creation time:
Instrument ID:
Column Type:
Carrier Gas:
Column Head Pressure: 10.3
Column Temperature: 114 C
Instrument Gain: LOW
Sample Time: 5 seconds
Inject Time: 30 milliseconds
Run Time: 100 seconds

Figure E.4 : Methane Supply From Column B

Table E.5 : Composition Of Methane Supply.

Compound	Concentration (% volume)
nitrogen	1.0
methane	98.3
ethane	0.7

Table E.6 : Composition Of Propane Supply.

Compound	Concentration (% volume)
methane (+ nitrogen/air)	0.8
ethylene	4.3
ethane	0.3
propane (+ propylene)	94.2
i-Butane	0.4

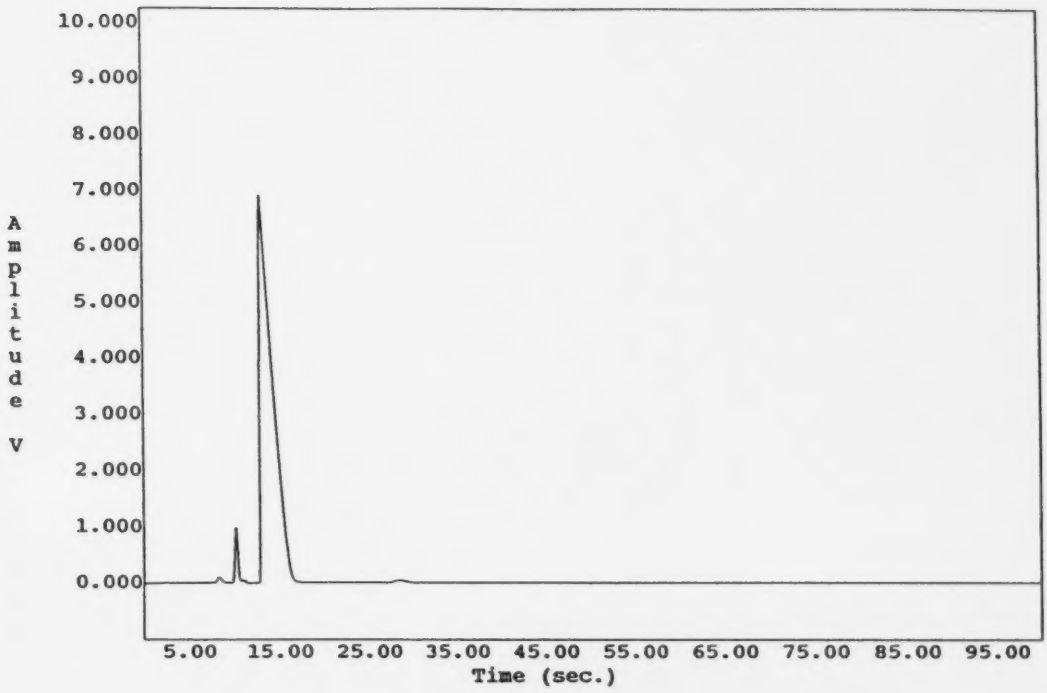

Channel: B
Current Time: Jan 20, 1992 14:49:53
Method: b:\prop.met
File : b:\prop2.dat
Data file creation time:
Instrument ID:
Column Type:
Carrier Gas:
Column Head Pressure: 10.4
Column Temperature: 114 C
Instrument Gain: LOW
Sample Time: 5 seconds
Inject Time: 30 milliseconds
Run Time: 100 seconds

Figure E.5 : Natural Propane Supply From Column B

PropL.Met

Jan 20 1992 14:34:09
Method : propl.met
Channel : A

Instrument Setup

Column temperature (C) : 50
Run Time (sec) : 60
Sample Time (sec) : 5.0
Inject Time (msec) : 40
Detector Filament : On
Detector Auto Zero : On
Detector Sensitivity : Low

Peak Table

Pkno Name RT RT Window Un BP Cal Level 1

Calibration Table

Level Area Concentration

Calibration Setup

Time Unit : SEC
Peak Attribute : AREA
Calibration Fit : POINT
Update Peak RT Time After Each Run : NO
Update Peak Retention Time After Calibration : YES
Number of Runs (A & B) : 1
Multiplication Factor : 1.000
Uncalibrated Peaks RF : 0.00000

Jan 20 1992 14:34:09
Method : propl.met
Channel : B

Instrument Setup

Column temperature (C) : 115
Run Time (sec) : 100
Sample Time (sec) : 5.0
Inject Time (msec) : 30
Detector Filament : On
Detector Auto Zero : On
Detector Sensitivity : Low

Peak Table

Pkno Name RT RT Window Un BP Cal Level 1

Calibration Table

Level Area Concentration

Calibration Setup

Time Unit : SEC
Peak Attribute : AREA
Calibration Fit : POINT
Update Peak RT Time After Each Run : NO
Update Peak Retention Time After Calibration : NO
Number of Runs (A & B) : 1
Multiplication Factor : 1.000
Uncalibrated Peaks RF : 0.00000

Meth.Met

Meth.Met

Channel : A

Instrument Setup

Column temperature (C)	: 50
Run Time (sec)	: 60
Sample Time (sec)	: 5.0
Inject Time (msec)	: 40
Detector Filament	: On
Detector Auto Zero	: On
Detector Sensitivity	: Low

Peak Table

Pkno	Name	RT	RT Window	Un	BP	Cal Level 1
1	Nitrogen	25.730	2.540	%		0.652
2	methane	42.020	8.910	%		97.500

Calibration Table

	Level	Area	Concentration
Nitrogen	1	4495312	0.652
methane	1	817761152	97.500

Calibration Setup

Time Unit	: SEC
Peak Attribute	: AREA
Calibration Fit	: POINT
Update Peak RT Time After Each Run	: NO
Update Peak Retention Time After Calibration	: YES
Number of Runs (A & B)	: 1
Multiplication Factor	: 1.000
Uncalibrated Peaks RF	: 0.00000

Channel : B

Instrument Setup

Column temperature (C)	: 35
Run Time (sec)	: 60
Sample Time (sec)	: 5.0
Inject Time (msec)	: 20
Detector Filament	: On
Detector Auto Zero	: On
Detector Sensitivity	: Low

Peak Table

Pkno	Name	RT	RT Window	Un	BP	Cal Level 1
1	n2/o2/air	7.310	0.890	%		1.000
2	methane	8.130	1.510	%		97.500
3	ethane	11.090	0.520	%		0.560
4	propane(propl)	21.410	1.540	%		0.768

Calibration Table

	Level	Area	Concentration
n2/o2/air	1	2267293	1.000
methane	1	367333184	97.500
ethane	1	161437	0.560
propane(propl)	1	3399988	0.768

Calibration Setup

Time Unit	: SEC
Peak Attribute	: AREA
Calibration Fit	: POINT
Update Peak RT Time After Each Run	: NO
Update Peak Retention Time After Calibration	: YES
Number of Runs (A & B)	: 1
Multiplication Factor	: 1.000
Uncalibrated Peaks RF	: 0.00000

Prop.Met

Jan 20 1992 14:49:04
Method : prop.met
Channel : A

Instrument Setup

Column temperature (C) : 50
Run Time (sec) : 60
Sample Time (sec) : 5.0
Inject Time (msec) : 40
Detector Filament : On
Detector Auto Zero : On
Detector Sensitivity : Low

Peak Table

Pkno	Name	RT	RT Window	Un	BP	Cal Level 1

Calibration Table

Level	Area	Concentration

Calibration Setup

Time Unit : SEC
Peak Attribute : AREA
Calibration Fit : POINT
Update Peak RT Time After Each Run : NO
Update Peak Retention Time After Calibration : YES
Number of Runs (A & B) : 1
Multiplication Factor : 1.000
Uncalibrated Peaks RF : 0.00000

Jan 20 1992 14:49:04
Method : prop.met
Channel : B

Instrument Setup

Column temperature (C) : 90
Run Time (sec) : 80
Sample Time (sec) : 5.0
Inject Time (msec) : 30
Detector Filament : On
Detector Auto Zero : On
Detector Sensitivity : Low

Peak Table

Pkno	Name	RT	RT Window	Un	BP	Cal Level 1

Calibration Table

Level	Area	Concentration

Calibration Setup

Time Unit : SEC
Peak Attribute : AREA
Calibration Fit : POINT
Update Peak RT Time After Each Run : NO
Update Peak Retention Time After Calibration : NO
Number of Runs (A & B) : 1
Multiplication Factor : 1.000
Uncalibrated Peaks RF : 0.00000

References

[Di67] W.A. Dietz, "Response Factors for Gas Chromatographic Analyses

[HP89] Hewlett Packard, 1989 Analytical Supplies Catalog and Chromatography Reference Guide.

Appendix F : Pressure Transducer Calibration

This appendix details the calibration of the pressure transducer used for tracing pressure rise in the combustion chamber. The pressure transducer is a Norwood model 111, four-active-arm strain gauge with a response frequency of 45 kHz.

With the amplification factor set at 1000, the pressure transducer was calibrated on a dead weight tester prior to each series of runs. A typical set of calibration data is tabulated in Table F.1. This calibration is also plotted in Figure F.1. Note that the maximum pressure used is only 368 kPa. This is because the range of pressures which corresponds to the initial flame growth from ignition until the flame front touches the walls falls inside this region.

Table F.1 : Pressure Transducer Calibration.

Pressure (Psig)	Voltage Output (V)	Absolute Pressure (kPa)
10	0.662	161.6
15	0.856	196.1
20	1.068	230.6
25	1.283	265.0
30	1.502	299.5
35	1.725	334.0
40	1.952	368.4

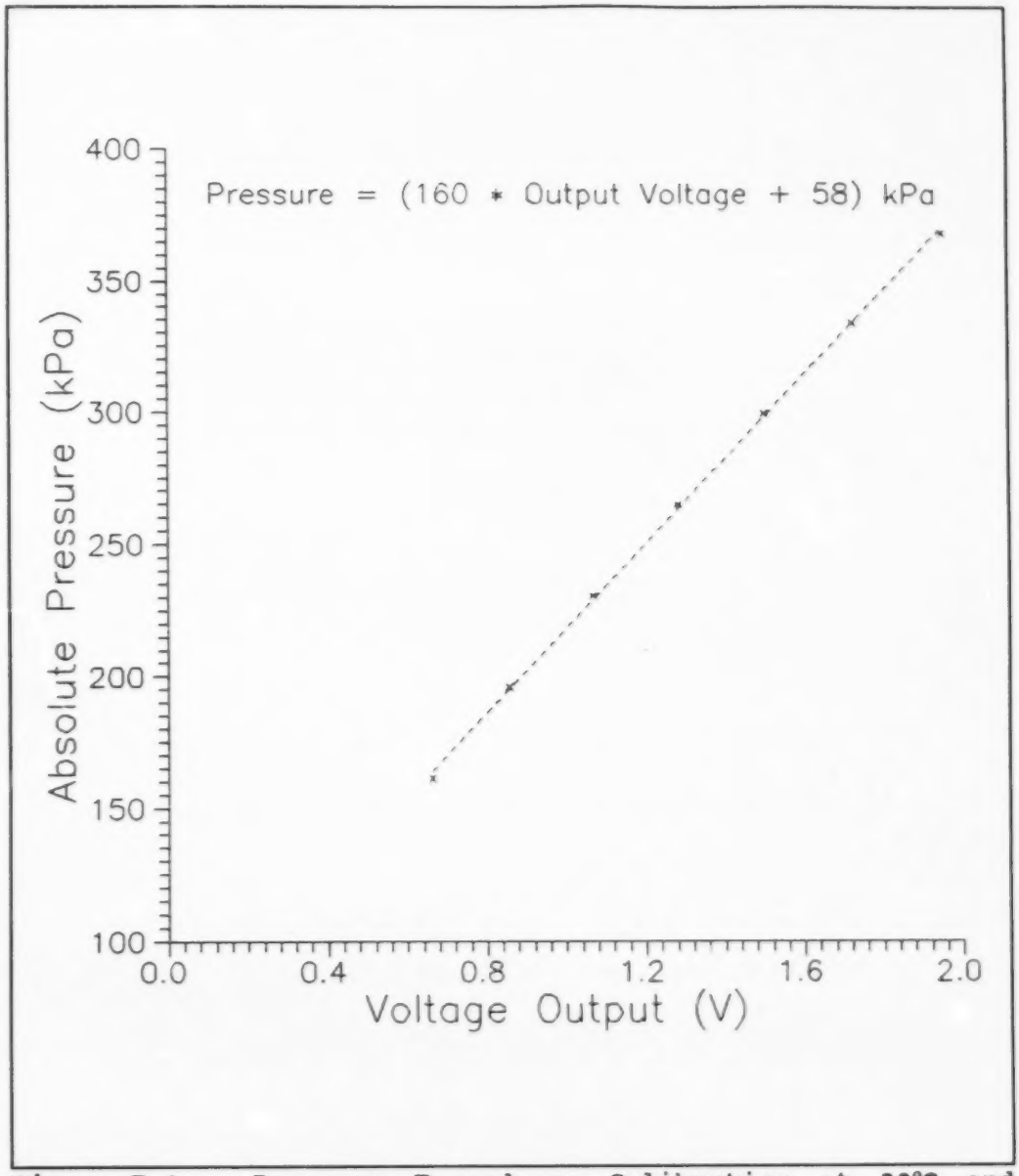

Figure F.1 : Pressure Transducer Calibration at 23°C and 92.7 kPa.

Appendix G : Digitization And Analysis Programs

This section details the actual software programs used for digitization and analysis. It details the path from the RACAL STORE 4DS FM tape recorder to the actual results of burning velocity.

Throughout this study, the path from the original recorded data to the burning velocity results is as shown in Figure G.1. The FM tape recorded all data at 30 in/s (inch per second) using the RACAL wide-band option giving a low-pass filter cutoff frequency of 40 kHz.

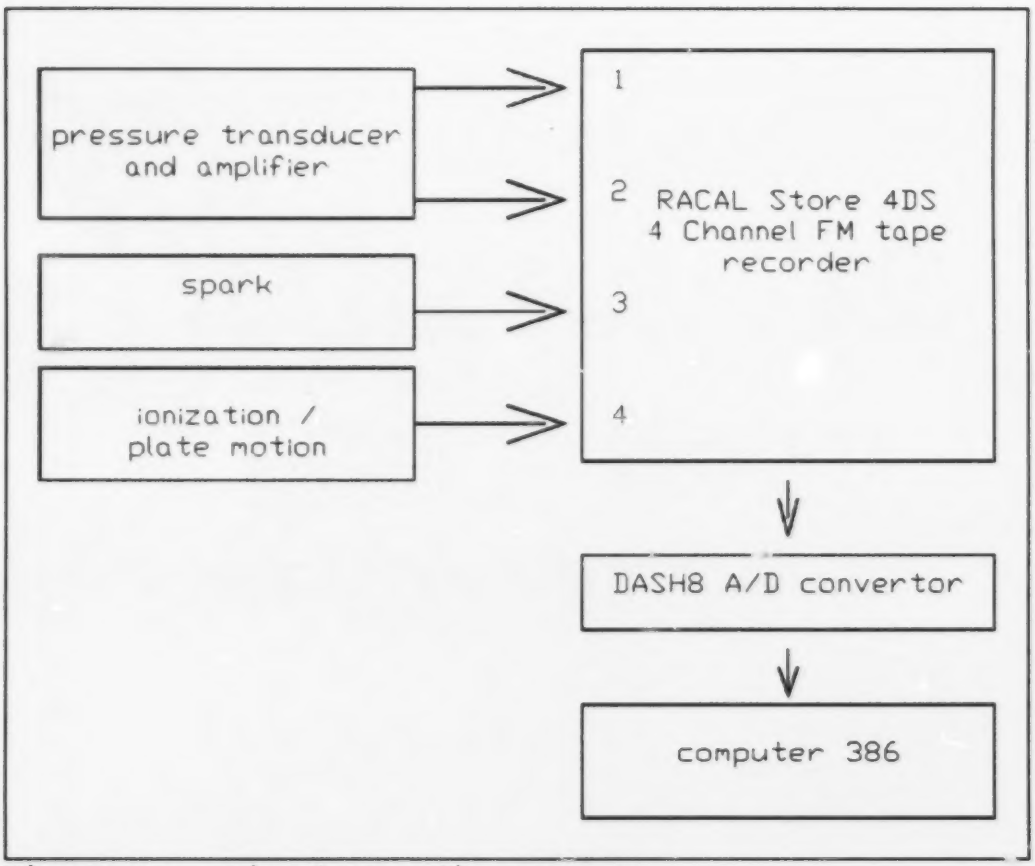

Figure G.1 : Signal Recording Summary.

A Metrabyte DASH8 A/D converter board was used for digitization. During digitization the replay was set at a speed of 1.875 in/s (16 times slower than that of the recording), while the digitization program, 4CHD8.bas, was taking data at a rate of 4000 Hz (3000 Hz was used for the slower burning quiescent run). Therefore, the effective digitization rate was 16 kHz (12 kHz for slower burning quescent runs) on each channel.

All four channels and time were recorded. The actual plate speed and spark delay, time for the plate to move from the centre of the spark gap to spark ignition, were calculated. The plate motion was measured using optical sensors to record the passage of a stirrup which was attached to the perforated plate. A phototransistor focused on alternating black and white markers at 10 mm intervals on the stirrup was used. The actual plate speed was taken as the average plate speed neglecting the very first 5 mm and the very last 5 mm where acceleration and deceleration occurred.

After digitization, a program called 4CPLT.bas was used to read and plot the digitized data file and convert the original voltage input into pressure in kPa. The maximum pressure and the corresponding time were recorded from channel 3 (channel 2 on the FM tape recorder). This program then saves the pressure trace of channel 2 (channel 1 on FM tape recorder) from spark ignition to the required end point, which is the end of the recorded data from the digitization program (4CHD8.bas) by default.

Theoretical results obtained from NEWBOMB.bas (used in conjunction with CMBCMB.bas and CMBSUB.bas) were then used to

interpolate the experimental result. Program NEWBP2.Bas was used to interpolate the experimental pressure trace with the theoretical value to get the other parameters involved.

The actual turbulence intensity at any instant was calculated using program RPDIST.bas. This program considers rapid distortion effects in conjunction to the normal decay.

The final stage was the burning velocity calculation which uses the program SUT.bas. This program uses a geometric method to calculate the burning velocity. The geometric method as used in SUT.bas calculates the progation of the combustion wave with repect to the actual flame front by taking the compression and expansion of the burning element into account. The actual flame front was taken as the geometric average radius of the previous and the burning flame radii, while the propagating wave was this flame front plus the unburnt element volume.

The video images were digitized using programs developed at the University of Alberta (Mechanical Engineering Department) after image capture with the Data Translation DT2782 Flame Grabber. The images go through the following programs sequentially.

- PASS
- AUSAVEI
- FLASH with flame area option

The program FLASH calculates the area occupied by the outer Schlieren edge of the flame front. From this calculated area, the relative radius and hence the flame growth rate are obtained. Program FGBP2.bas was used to interpolate the calculated flame

growth rate with the theoretical results from NEWBOMB.bas to obtain the other parameters involed. A program called SUI.bas was then used to calculate the burning velocity.